Contract No. 777564

INNOVATIVE RUNNING GEAR SOLUTIONS FOR NEW DEPENDABLE, SUSTAINABLE, INTELLIGENT AND COMFORTABLE RAIL VEHICLES

D 4.2 – Complete virtual test method for structure-borne and airborne noise transmission

Due date of deliverable: 28/02/2019

Actual submission date: 13/03/2019

Leader/Responsible of this Deliverable: David Thompson, ISVR University of Southampton

Reviewed: Y

Document status		
Revision	Date	Description
0	21/02/2019	First issue for approval by TMT
1	08/03/2019	Taking account of TMT comments
2	13/03/2019	Final version after review and Quality check

This project has received funding from Shift2Rail Joint Undertaking under the European Union's Horizon 2020 research and innovation programme under grant agreement No 777564.

Dissemination Level		
PU	Public	X
CO	Confidential, restricted under conditions set out in Model Grant Agreement	
CI	Classified, information as referred to in Commission Decision 2001/844/EC	

Start date of project: 01/09/2017 Duration: 24 months

REPORT CONTRIBUTORS

Name	Company	Details of Contribution
David Thompson	ISVR	Overall responsible; Executive Summary; Sections 1, 4, 5
Xiaowan Liu	ISVR	Sections 4.1, 4.3, 4.4
Hui Li	ISVR	Sections 4.3, 4.4
Gang Xie	CDH	Sections 3.3, 4.2
Pascal Bouvet	Vibratec	Sections 2.1, 3.1, 3.2, 3.4, 3.5, Appendix A.1, A.3, A.4, A.7, A.8
Martin Rissmann	Vibratec	Sections 2.1, 3.1, 3.2, 3.4, 3.5, Appendix A.1, A.3, A.4, A.7, A.8
Luis Baeza	ISVR / UPV	Section 2.2
Francisco Denia	UPV	Section 2.2, Appendix A.5, A.6
Juan Giner	UPV	Appendix A.2, A.3
Javier Carballeira	UPV	Appendix A.2
José Martínez	UPV	Appendix A.3
Maria Laura Trifiletti	RINA-C BE	Quality check

EXECUTIVE SUMMARY

This deliverable describes the virtual test method for noise transmission from the running gear to the train interior. It includes the various sub-models and the way they are assembled. Methods for determining wheelset vibration, structure-borne noise transmission and airborne noise transmission are described, including example results for the chosen case study. Field measurements on a static train have been carried out at Metro de Madrid and used for tuning the model.

The wheelset transmits vibration from the wheel/rail contact point to the axlebox. To investigate the influence of wheel rotation on this transmission, a new model of a rotating wheelset is introduced. Results are presented in the form of transfer receptances and displacement transmissibilities. Although the results of introducing the rotation are mostly small, it is shown that the rotation leads to a coupling between the vertical and longitudinal directions.

To determine the structure-borne transmission through the bogie, a finite element model of the bogie frame is established and verified against static measurements. The dynamic stiffnesses of the primary suspension and bushings of the traction bar and secondary damper are based on laboratory measurements from Deliverable D4.1. The model is excited by the wheel/rail forces, taking account of the fact that excitation by vertical and lateral forces at a given wheel are coherent, whereas contributions from different wheels are incoherent. The model is used to determine the blocked forces at the connection points to the car body. These are combined with measured vibro-acoustic transfer functions to determine the interior noise.

For the airborne sound transmission the sound power from the rolling noise is calculated using the TWINS model. Parameters for the track and wheel are obtained or verified using the static measurements. Sound power from the bogie frame is also calculated using a boundary element model based on the finite element calculations carried out for the structure-borne transmission. The transmission of sound below the vehicle is calculated using a statistical energy analysis method and compared with static measurements. Similarly the transmission of sound to the exterior panels of the train is calculated using a 2.5D boundary element method and verified using static measurements. The results will then be combined with the acoustic transmission loss of exterior panels to determine the interior sound.

The various models have been assembled and demonstrated. The following specific conclusions have been reached:

- It has been verified by comparison between the modal summation approach and the direct calculation that the modal summation approach can be used with the frequency-dependent stiffness elements.

- The two models for acoustic propagation beneath and around the vehicle have been successfully verified using static measurements with a loudspeaker source.

Running measurements have also been obtained on the same vehicle at Metro de Madrid and will be used subsequently for validation of the modelling approach.

ABBREVIATIONS AND ACRONYMS

ATV	Acoustic Transfer Vectors
BEM	Boundary Element Method
CAT	Corrugation Analysis Trolley
DPRS	Discrete Point Reacting Spring model
EMA	Experimental Modal Analysis
FEM	Finite Element Method
FRF	Frequency Response Function
SEA	Statistical Energy Analysis
TDR	Track Decay Rate
TPA	Transfer Path Analysis
TSI	Technical Specifications for Interoperability
TWINS	Track-Wheel Interaction Noise Software

TABLE OF CONTENTS

LIST OF FIGURES

LIST OF TABLES

1. INTRODUCTION

Workpackage 4 of RUN2Rail aims to develop tools and methodologies for predicting the transmission of noise and vibration from the running gear into the carbody and new technologies for reducing noise and vibration transmission in order to improve passenger comfort. The work described in this report is focused on developing simulation models for predicting running gear noise that can be used as 'virtual test methods'. The objectives are to:

- Predict the structure-borne noise transmission by determining the wheelset vibration and developing simulation models for the vibration of the bogie frame.
- Determine the airborne noise transmission by predicting the noise radiated by the wheels, track and bogie frame.
- Combine these two sub-models together in a single modelling approach capable of representing the noise of various different bogie designs.
- Illustrate the application of the method for an example case study.

The work focuses on a trailer vehicle of a Metro de Madrid train. As it is a trailer vehicle, only rolling noise sources are considered. The methods developed will also be applicable to impact noise from wheel flats, rail joints and switches & crossings and the methods for airborne noise transmission will also be applicable to squeal noise. However, these sources are not considered in this work. A series of static and running measurements have been performed on a test train for tuning of the models and ultimately for their validation. The static measurements are described in Appendix A this report.

In parallel with the work described here, laboratory tests have been carried out by KTH and ISVR on various suspension elements (primary suspension spring, traction bar, lateral damper and associated bushings). Based on these measurements, models for the vibration transmission through these elements have been proposed. Results are reported in Deliverable D4.1 [1] and will be used as input to the current model.

In Section 2 the wheelset vibration is studied. Two different approaches are compared. In the first case a TWINS-like approach will be adopted and the contact forces calculated by means of roughness excitation. A finite element (FE) model of a non-rotating wheelset will be used to calculate the response to this excitation. In an alternative approach, an advanced model of the wheelset that includes the inertial effects associated with the spinning rotation is adopted.

Section 3 presents a model for structure-borne noise transmission through the bogie. The bogie frame is modelled using Finite Elements and is coupled with models of primary and secondary suspension elements from D4.1. This model is compared with results from the static tests. Using

the axlebox vibration as the input, the forces acting on the carbody can be predicted. These can be combined with (measured) vibroacoustic transfer functions to the interior of the vehicle.

In Section 4 the airborne noise transmission is considered. Noise radiated from the vibrating wheels, rail and sleepers is predicted using TWINS [2]. In addition the noise radiated by the bogie is predicted using the same finite element model used for the structure-borne path. A model of the under-floor cavity has been developed to obtain sound pressure levels at the train floor and a separate model is developed for the noise propagation to the sides of the train. The sound transmitted to the interior will be determined using measurement data for the sound transmission loss of the vehicle floor and walls.

Finally the different sub-models will be integrated to form a versatile approach to modelling noise and vibration transmission through and from the bogie.

The measurement campaign carried out at Metro de Madrid in March and July 2018 for both static and running conditions will be reported more fully in Deliverable D4.3 – Validation of complete virtual test method for structure-borne and airborne noise transmission. This deliverable will report the results of the validation tests and comparisons between the complete virtual test method and the field measurements.

2. WHEELSET VIBRATION

The objective of this task is to calculate wheelset vibration levels at the axle box. Two different approaches are compared. In the first case, a TWINS-like approach is adopted and the contact forces are calculated by means of roughness excitation. A finite element (FE) model of a non-rotating wheelset is used to calculate the response to this excitation. In an alternative approach, an advanced model of the wheelset that includes the inertial effects associated with the spinning rotation is adopted.

2.1 TWINS-LIKE APPROACH

The vibration transfer, in terms of acceleration γ, from one wheel-rail interaction to one axle box of the bogie can be expressed as follows [3], [4]:

$$\vec{\gamma}_{axle\ box} = \begin{pmatrix} \gamma_z \\ \gamma_y \end{pmatrix} = [B]\ \vec{F}_{contact} \tag{2.1}$$

The contact force $\vec{F}_{contact}$ is obtained as described in Section 3.4.1 including the corresponding wheel/rail roughness spectra and contact patch filtering effect. Note that when calculating the axle

box vibration, equation (2.1) takes into account the correlation effect between the vertical component F_z and the lateral component F_y of one wheel-rail contact excitation.

The total axle box vibration is the sum of two different wheel-rail contact excitations, due to the coupling via the axle. In that case, as the wheel/rail roughness of the two opposite contact patches are uncorrelated, an uncorrelated sum of the contributions of the two excitations has to be done (sum of the squared values). This point is detailed in Section 3.4.2.

$[B]$ is the axle box accelerance matrix γ/F obtained from the FE model of Section 3.3:

$$[B] = \begin{bmatrix} B_z & \cdots & B_{zy12} \\ \vdots & \ddots & \vdots \\ B_{yz12} & \cdots & B_y \end{bmatrix} \tag{2.2}$$

The cross terms represent coupling between vertical (z) and lateral (y) directions as well as between the wheels of the wheelset.

2.2 ROTATING WHEELSET MODEL

2.2.1 Introduction

The wheelset model that will be adopted in this task can be found in Ref. [1]. This model adopts realistic hypotheses such as the inertial effects due to the rotation and the wheelset flexibility. In spite of this complexity, the equation of motion by means of this model is linear and has a low computational cost. The difficulty associated with the generation of the model is similar to a finite element one, and consequently this methodology can be easily transferred to the industry.

The dynamics of the railway wheelset is studied in this section by means of frequency response functions (FRF) such as the receptance and the transmissibility: the receptance permits to obtain the response at certain coordinate due to a harmonic excitation, whereas the transmissibility function is the ratio between the harmonic responses associated with two coordinates. Both FRFs are adopted in this methodology for accounting the contribution of the wheelset dynamics in the carbody vibration.

2.2.2 Background

From Reference [5], the equation of motion of the rotating wheelset is

$$\tilde{\mathbf{M}}\ddot{\mathbf{q}} + \Omega\tilde{\mathbf{C}}\dot{\mathbf{q}} + \left(\tilde{\mathbf{K}}_1 + \Omega^2\tilde{\mathbf{K}}_2\right)\mathbf{q} = \mathbf{f}\,, \tag{2.3}$$

where Ω is the angular velocity of the wheelset, $\mathbf{q}$ is a vector that contains Eulerian modal coordinates, $\tilde{\mathbf{M}}$ and $\tilde{\mathbf{K}}_1$ are respectively the modal mass and stiffness matrices, $\tilde{\mathbf{C}}$ and $\tilde{\mathbf{K}}_2$ are constant matrices that takes into account the gyroscopic and stiffening effects, and $\mathbf{f}$ is the generalised force vector.

The terms in the equation of motion are calculated from a finite element mesh, which is shown in Figure 1. The figure also shows the coordinates that are important for this study, which are associated with points that link the wheelset with the track and the axleboxes. The coordinates that are presented in Figure 1 are listed below.

- c_1 vertical displacement at the left wheel/rail contact point (positive downward).
- c_2 lateral displacement at the left wheel/rail contact point (positive leftward).
- c_3 longitudinal displacement at the left wheel/rail contact point (positive forward).
- c_4 vertical displacement at the right wheel/rail contact point (positive downward).
- c_5 lateral displacement at the right wheel/rail contact point (positive leftward).
- c_6 longitudinal displacement at the right wheel/rail contact point (positive forward).
- a_1 vertical displacement at the left axlebox centre (positive downward).
- a_2 lateral displacement at the left axlebox centre (positive leftward).
- a_3 longitudinal displacement at the left axlebox centre (positive forward).
- a_4 vertical displacement at the right axlebox centre (positive downward).
- a_5 lateral displacement at the right axlebox centre (positive leftward).
- a_6 longitudinal displacement at the right axlebox centre (positive forward).

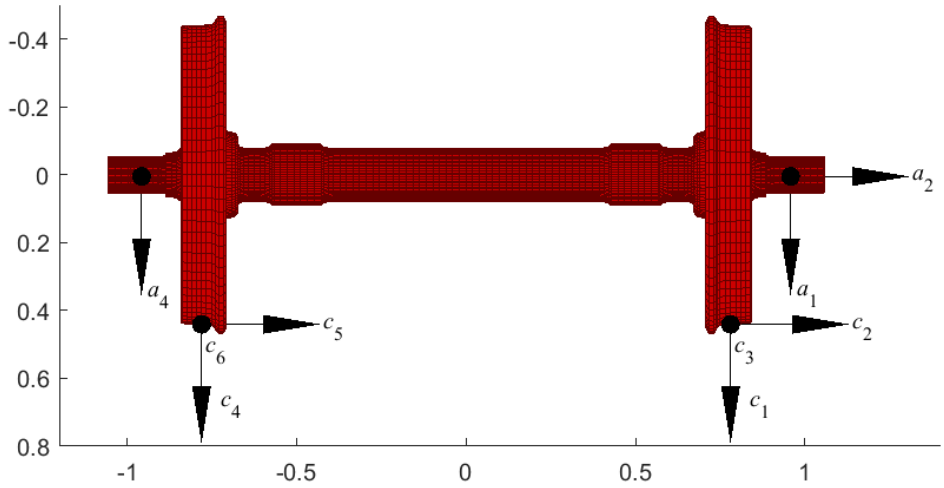

Figure 1: Wheelset mesh and coordinates of the axlebox and contact point displacements

The displacements at the contact points and the axleboxes are computed from the modal coordinate vector as follows

$$\mathbf{x} = \mathbf{\Phi}\,\mathbf{q}\,, \tag{2.4}$$

where $\mathbf{\Phi}$ is the modal matrix, and $\mathbf{x} = \begin{bmatrix}\mathbf{c}^{\mathrm{T}} & \mathbf{a}^{\mathrm{T}}\end{bmatrix}^{\mathrm{T}}$ are the displacements at the contact and the axlebox locations. The generalised force vector is calculated from the external forces $\mathbf{F}$ by means of the following formula

$$\mathbf{f} = \mathbf{\Phi}^{\mathrm{T}}\,\mathbf{F}\,. \tag{2.5}$$

By assuming that the external forces are harmonic with frequency ω, the modal response is

$$\mathbf{q} = \tilde{\mathbf{H}}(\omega)\mathbf{f}\,, \tag{2.6}$$

where

$$\tilde{\mathbf{H}}(\omega) = \left[-\omega^2\,\tilde{\mathbf{M}} + \mathrm{i}\,\omega\Omega\tilde{\mathbf{C}}\,\dot{\mathbf{q}} + \left(\tilde{\mathbf{K}}_1 + \Omega^2\,\tilde{\mathbf{K}}_2\right)\right]^{-1}. \tag{2.7}$$

From equations (2.4) to (2.7) the receptance FRF associated with physical coordinates is obtained from the following expression

$$\mathbf{H} = \mathbf{\Phi}\tilde{\mathbf{H}}\mathbf{\Phi}^{\mathrm{T}}\,. \tag{2.8}$$

The matrix $\mathbf{H}$ allows the response due to a harmonic excitation to be calculated using

$$\mathbf{x} = \mathbf{H}\,\mathbf{F}\,. \tag{2.9}$$

The transmissibility function that relates the responses at the j-th and ℓ-th coordinates when a harmonic excitation is applied at the ℓ-th coordinate, can be computed as follows

$$T_{j\ell}(\omega) = \frac{x_j}{x_\ell} = \frac{H_{j\ell}}{H_{\ell\ell}}\,. \tag{2.10}$$

Typically, the ℓ-th coordinate is at the wheel/rail contact whereas the j-th one is associated with the axlebox centre displacements.

Generating a plot with 1000 points by means of Eq. (2.10) needs (approx.) 3 s in a personal computer.

2.2.3 Receptances

The results that are presented in this Section have been calculated for the non-motored wheelset of a Metro de Madrid vehicle (see Figure 1). The wheel diameter is 860 mm. The mode shapes of the wheelset can be found in Figure 2.

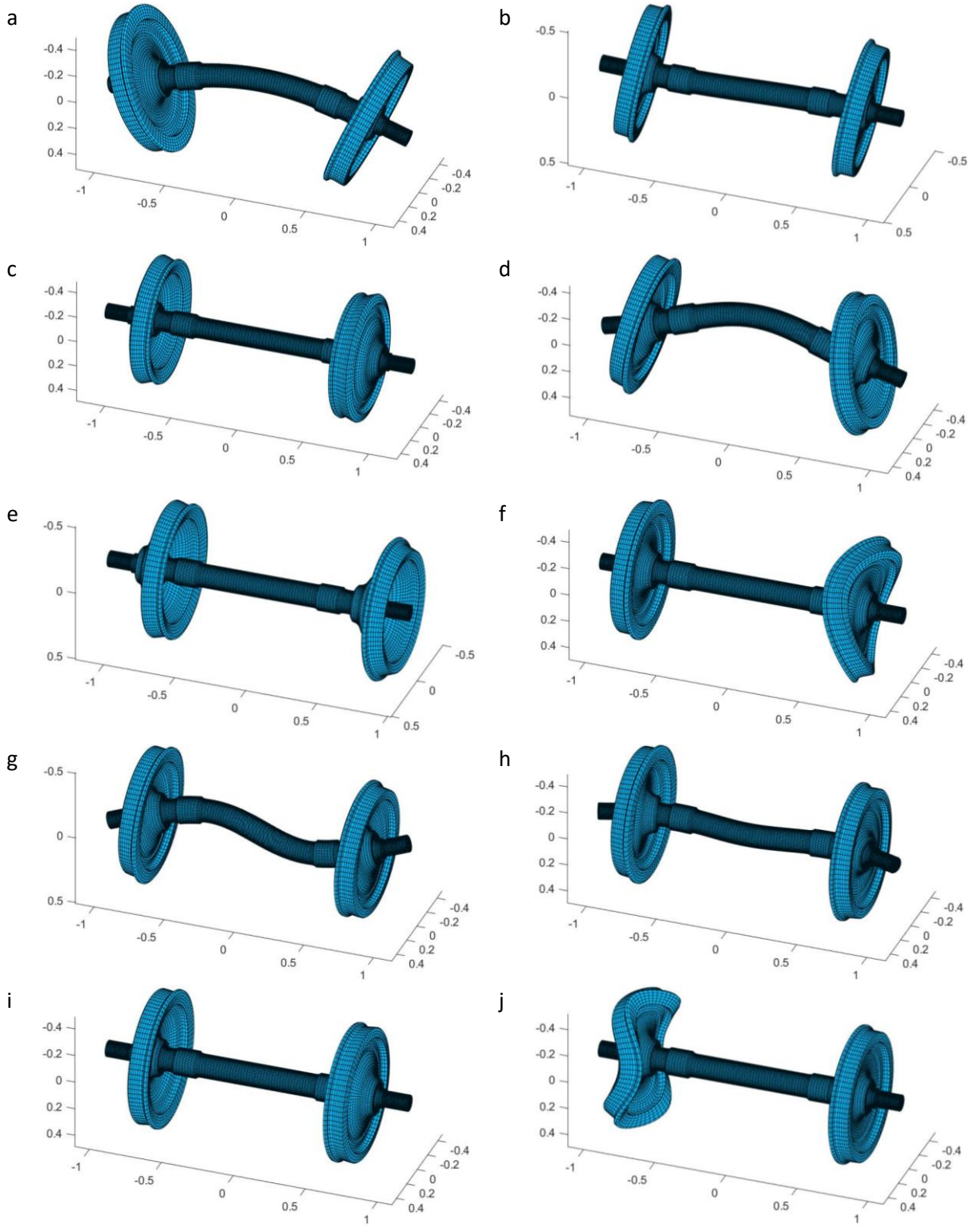
a
b
c
d
e
f
g
h
i
j

Figure 2: First 10 mode shapes of the free-boundary wheelset. Natural frequencies at a) 79.59 Hz, b) 133.7 Hz, c) 238.5 Hz, d) 259.1 Hz, e) 367.2 Hz, f) 397.3 Hz, g) 561.7 Hz, h) 927.6 Hz, i) 1013.7 Hz, j) 1072.9 Hz.

Figure 3 presents the transfer receptance $H_{a_1c_1}(\omega)$ that relates the vertical response at the left axlebox centre (according to Figure 1, the coordinate a_1) and the vertical excitation at the left wheel tread (coordinate c_1). The calculation has been carried out for three angular velocities of the wheelset that correspond to 0, 50 and 100 km/h. This result shows almost the same results for all the vehicle speeds except for the first bending mode at 79.59 Hz (see Figure 2 (a)). At this frequency, the receptance peak splits with the angular velocity. This effect can be seen for the other modes with multiplicity 2 or more, but it is less remarkable (due to the logarithmic frequency scale).

The gyroscopic effects become more important when analysing the transfer receptance that relates the vertical excitation in the wheel/rail contact point with the longitudinal response in the axlebox centre $H_{a_3c_1}(\omega)$. This is plotted in Figure 4. Due to the axisymmetry of the wheelset, this receptance is zero when the angular velocity of the wheelset is zero. However the receptance $H_{a_3c_1}(\omega)$ is comparable to $H_{a_1c_1}(\omega)$ when the angular velocity increases. This effect enables the transmission of vibration through the primary suspension, which frequently is much stiffer in the longitudinal direction than the vertical direction.

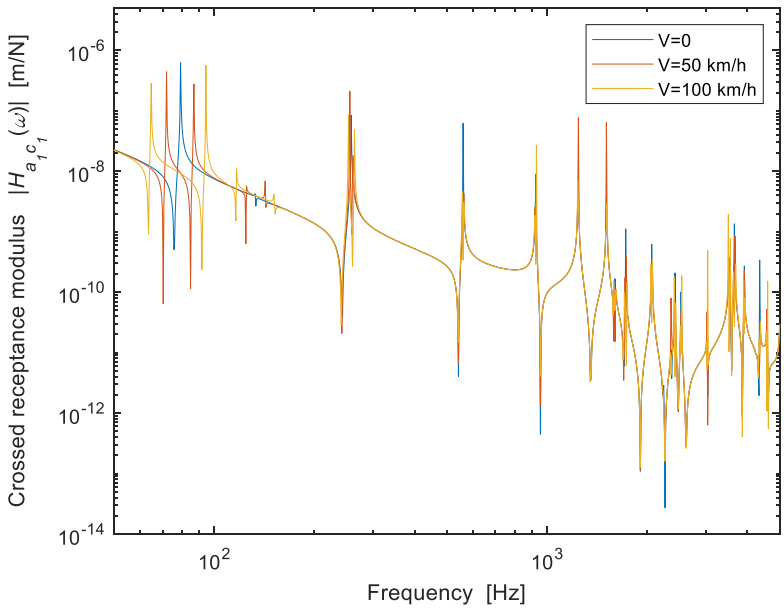

Figure 3: Transfer receptance $H_{a_1c_1}(\omega)$ giving the vertical response at the axlebox centre due to a vertical harmonic excitation at the wheel contact point. This FRF has been obtained for three angular velocities of the wheelset that correspond to 0, 50 and 100 km/h.

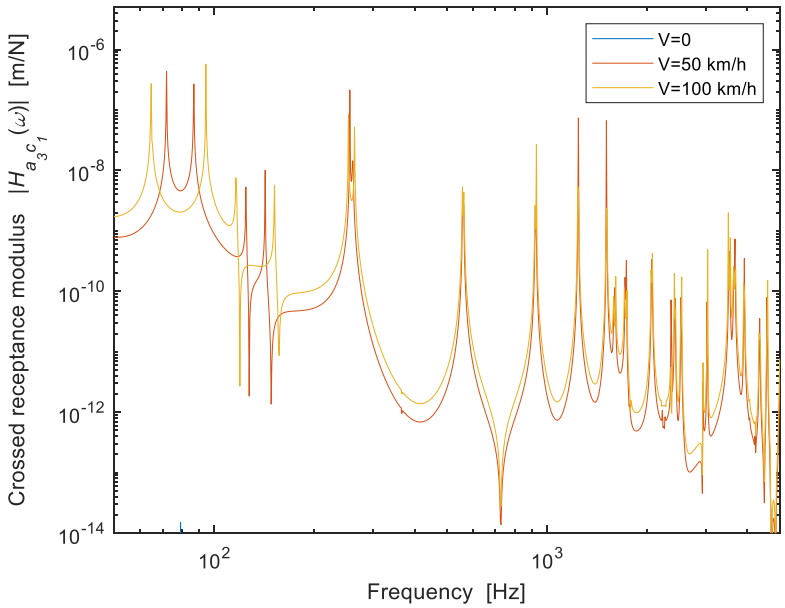

Figure 4: Transfer receptance $H_{a_3c_1}(\omega)$ giving the longitudinal response at the axlebox centre due to a vertical harmonic excitation at the wheel contact point. This FRF has been obtained for three angular velocities of the wheelset that correspond to 50 and 100 km/h. The receptance is zero when the velocity is zero.

2.2.4 Transmissibility

Figure 5 shows the transmissibility function that $T_{a_1c_1}(\omega)$ that relates the vertical displacements at the left axlebox centre and the left wheel tread. From this result, apart from a few peaks and dips associated with resonances and antiresonances, the transmissibility is close to 1 for frequencies lower than 500 Hz. This shows that, apart from the resonances, the wheelset behaves as a rigid body at medium and low frequency. The present wheelset has a band between 555 and 921 Hz where there is a significant amplification at the axleboxes, whereas there is certain filtering effect at higher frequencies (away from the resonances). Again, the influence of the wheelset rotation is more remarkable below 300 Hz.

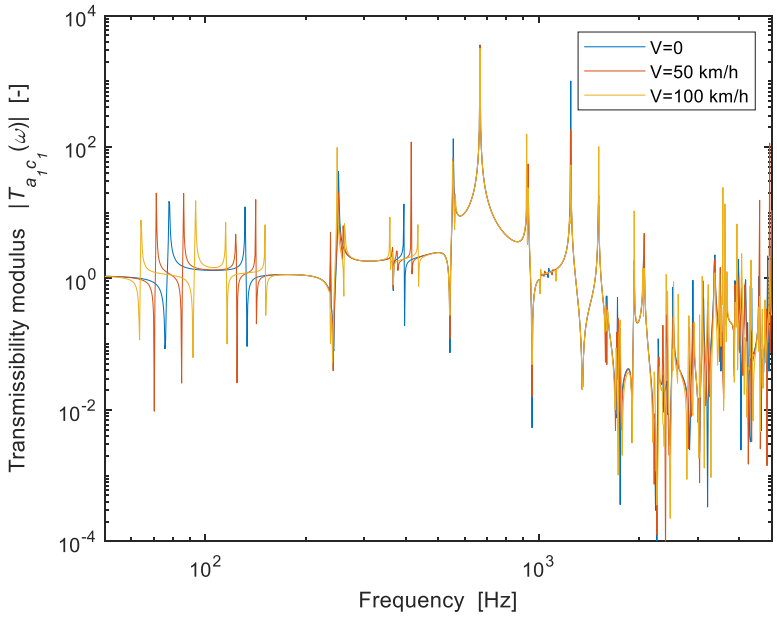

Figure 5: Transmissibility function that relates the vertical displacements at the wheel/rail contact (input) and the axlebox centre (output). This FRF has been obtained for three angular velocities of the wheelset that correspond with 0, 50 and 100 km/h.

Figure 6 plots the transmissibility associated with the longitudinal axlebox displacement (output) and the vertical wheel displacement at the contact point (input). Due to the wheelset axisymmetry, this function is zero when the angular velocity of the wheelset is zero. Nevertheless, the calculations show non-zero transmissibility when the wheelset rotates. When comparing the transmissibility in Figure 5 and Figure 6, the latter is much smaller except at the resonances, where the contribution of the wheelset rotation becomes important. It can be inferred that the longitudinal forces that can be transmitted through the longitudinal stiffness are tonal.

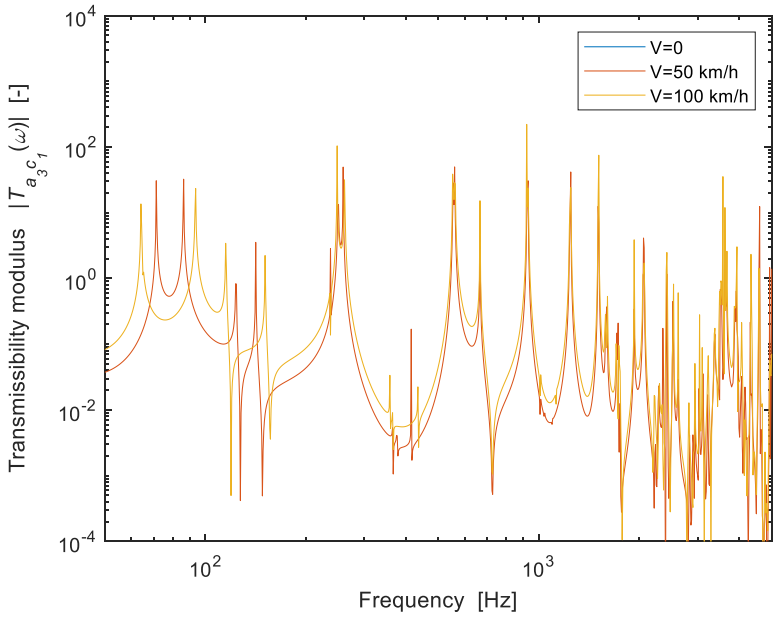

Figure 6: Transmissibility function that relates the vertical displacement at the wheel/rail contact (input) and the longitudinal displacement at the axlebox centre (output). This FRF has been obtained for three angular velocities of the wheelset that correspond with 50 and 100 km/h. The transmissibility is null when the velocity is zero.

3. STRUCTURE-BORNE NOISE TRANSMISSION MODEL

The structure-borne path starts at the wheel/rail contact and propagates through the suspensions and bogie frame into the car body. For the chosen case study, the bogie frame has been modelled using Finite Elements and will be coupled with models of primary and secondary suspension elements from D4.1 [1]. Using the axlebox vibration from the previous section as the input, the forces acting on the car body are predicted.

3.1 STRUCTURE BORNE NOISE SYNTHESIS USING BLOCKED FORCE APPROACH

In the scope of RUN2Rail, no vibro-acoustic model of the car body is available. For this reason a complete computational model – from wheel-rail contact point to interior pressure level – cannot be implemented. Note that such global models are nowadays more and more common in the automotive industry (i.e. from tyre-road excitation to noise inside car body, see ref. [6]).

To overcome this difficulty, the structure borne noise inside the vehicle can be estimated thanks to the so-called Transfer Path Analysis (TPA) method:

$$P_j = \sum_{i=1}^{M} H_{ij} F_i \qquad \text{or in matrix form: } \{p\} = [H_{disconnected}]\{F\} \tag{3.1}$$

where H_{ij} is the vibro-acoustic transfer function between the pressure P_j at points j inside the vehicle and the input forces F_i at carbody input points *i*. This interior noise synthesis can be done in two different ways:

- Using the **"internal force method"**:

In this case, the internal forces $\{F_{\text{int}}\}$ at the connecting points are combined with the vehicle vibroacoustic transfer functions $[H_{disconnected}]$ measured with vibration sources (in the present case, traction bars and lateral dampers) disconnected from the car body (in this case the bolster beam which is rigidly fixed to the car body). The structure borne noise is then assessed as follows:

$$\{p\} = [H_{disconnected}]\{F_{int}\} \tag{3.2}$$

- Using the **"blocked force method":**

In this case, the blocked forces $\{F_{bl}\}$ at the connecting points are combined with the vehicle vibroacoustic transfer functions ($[H_{connected}]$) measured without disconnecting the vibration source from the car body. The structure borne noise is then assessed as follows:

$$\{p\} = [H_{connected}]\{F_{bl}\} \tag{3.3}$$

These two noise synthesis techniques can be used with computed data, measured data or in a combined approach: for example some automotive manufacturers use dedicated test benches to measure blocked forces and combine these measured blocked forces with computed vibro-acoustic transfers of the complete vehicle (see ref. [7], pages 30-35).

In the scope of RUN2Rail, the TPA method using the blocked force approach has been selected:

- In the global model described in Section 3.3, the car body is replaced by simple clamped boundary conditions. The outputs of the computational model are the blocked forces at the car body input points (in our case the fixing points of the traction bar and of the lateral dampers to the car body). The next section describes how these blocked forces are obtained from the finite element model.

- In a second step, these **computed blocked forces** are then combined with **measured vibro-acoustic transfers P/F** of the car body, obtained on the test vehicle without disconnecting the vibration sources (traction bars and lateral dampers) from the car body.

These vibro-acoustic transfer functions were measured during a measurement campaign on a vehicle of Metro de Madrid rolling stock.

The next sections describe how these blocked forces, and also wheelset and bogie vibration levels, are obtained from the finite element model, taking into account that the entire system is excited by four wheel/rail contact patches.

3.2 GENERAL APPROACH

The vibration response on the wheelset, bogie frame and connecting elements can be estimated using the following equation which relates the dynamic forces $\vec{F}_{contact}$ of the wheel-rail interaction to the vibration level γ:

$$\gamma = [H_{\gamma/F}]\,\vec{F}_{contact} \tag{3.4}$$

$[H_{\gamma/F}]$ is the vibration transfer matrix of the entire bogie and $\vec{F}_{contact}$the interaction force of a given wheel-rail contact patch. In the same way, blocked forces at the car body input points are estimated from a force transmissibility matrix $[H_{F/F}]$ and contact forces:

$$\vec{F}_{bl} = [H_{F/F}]\,\vec{F}_{contact} \tag{3.5}$$

Special care is required to correctly build this matrix, since vertical and lateral contributions of one single wheel are correlated and contributions from one wheel to another are uncorrelated. Details of this aspect are given in Section 3.4.

Both the matrices $[H_{\gamma/F}]$ and $[H_{F/F}]$ are obtained from the complete bogie finite element model including the wheelsets and the suspension elements.

3.3 DESCRIPTION OF THE FE MODEL

In this project, a trailing bogie of a Metro Madrid vehicle is modelled using the FE package Nastran. The full FE model includes the bogie frame, a front wheelset, a rear wheelset, axle boxes, primary suspension springs, lateral dampers and traction bars as shown in Figure 7. The wheelsets, bogie frame and axle boxes are modelled using solid elements. The dampers and traction bars could also be modelled using solid elements or appropriate one-dimensional beam elements; the latter approach is used here. The primary suspension springs and rubber bushings are modelled using spring-damper elements with the measured frequency-dependent properties from Deliverable D4.1 [1]. The FE bogie model consists of over 1.36 million nodes.

Wheel/rail forces calculated from Section 2.1 using the TWINS approach will be applied in the FE model. To evaluate the structure-borne noise transmission into the interior, the forces acting on the carbody are required. In the present study, the carbody is not considered and instead the blocked-force method is used. Therefore the four connecting points on the bolster, to which the traction bars and lateral dampers are attached, are constrained as fixed. The forces acting on these four nodes will be calculated. The structure-borne noise can then be predicted by using these forces together with noise transfer functions from forces at these positions to the interior sound pressure. These could be obtained either through simulations or measurements. In the present project they have been measured.

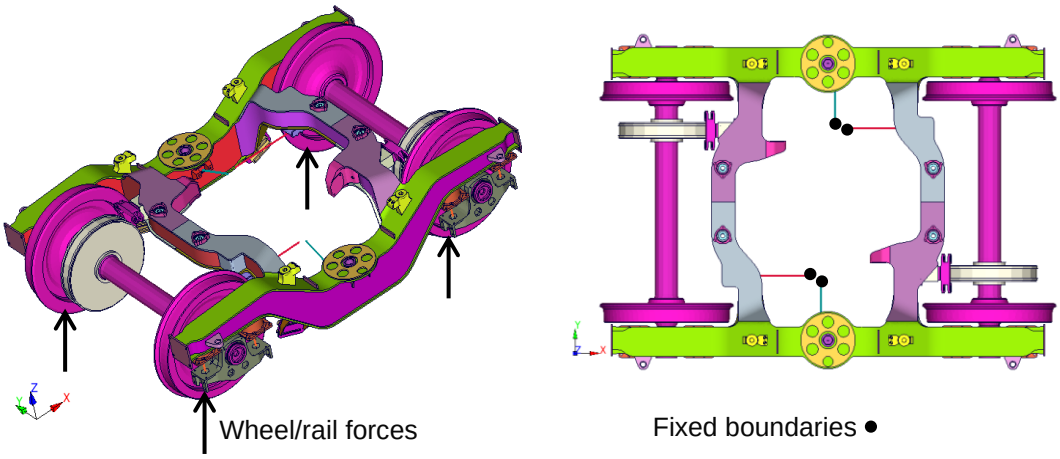

Figure 7: The FE model for the bogie with dampers and traction bars modelled by 1D bar elements.

3.3.1 Frequency dependent stiffness

The frequency response calculation is usually carried out using modal summation approach to reduce the computational cost. The displacement in physical coordinates $u(\omega)$ is given by

$$\{u(\omega)\} = [\Phi]\{q(\omega)\} \tag{3.6}$$

where $[\Phi]$ is the matrix mode shapes and $q(\omega)$ is the modal coordinates.

The equation of motion in terms of the modal coordinates for a damped system is

$$(-\omega^2[\Phi]^T[M][\Phi] + i\omega[\Phi]^T[B][\Phi] + [\Phi]^T[K][\Phi])\{q(\omega)\} = [\Phi]^T F(\omega) \tag{3.7}$$

$$(-\omega^2[m] + i\omega[b] + [k])\{q(\omega)\} = f(\omega) \tag{3.8}$$

where [*M*],[*B*] and [*K*] are mass, damping and stiffness matrices of the FE model, and [*m*],[*b*] and [*k*] are their modal counterparts. When a spring or damper becomes frequency dependent, the stiffness and damping matrices are changed and the mode shapes [*Φ*] are also changed. For a large model the computational cost of obtaining the mode shapes is expensive. The advantage of using the modal summation approach is to avoid solving the eigenvalue problems again. Therefore, a modal correction to the modal damping and stiffness matrices is introduced based on the original mode shapes [*Φ*]. Eq.(3.8) becomes

$$(-\omega^2[m] + i\omega[b + \Delta b] + [k + \Delta k])\{q(\omega)\} = f(\omega) \tag{3.9}$$

where *Δk* and *Δb* are modal correction terms which are due to Δ*K* and Δ*B*, the changes of stiffness and damping in physical coordinates, given by

$$\Delta b = [\phi]^T[\Delta \mathrm{B}][\phi] \tag{3.10}$$

$$\Delta \mathrm{k} = [\phi]^T[\Delta K][\phi] \tag{3.11}$$

As frequency-dependent complex stiffness terms are present for the primary suspension springs and rubber bushings in the FE model, Eqs (3.6) to (3.11) are used to calculate the responses in Nastran. This approach has been widely used in the automotive industry. Figure 8 shows a comparison between the modal summation approach and the direct calculation including the frequency-dependent primary suspension stiffness. The response in Figure 8 was taken from an arbitrarily selected node in the model. The direct solution was carried out with a low frequency resolution while the modal summation approach has a much higher frequency resolution. The graphs on the right show a close-up of a limited frequency range.

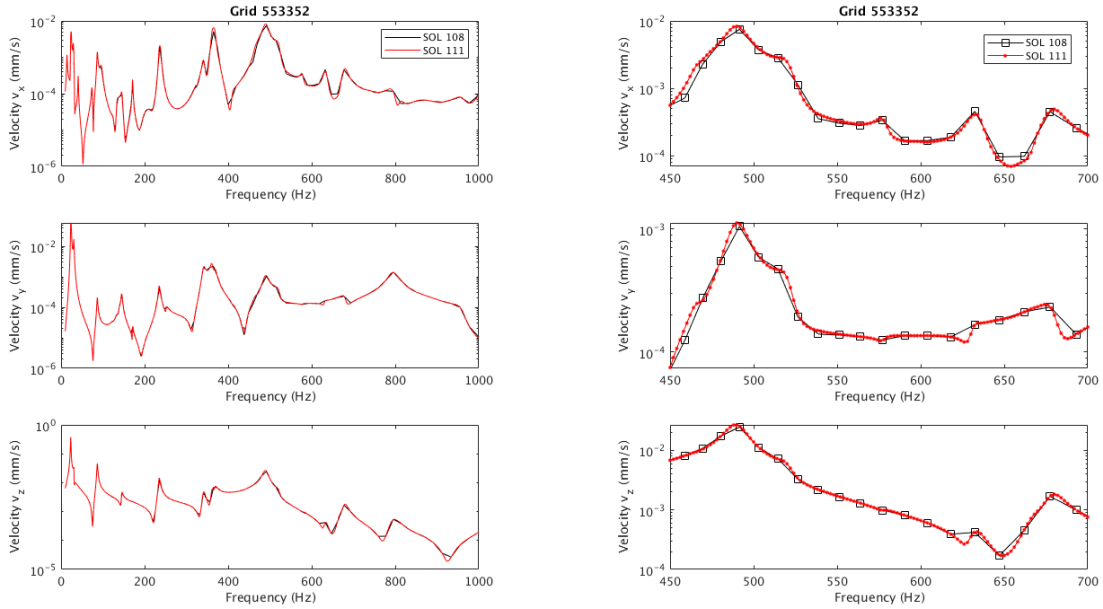

Figure 8: Comparison of responses calculated with the direct method (SOL 108) and the modal summation approach (SOL 111) for frequency dependent primary stiffness.

3.3.2 Method to include components with frequency dependent stiffness

The dynamic properties of the primary suspension spring, lateral damper and traction bar have been investigated in [1]. In the Nastran FE model, it is proposed to model these dynamic properties using the CBUSH element, a general spring and damper element with the capability of including frequency dependent stiffness and damping. The CBUSH element is defined between two points in the model. The stiffness of a CBUSH includes translation and rotation directions. In practice, it is common to define two coincident points to model a suspension component, with a dynamic stiffness only given for the three translation degrees of freedom. The rotational stiffness is set to a high value to constrain the rotation.

Consider only a spring connecting points 1 and 2 for a single direction. The stiffness matrix of a CBUSH element for this spring is given by

$$K = \begin{bmatrix} k_{11} & -k_{12} \\ -k_{21} & k_{22} \end{bmatrix} \tag{3.12}$$

where $k_{11} = k_{12} = k_{21} = k_{22} = k$ and k is the stiffness defined in the CBUSH element. The force in the CBUSH element is determined by its stiffness and relative deformation of the spring.

However, the dynamic stiffness of the primary suspension spring cannot be sufficiently modelled by a single CBUSH element using Eq. (3.7). Due to the internal mass effect, the diagonal stiffness terms are different from the off-diagonal term. The diagonal stiffness can be called a point stiffness and the off-diagonal stiffness a transfer stiffness. For primary spring, Eq. (3.12) is thus re-written as

$$K = \begin{bmatrix} k_{po} & -k_{tr} \\ -k_{tr} & k_{po} \end{bmatrix} \tag{3.13}$$

The two point stiffnesses may also be different from one another depending on the mass distribution, but the two transfer stiffnesses are equal by reciprocity. To include Eq. (3.13) in the FE model, three CBUSH elements are needed. The first CBUSH element is same as that described by Eq. (3.12). It is defined between points 1 and 2 with its stiffness set to be the transfer stiffness. Two additional grounded CBUSH elements are meanwhile introduced at points 1 and 2 respectively. A grounded spring is a point spring. The force at a grounded spring is determined by its stiffness and the displacement of the point. If the grounded spring has its stiffness defined by the difference between the point stiffness and transfer stiffness, the assembled stiffness matrix for the three CBUSH elements becomes

$$K = \begin{bmatrix} k_{tr} & -k_{tr} \\ -k_{tr} & k_{tr} \end{bmatrix} + \begin{bmatrix} k_{po} - k_{tr} & 0 \\ 0 & 0 \end{bmatrix} + \begin{bmatrix} 0 & 0 \\ 0 & k_{po} - k_{tr} \end{bmatrix} \tag{3.14}$$

It can be seen that Eq. (3.14) is the same as Eq. (3.13). Therefore the dynamic stiffness of the primary suspension springs can be readily modelled in the FE model using three CBUSH elements. As the top and bottom of the primary suspension spring have different mass and stiffness, the point stiffnesses added at the top and bottom sides should be different. This effect can also be handled with the grounded CBUSH elements at top and bottom.

3.4 CONTACT FORCES

3.4.1 Contact force calculation

The contact force $\vec{F}_{contact}$ resulting from the wheel-rail interaction is calculated using a TWINS-like approach [2] as follows. For this, the roughness excitation $\vec{R}$, and the receptance matrix $[A]$ of the wheel, rail and contact at the interaction contact point are required. The contact force $\vec{F}_{contact}$ is then calculated according to

$$\vec{F}_{contact} = \begin{pmatrix} F_z \\ F_y \end{pmatrix} = ([A]_w + [A]_r + [A]_c)^{-1}\vec{R} \tag{3.15}$$

The roughness excitation $\vec{R}$ is actually an imposed displacement in the vertical direction, such that $\vec{R} = (R_z, 0)$. Furthermore, the input roughness is filtered by the contact patch. This filtering effect depends on speed and wheel load. A Remington contact filter will be used here [8].

The receptance matrices $[A]$ of the wheel, rail and contact are calculated by different means. For the wheel $[A]_w$ is defined as

$$[A]_w = \begin{bmatrix} A_z & \cdots & A_{zy12} \\ \vdots & \ddots & \vdots \\ A_{yz12} & \cdots & A_y \end{bmatrix}_w \tag{3.16}$$

Cross terms represent coupling between vertical (z) and lateral (y) receptances as well as between wheel 1 and 2 of one wheelset. $[A]_w$ is calculated with the FE model of Section 3.3.

The rail receptance matrix $[A]_r$ is given as

$$[A]_r = \begin{bmatrix} A_z & \cdots & A_{zy12} \\ \vdots & \ddots & \vdots \\ A_{yz12} & \cdots & A_y \end{bmatrix}_r \tag{3.17}$$

Again, it could contain coupling terms between vertical and lateral directions as well as between two rails. In the present case, $[A]_r$ is calculated with TWINS and thus contains just A_z, A_y, A_{zy} and A_{yz} (i.e. the coupling between the two rails is neglected). Alternatively a Finite Element model of the track could be used to include this coupling.

The contact receptance matrix $[A]_c$ is given as

$$[A]_c = \begin{bmatrix} A_z & \cdots & 0 \\ \vdots & \ddots & \vdots \\ 0 & \cdots & A_y \end{bmatrix}_c \tag{3.18}$$

It may also contain cross terms representing spin and creepage phenomena. $[A]_c$ is calculated with TWINS.

3.4.2 Correlation effects between contact forces

The forces transmitted to the car body result from the wheel-rail interaction of the four wheels of the bogie. For each wheel vertical F_z and lateral F_y contact forces come into play (longitudinal forces F_x are negligible). In order to determine for example the acceleration at a certain point of the system, e.g. at the axle box, one has to distinguish between correlated and uncorrelated contributions in the transfer matrix $[H]$.

$$\vec{\gamma} = \begin{pmatrix} \gamma_z \\ \gamma_y \end{pmatrix} = [H]\vec{F}_{contact} = [H]\begin{pmatrix} F_z \\ F_y \end{pmatrix} \tag{3.19}$$

For a single wheel the lateral and vertical force are correlated:

$$\gamma_z = \left(\frac{\gamma}{F}\right)_z F_z + \left(\frac{\gamma}{F}\right)_{zy} F_y \tag{3.20}$$

However, the contribution from one wheel to another can be considered as uncorrelated, since combined wheel-rail roughness at different contact points are uncorrelated.

For four wheel, the vertical acceleration at the observation point becomes thus:

$$\gamma_{total,z} = \sqrt{\sum_1^4 {\gamma_{z,i}}^2} = \sqrt{\left[\left(\frac{\gamma_z}{F_z}\right)F_z + \left(\frac{\gamma_z}{F_y}\right)F_y\right]_1^2 + \cdots + \left[\left(\frac{\gamma_z}{F_z}\right)F_z + \left(\frac{\gamma_z}{F_y}\right)F_y\right]_4^2} \tag{3.21}$$

This equation can be adapted to calculate the car body blocked forces $\vec{F}_{car}$:

$$F_{car,z} = \sqrt{\sum_1^4 {F_{car,z,i}}^2} = \sqrt{\left[\left(\frac{F_{car,z}}{F_z}\right)F_z + \left(\frac{F_{car,z}}{F_y}\right)F_y\right]_1^2 + \cdots + \left[\left(\frac{F_{car,z}}{F_z}\right)F_z + \left(\frac{F_{car,z}}{F_y}\right)F_y\right]_4^2} \tag{3.22}$$

The interior sound pressure can thus be estimated by injecting results (3.22) into equation (3.3).

3.5 METHOD VALIDATION APPROACH

A large experimental data base acquired during a two weeks measurement campaign in March 2018 at Metro de Madrid is available for the method validation. The various static measurements forming part of this data base is described in the appendices of this document. The corresponding running measurements will be described in Deliverable D4.3.

A complete model validation would go beyond the scope of the project which aims at a modelling method for structure borne and airborne transmission.

Comparisons between measurement and simulation results will be carried out. The focus will be on qualitative agreement.

4. AIRBORNE NOISE TRANSMISSION MODEL

The airborne path starts from the wheel and track vibration and propagates through the air until reaches the external boundary of the car body. The model for the airborne propagation path is described in this section. Noise radiated from the vibrating wheels, rail and sleepers are predicted using TWINS [2]. In addition the noise radiated by the bogie is predicted using the bogie model from the previous section. The noise propagates through the air underneath the car body where it develops a partially diffuse field. An SEA model of the under-floor cavity has been developed to obtain sound pressure levels at the train floor. Through reflections and diffraction, noise also reaches the sides of the train and can enter the car body through the side walls. A 2.5D boundary element model is presented for this. The sound transmitted to the interior will be determined using measured data for the sound transmission loss of the vehicle floors and walls.

4.1 TWINS MODEL OF ROLLING NOISE

4.1.1 Introduction

This section describes the prediction of rolling noise caused by wheel and rail vibration using the TWINS model [2]. The input parameters required for the TWINS calculations are presented, including wheel and rail surface roughness, and the dynamic properties of track and wheel. Comparisons with the measurements described in the Appendix A.1 and A.2 for the wheel and track characterization are also given.

4.1.2 Background

An overview of the TWINS model for rolling noise is shown in Figure 9. Roughness on the wheel and rail surfaces induces wheel and rail vibrations which are responsible for radiating noise. The vertical relative displacement between the wheel and rail is determined by the combination of wheel and rail roughness, which are provided as one-third octave spectra and are assumed to be incoherent. Together with the known wheel, rail and contact mobilities, the wheel/rail interaction forces can be computed. The calculations are performed in the frequency domain; the interaction and vibration calculations are performed in narrow frequency steps and the noise radiation is calculated in one-third octave bands.

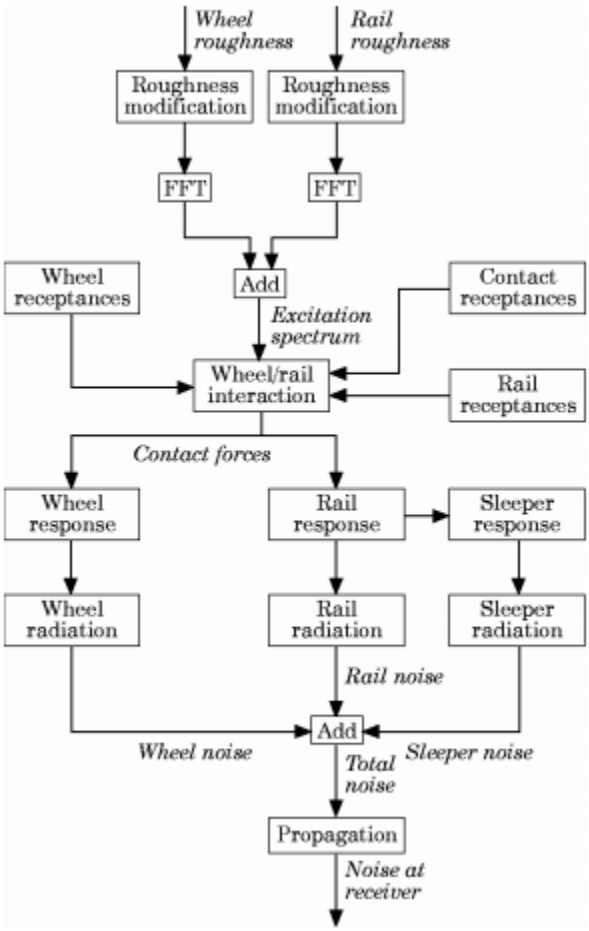

Figure 9: An overview of the TWINS model for rolling noise [2]

The frequency response of the wheel can be calculated from the modal basis of the wheel obtained from a finite element analysis. The track system consists of rail, pad, sleeper and ballast and is modelled by a Timoshenko beam model with two-layer support, as shown in Figure 10. Calculations are performed for both continuously and discretely supported track.

Once the vibration response of the wheel and track has been determined, the sound power is calculated by combining predicted vibration spectra with radiation efficiencies.

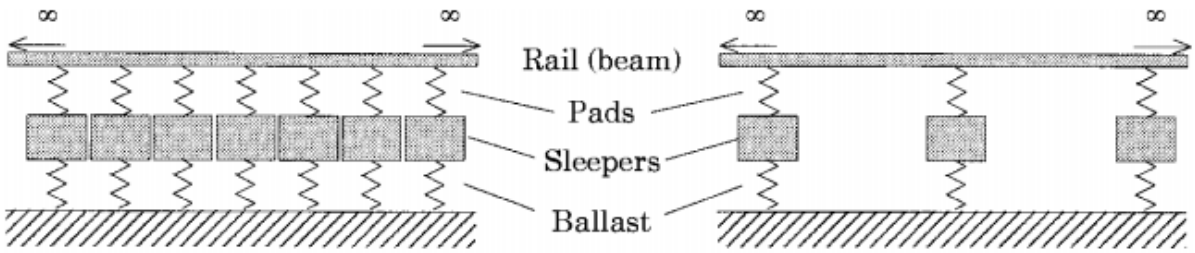

Figure 10: Models for track vibration: left, continuously supported; right, discretely supported [2].

4.1.3 Contact mobilities

As shown in Figure 11, the wheel/rail contact is represented in TWINS by a linearised Hertzian contact spring in the vertical direction and a combination of a contact spring and a creep force in the lateral direction. The magnitude and phase of the contact point mobilities predicted from TWINS are displayed in Figure 12. The corresponding input parameters are listed in Table 1.

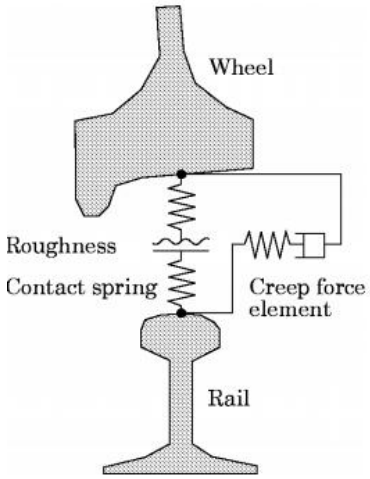

Figure 11: Schematic diagram of the wheel/rail system [2]

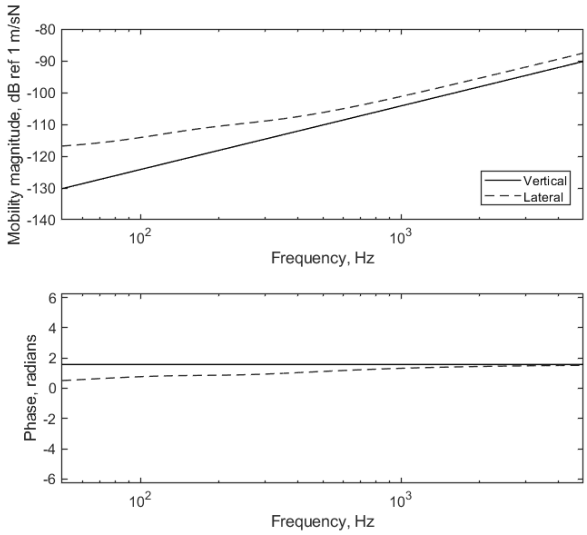

Figure 12: Contact point mobilities predicted from TWINS.

Table 1: Parameters defining the wheel/rail contact

Wheel radius	Rail head radius	Wheel transverse radius	Normal load	Vertical contact stiffness	Lateral contact stiffness	Contact patch dimension, a	Contact patch dimension, b
0.43 m	0.3 m	0 m	36230 N	1.02×10^9 N/m	7.54×10^8 N/m	5.0 mm	3.9 mm

4.1.4 Roughness

Figure 13 shows the one-third octave spectrum of the contact filter used in calculations. This is based on results from the DPRS (Discrete Point Reacting Springs) model which have been rescaled for the current contact patch length [10].

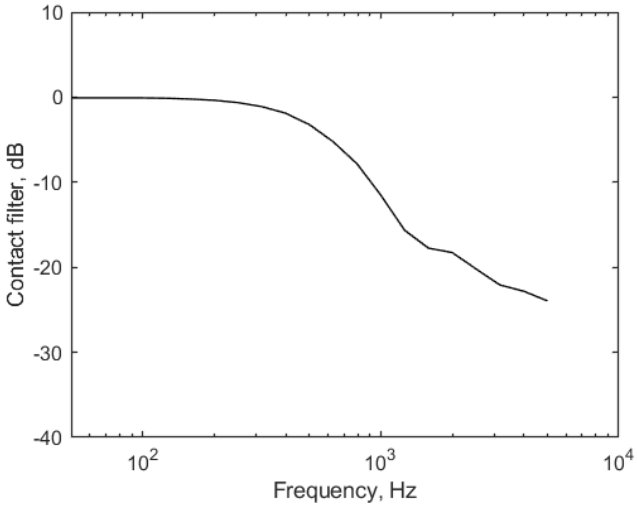

Figure 13: Contact filter from DPRS model; frequencies correspond to a speed of 50 km/h.

Figure 14 shows the one-third octave band spectra of wheel and rail roughness which are used as input to the TWINS model. These are the averaged levels of the measured data described in Appendix A.3. For the wheel, the average was taken over 4 trailer bogie wheels with 4 lines on each wheel; for the rail, it is averaged over the left and right rails with 5 lines on each. The limit spectrum from ISO 3095:2013 [11] (as used in the TSI-Noise) is also shown in Figure 14 for reference. The rail roughness seems high at long wavelengths, whereas the wheel roughness is generally much lower than the ISO limit.

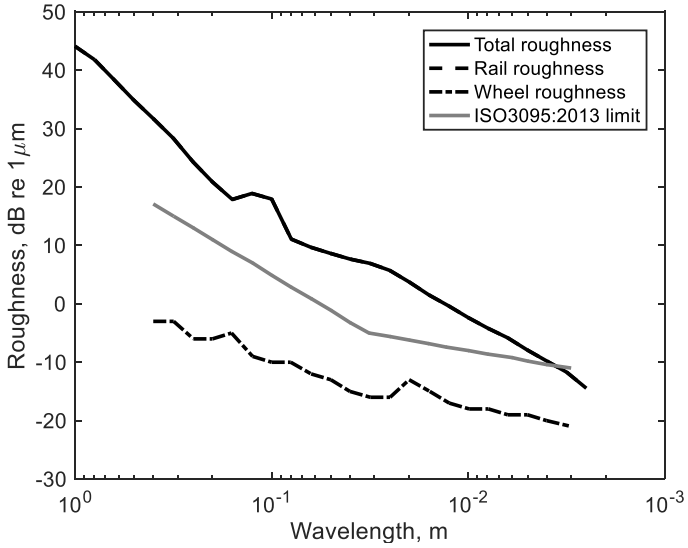

Figure 14: Wheel and rail roughness spectra

4.1.5 Track decay rate

To give an appropriate estimation of the rail pad stiffness, the track decay rates obtained with different rail pad stiffnesses are compared with the measured results in Figure 15. The limit curves from ISO 3095:2013 [11] are again shown for reference. These predicted results are based on the continuously supported rail model including a flexible sleeper. The input parameters are listed in Table 2. As the pad stiffness is reduced, a reduction is seen in the frequency at which a sharp drop in decay rate occurs. For the vertical direction, the prediction based on a pad stiffness of 800 MN/m gives the best fit to the measured data, while for the lateral direction, a value of 156 MN/m shows the best agreement.

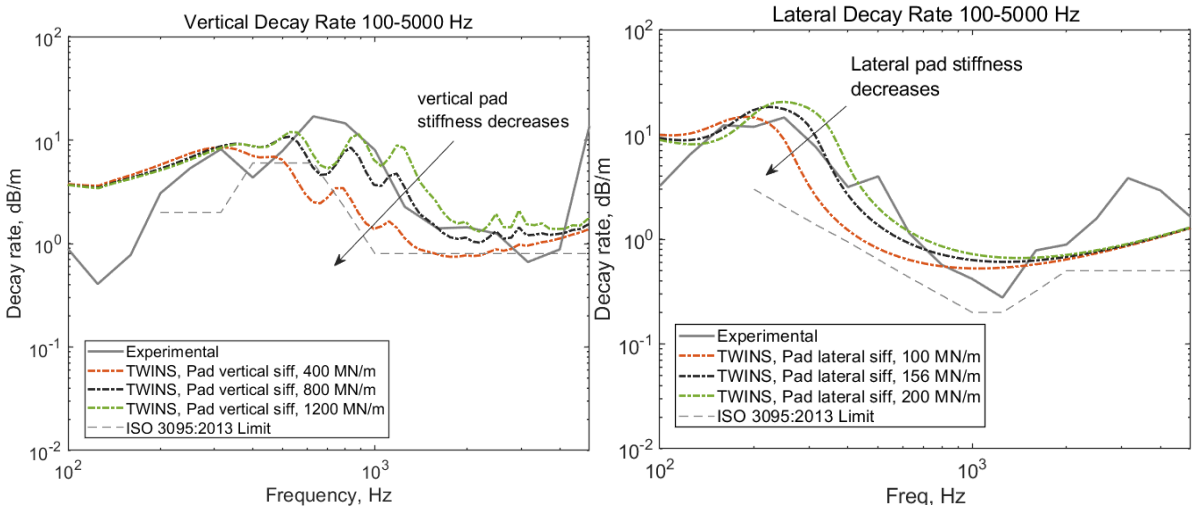

Figure 15: Effect of pad stiffness on track decay rates

Table 2: Parameters used in TWINS for the track

			Vertical	Lateral
Rail	Bending stiffness	EI	4.84×10^6 Nm^2	0.88×10^6 Nm^2
	Mass per unit length	ρA	54 kg/m	
	Damping loss factor	η_r	0.02	0.02
	Cross mobility factor	XdB	–12 dB	
Pad	Stiffness	K_p	8.00×10^8 N/m	1.56×10^8 N/m
	Damping loss factor	η_p	0.2	0.2
Bi-bloc	Mass (half sleeper)	m	150 kg	
	Spacing	d	1.0 m	
Mono-bloc	Young's Modulus	E	4.13×10^{10} N/m^2	
	Poisson's ratio	v	0.15	
	Damping loss factor	η_s	0.02	
	Mass	m	150 kg	
	Spacing	d	1.0 m	
	Length	L	2.4 m	
Ballast	Stiffness	K_b	4.0×10^7 N/m*	3.5×10^7 N/m
	Damping loss factor	η_b	1.0*	2.0

* frequency dependent

4.1.6 Rail mobility

The magnitude and phase of the rail point mobility, predicted with the continuously supported rail model, are shown in Figure 16.

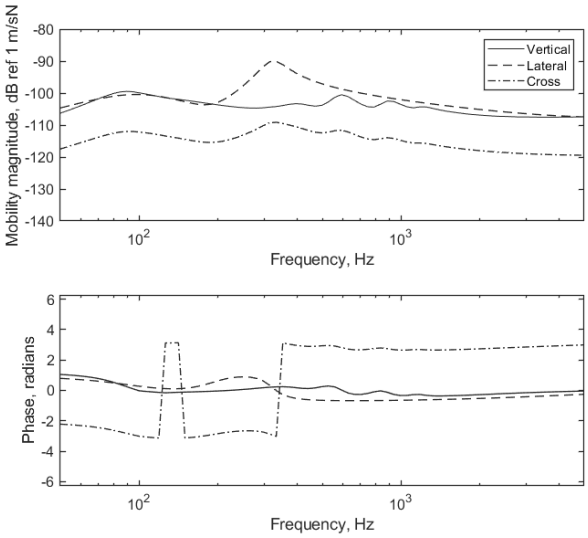

Figure 16: Rail point mobility predicted from TWINS with continuous support.

In the measurements in Appendix A.2 there are large differences between the vertical mobility measured above a sleeper and at mid-span. The pinned-pinned mode is found at 457 Hz, which is lower than the mode of the rail bouncing on the rail pad stiffness. Comparisons have therefore been made with a discretely supported track model. This model is currently only available with the sleepers represented as a mass, i.e. not including the flexible sleeper model. For comparison, results are obtained from the continuously supported track model with the mass model for the sleeper as well as with the flexible sleeper model considered above. Figure 17 and Figure 18 compare the results from the various models with the mobility measured at mid-span and above a sleeper, respectively.

In the models based on a mass model for the sleeper, a constant value of 40 MN/m is used for the ballast stiffness. This corresponds to the low frequency limit of the frequency dependent stiffness used in the continuously supported model. At frequencies above 70 Hz, the discretely and continuously supported models show significant differences. The models with continuous support fail to predict the first pinned-pinned frequency (peak at about 457 Hz) and the second one (dip at about 1490 Hz), which are observed in the measurement at mid-span, while these can be well predicted by the discretely supported model.

At the position above a sleeper, the measured point mobility appears to be contaminated at frequencies below 500 Hz. Good agreement between the discretely supported model and the measurement is obtained for the second pinned-pinned frequency at around 1490 Hz. This cannot be predicted by the models with continuous support.

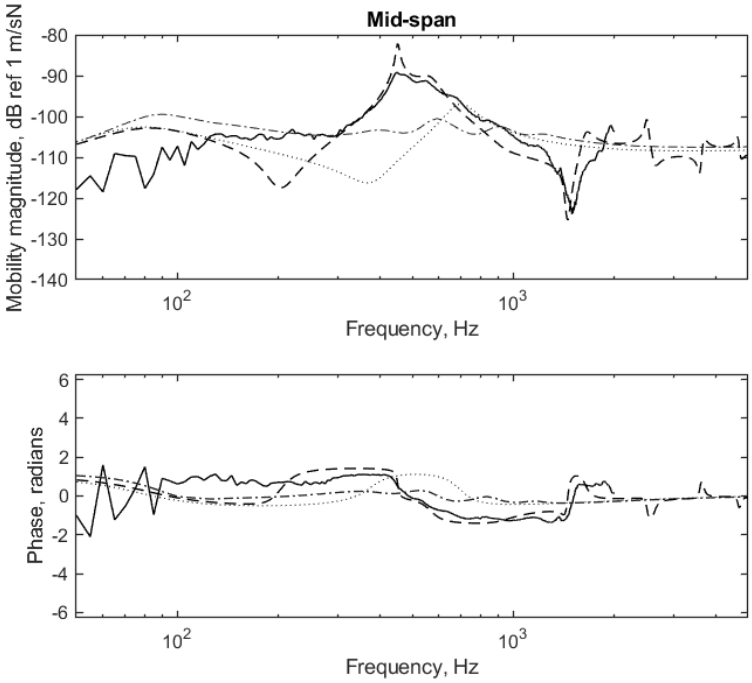

Figure 17: Vertical point mobility of track at mid-span. –, measurement; --, discretely supported model; -·, continuously supported model with flexible sleeper, ··, continuously supported model with mass sleeper model.

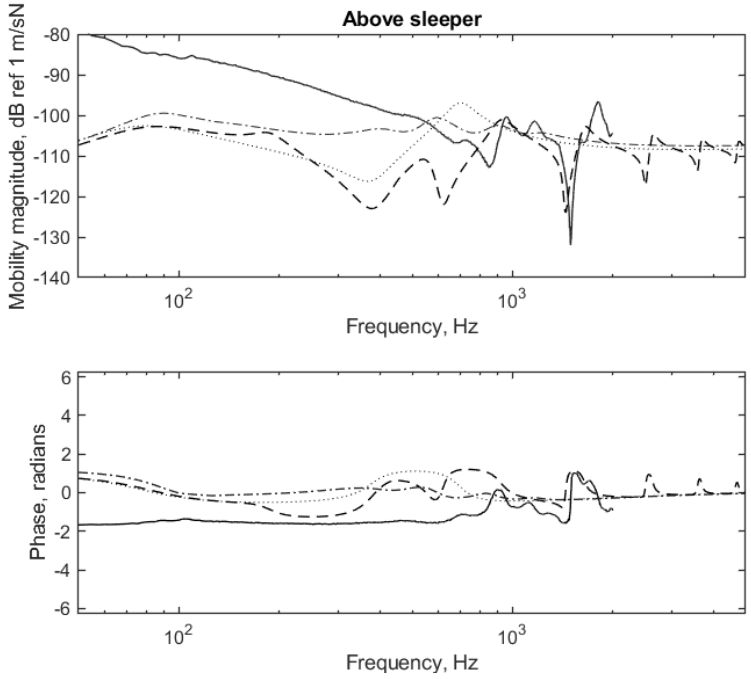

Figure 18: Vertical point mobility of track above sleeper. –, measurement; --, discretely supported model; -·, continuously supported model with flexible sleeper, ··, continuously supported model with mass sleeper model.

4.1.7 Wheel modes

The parameters used for the wheel are listed in Table 3. An axisymmetric finite element model of the wheel was created in the FE package ANSYS. The mesh configuration is shown in Figure 19. According to normal practice for a TWINS model, the axle was not included in the FE model but the inner edge of the hub was constrained in all directions. Free vibration analysis of the wheel was performed using ANSYS, from which the modal basis including the natural frequencies and selected mode shape information can be obtained. The natural frequencies of the most important modes are listed in Table 4, which also includes the results from the measurements from Appendix A.1 for comparison. To give a clear indication of the trend, the natural frequencies are also plotted in Figure 20. Good agreement is obtained between the current FE model and the measurements, although larger differences are found for modes (0,0) and (0,1) which will be more affected by the axle. It can be noted from Figure 2 that inclusion of the axle in the FE model yields two modes resembling each of these, one with the two wheels in phase and the other with them out of phase. For mode (0,0), mode c at 239 Hz corresponds to the result from ANSYS without the axle (256 Hz) whereas mode e at 367 Hz corresponds to the mode identified in the experiments at 351 Hz. Similarly for mode (1,0) mode b at 134 Hz corresponds to the result without the axle (168 Hz) whereas mode d at 259 Hz corresponds to the experimental mode at 270 Hz. The predicted natural frequencies of the two-nodal-circle axial modes and the circumferential modes, which were not identified in the experiments, are listed in Table 4. Based on the measured modal damping (see Table 6 in Appendix A.1), the minimum damping ratio in the model was set to 0.002. A damping ratio of 0.01 was used for modes with $n = 1$.

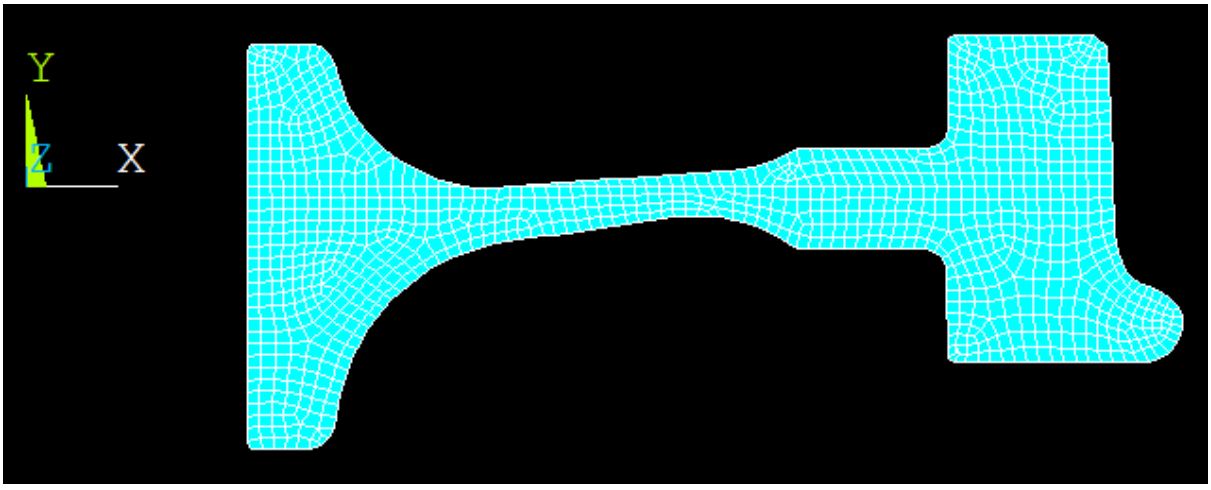

Figure 19: FE Mesh of the wheel

Table 3: Wheel parameters

Wheelset mass	Radius	Density	Elastic modulus	minimum damping ratio
1100 kg	0.43 m	7850 kg/m^3	210 GPa	0.002

Table 4: Natural frequencies in Hz of wheel for zero-nodal-circle, one-nodal-circle, and radial modes

	(*n*,0)		(*n*,1)		(*n*,R)		(*n*,2)	(*n*,C)
n	ANSYS	measured	ANSYS	measured	ANSYS	measured	ANSYS	ANSYS
0	256	351	1600		3120		4231	541
1	168	270	1830		1241		4292	3448
2	402	405	2322	2380	1816	1885	4482	4766
3	1086	1084	2914	2875	2478	2581	4870	6511
4	1955	1961	3604		3273	3166	5432	
5	2928	2939	4397	4378	4125	4548	6154	
6	3957	3975	5001	4984	5297	5401	7008	
7	5015	5042			5925	6324		
8	6086	6125						

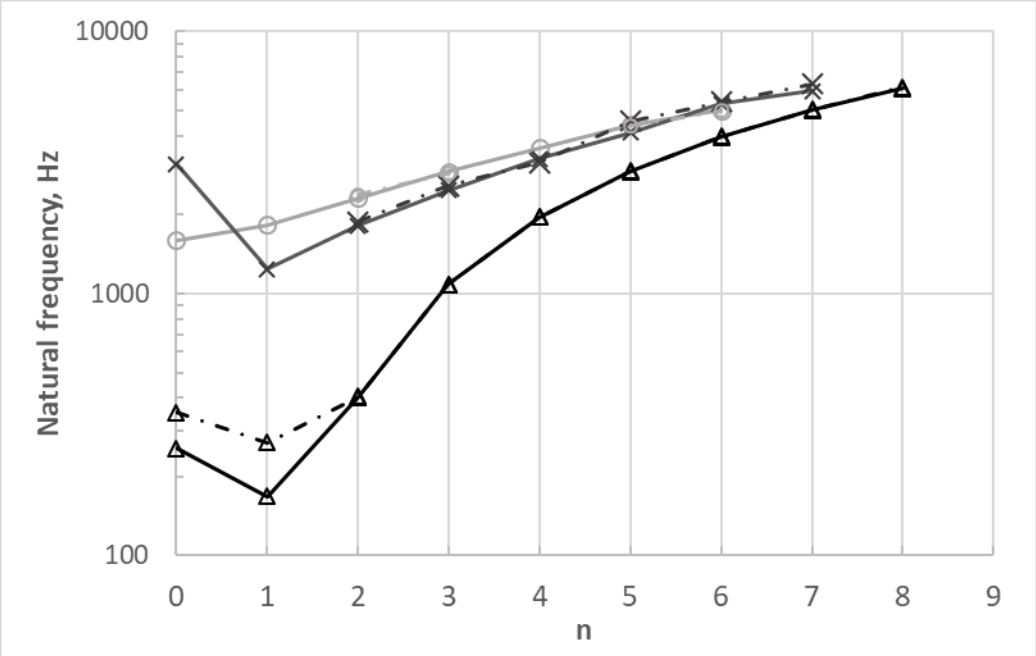

Figure 20: Natural frequencies of wheel. – Δ, zero-nodal-circle from ANSYS; – · Δ, zero-nodal-circle from measurements; – ○, one-nodal-circle from ANSYS; – · ○, one-nodal-circle from measurements; – ×, radial from ANSYS; – · ×, radial from measurements.

Figure 21 and Figure 22 display comparisons of the mobility of the wheel between the measurement and the predictions in the radial and axial directions respectively. In the radial mobility, an anti-resonance is found at around 750 Hz in the measurement, and around 500 Hz in the predictions. The resonance peaks, which are the radial and one-nodal circle axial modes, predicted by TWINS at high frequencies are close to those found from the measurement. For the axial mobility, which is dominated by the zero-nodal-circle axial modes, good agreement is obtained for the peaks at frequencies above 300 Hz. The behaviour at low frequencies is influenced by the axle which is not included in the model.

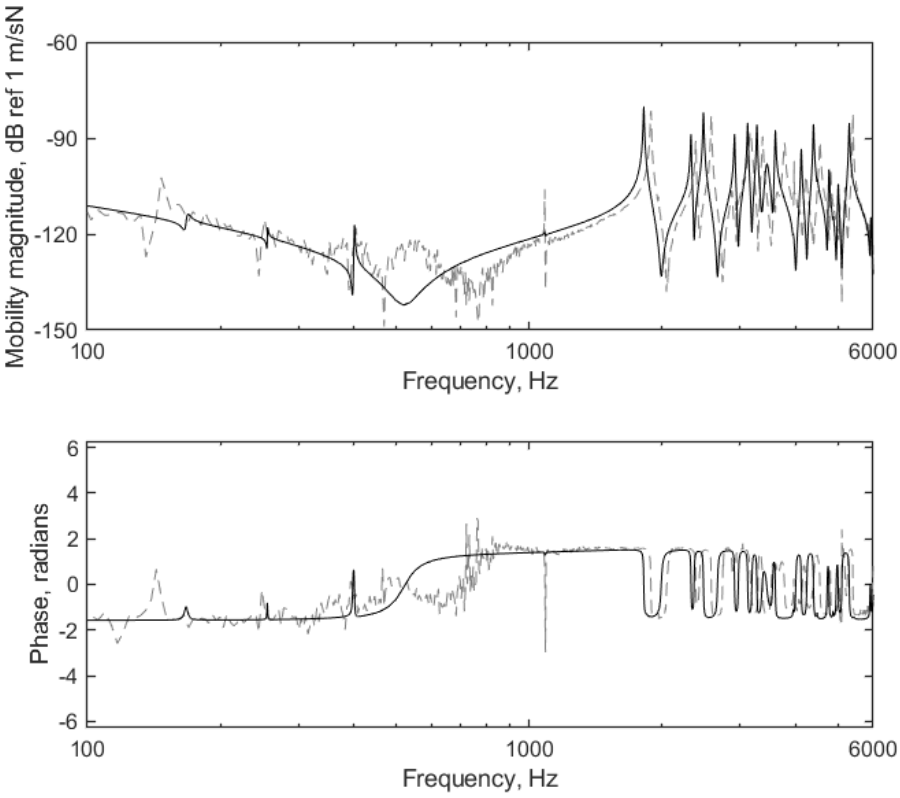

Figure 21: Radial mobility of wheel. - -, Measured; –, Predicted.

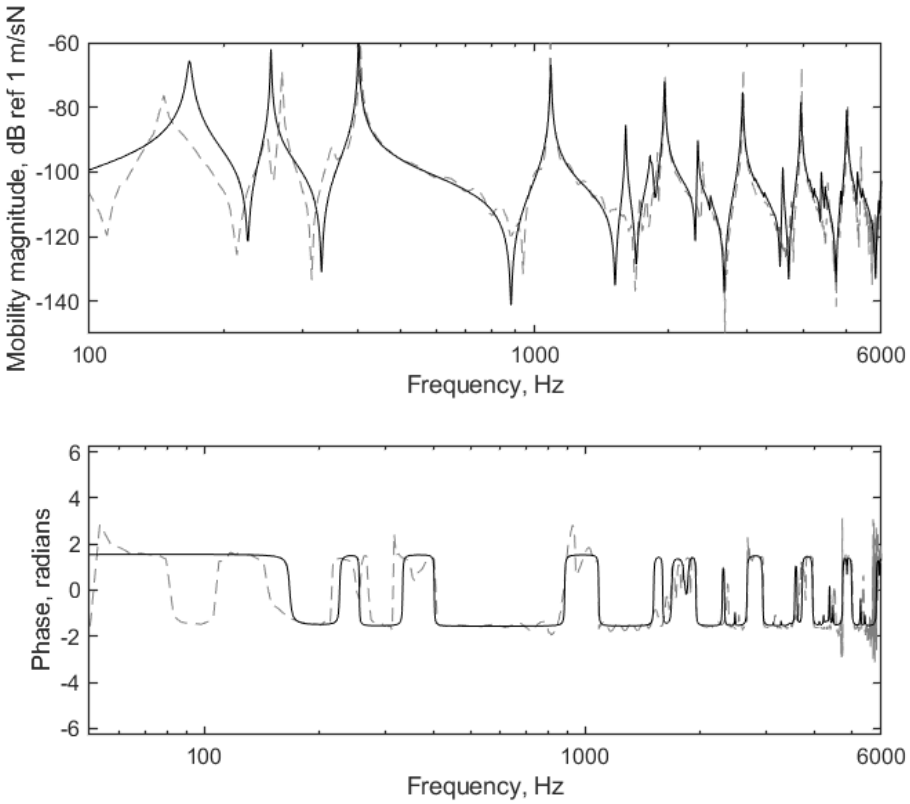

Figure 22: Axial mobility of wheel. - -, Measured; –, Predicted.

4.1.8 Sound power

Figure 23 shows the predictions of the sound power from different components. It can be seen that the largest sound power is concentrated in the frequency range below 1 kHz where the rail and sleeper mainly contribute. At low frequencies, the sleeper is the dominant source. The sound power radiated from the wheel is generally lower than those from the rail and sleeper except for frequencies around 250 Hz and above 2 kHz. The component radiated from the vertical rail vibration is generally greater than that from the lateral vibration.

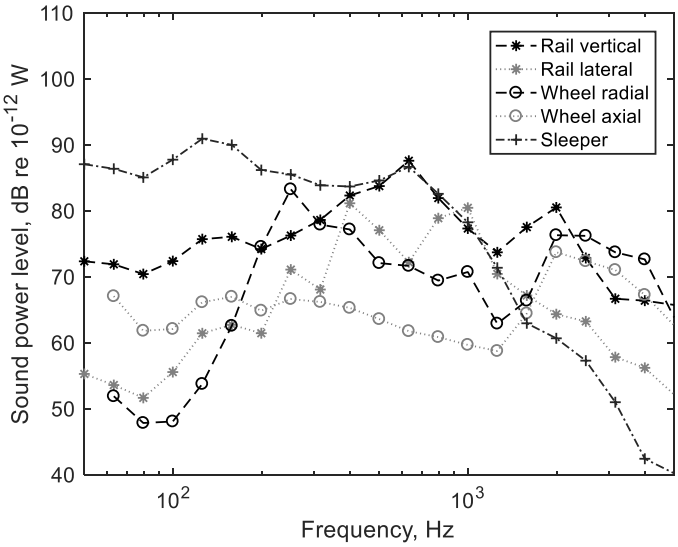

Figure 23: Predicted sound power levels from the rail, wheel and sleeper.

4.2 MODEL OF NOISE RADIATED BY THE BOGIE

The noise radiated by the bogie frame can be calculated with a three-dimensional Boundary Element Method (BEM) model after the vibration results are obtained from the previous structure-borne sound FEM analyses based on the full bogie model. For the BEM analysis, a mesh of the outer surface of the bogie frame has been created with triangle elements (Figure 24). The average element size is 40 mm, which gives at least 8 elements per wavelength for frequencies up to 1 kHz, which is sufficient.

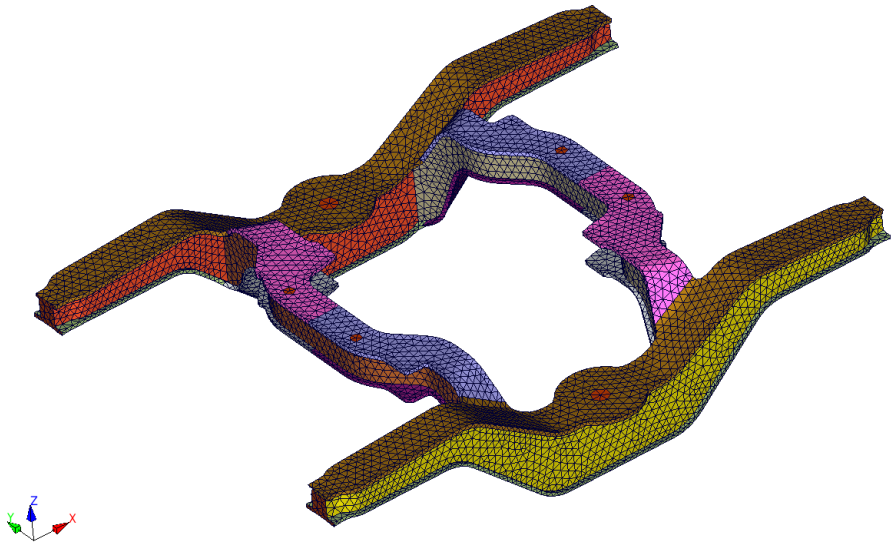

Figure 24: BEM model for radiated noise analysis.

The mesh size of the FEM model used in structural analysis is usually finer than required for acoustic BEM analysis. Therefore the surface velocities obtained from FE calculations cannot be directly used for the BEM calculation; they need to be mapped to the BEM mesh. This mapping procedure must be carried out for each frequency used in the BEM calculations. Figure 25 shows an example of the visualised velocities on the BE mesh after the mapping from the FE mesh.

In the first step of the BEM calculations the sound pressures on the bogie surface are obtained from the surface velocities. The radiated sound power noise can then be calculated by

$$W_{rad} = \frac{1}{2}\int_{\Gamma} \mathrm{Re}(p^{*}v)d\Gamma \qquad (4.1)$$

where p^* is the complex conjugate of the complex sound pressure amplitude p, v is the normal velocity amplitude on the boundary surface and Γ is the boundary surface.

The vibration of the bogie frame was calculated with the full bogie FE model under unit vertical forces applied on the four wheel/rail contact points. The sound power radiated by the bogie frame was calculated by Eq. (4.1) for this load case, as shown in Figure 26. The radiation efficiency for this load case is shown in Figure 27; it is seen to reach unity above approximately 800 Hz. This is given by

$$\sigma = \frac{W_{rad}}{\frac{1}{2}\rho c \int_{\Gamma} |v|^2 d\Gamma} \tag{4.2}$$

where ρ is the density of air and c is the speed of sound.

This load case is used here for demonstration of the methodology for the virtual test purpose. In real applications, the wheel/rail force should be obtained from the model described in Section 2, where the track properties and roughnesses of wheel/rail must be considered.

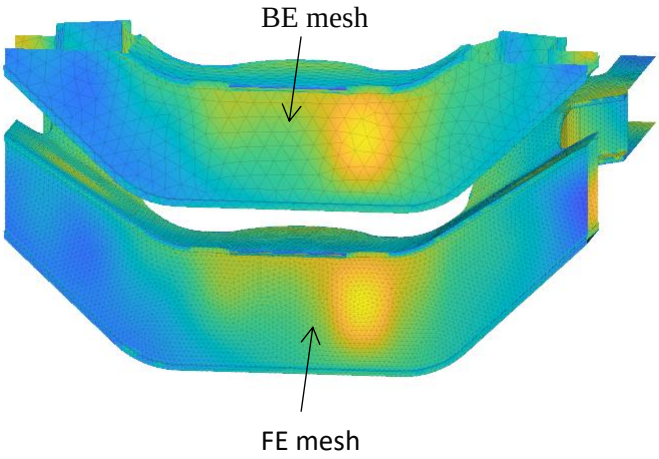

Figure 25: Examples of velocities on FE and BE meshes at 790 Hz.

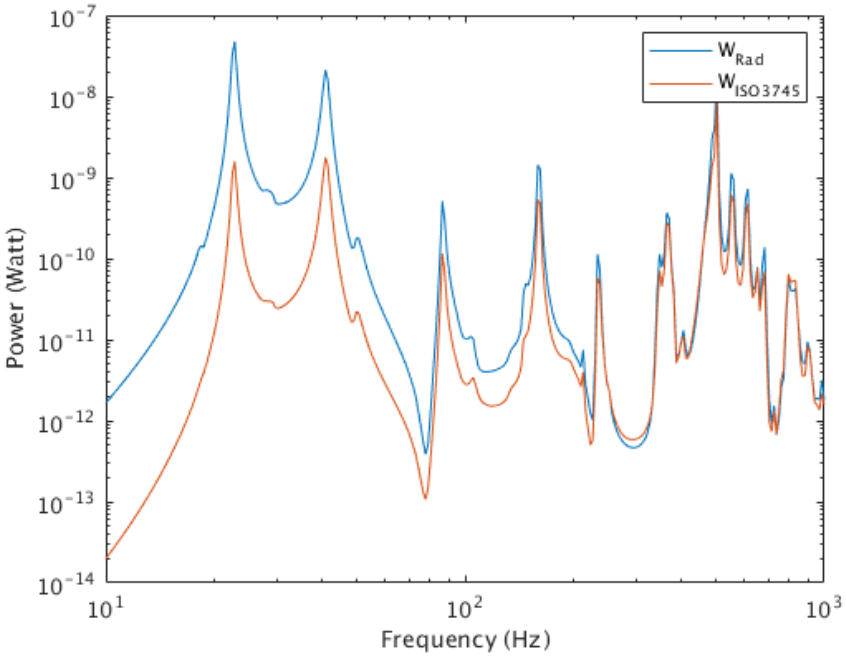

Figure 26: The radiated power by the bogie frame under the unit force at four wheel/rail contact using the direct method and virtual ISO3745.

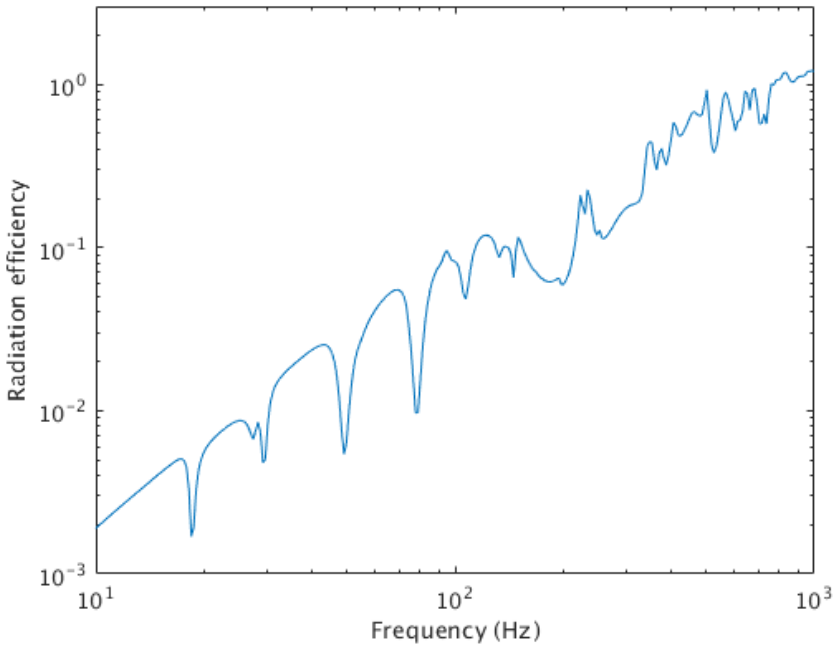

Figure 27: The radiation efficiency of the bogie frame.

Eq. (4.1) may be referred to as a direct method to calculate the sound power by BEM. A more practical way using the BEM is to use far-field sound pressures to predict the sound power, analogous to the measurement method specified by ISO 3745 [12]. In this method, sound pressures are calculated for 20 microphone positions defined according to ISO 3745. The sound power is given by

$$W_{rad} = \frac{1}{2\rho c}\overline{|p|^2}\cdot S \tag{4.3}$$

where *p* is the sound pressure in the far field which is averaged over the microphone positions and *S* is the surface area of a sphere with its radius defined by the distance between the microphone and the centre of the radiating object. This is set to 4.8 m to satisfy the requirement that it is at least 2.5 times the size of the source [12].

Using Eq. (4.3) to calculate the sound power is a numerical implementation of ISO 3745, which can be considered to be a virtual sound power test method [13]. Figure 26 also shows the radiated power calculated using Eq. (4.3). At frequencies below 200 Hz, the radiated power by the ISO 3745 method does not agree well with the direct calculation by Eq. (4.1). This is due to the fact that only 20 field points are used in the ISO 3745 method and they are affected by the near field at low frequency. Above 200 Hz, the agreement between the two methods improves and the difference is less than 3 dB.

A practical advantage of using Eq. (4.3) is that the so-called acoustic transfer vectors (ATVs) can be used. ATVs define relationships between the normal velocities of the radiating structure and the sound pressure at points in the acoustic field around the structure. They are obtained by solving the same BEM problem but with unit normal velocities. Therefore the ATVs can be pre-calculated, stored and then repeatedly used for the FEM model in subsequent dynamic analyses to predict the radiated noise, provided the geometrical shape of the radiating structure does not change. As the ATVs are usually smooth functions of frequency, they can be calculated at a limited number of frequencies and then interpolated to obtain the finer frequency resolution required for structural radiation. This can further save computational costs compared with using Eq. (4.1) directly.

4.3 SOUND FIELD BELOW THE VEHICLE

To determine the sound pressure incident on the floor of the train a statistical energy analysis (SEA) model of the cavity beneath the train is developed. The sound pressure in this region is assumed to be sum of the direct sound and the reverberant sound caused by reflections from the train floor and the track. The direct sound and reverberant sound are discussed below in Sections 4.3.1 and

4.3.2. The results from these two components are given in Section 4.3.3; Section 4.3.4 compares the overall results with the experiments.

The cross-section profile of the train is given in Figure 28. The train floor is about 1.2 m above the ballast. As additional equipment is mounted beneath the train floor, the effective height of the train floor was set to be 0.6 m in this work. The length of the vehicle is 17 m.

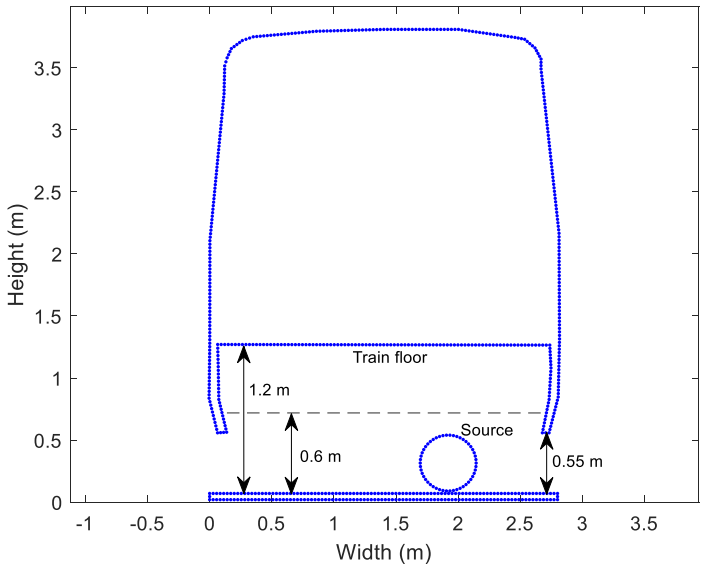

Figure 28: Two-dimensional cross-section of the train.

4.3.1 Direct sound at the receivers

In the field measurements described in Appendix A.6, an omnidirectional source with a diameter of 0.45 m was installed on the ground beneath the train. When calculating the direct sound, it is represented as a point source (S_1) about 0.225 m above the ground and 2.95 m the end of the vehicle. An image source S_2 is created to model the reflected path due to the ground. The sound at the receivers located on the centreline of the train at a height of 0.32 m is calculated by summing sound pressure due to the direct path and reflected paths, see Figure 29.

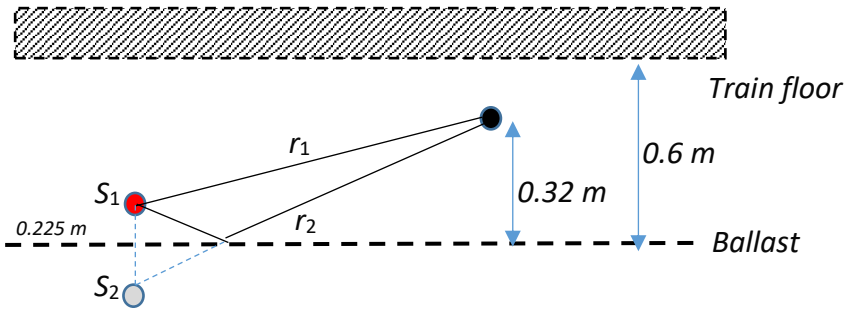

Figure 29: Direct sound including ground reflection.

The sound pressure at the receivers due to the direct source S_1 is expressed as

$$p_1 = i\omega\rho_0 q \frac{e^{-ikr_1}}{4\pi r_1} \tag{4.4}$$

where q is the source strength. As the source strength in the experiments is unknown, in the simulations a unit source strength was used. The combined sound pressure from source S_1 and the image source S_2 is expressed as

$$p = p_1 + R p_2 = p_1(1 + R \frac{r_1}{r_2} e^{-ik(r_2 - r_1)}) \tag{4.5}$$

where R is the reflection coefficient of the ground, which could be derived from the impedance of the ballast. The impedance is determined based on the Delany-Bazley model [14] for a layer of ballast of thickness 0.5 m. The flow resistivity is set to 50 kPa.s/m^2. The ground reflection coefficient is expressed as

$$R = \frac{z_n' \cos(\theta) - 1}{z_n' \cos(\theta) + 1} \tag{4.6}$$

Results of the direct sound are given in Section 4.3.3.

4.3.2 Reverberant sound

A SEA model was created to investigate the reverberant sound below the train. The total length of the vehicle is 17 m, which was divided into 10 subsystems, see Figure 30. The height of the train floor was set to be 0.6 m above the ground.

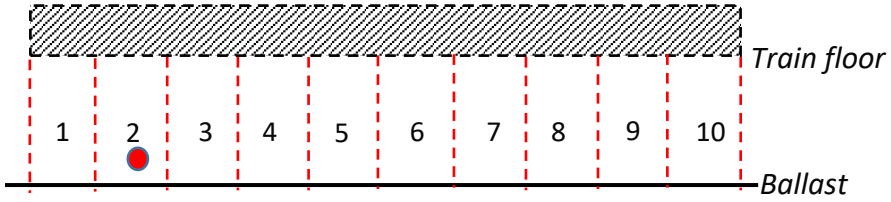

Figure 30: SEA model for investigating acoustic behaviour below the train floor.

The energy flow in the SEA model is illustrated in Figure 31.

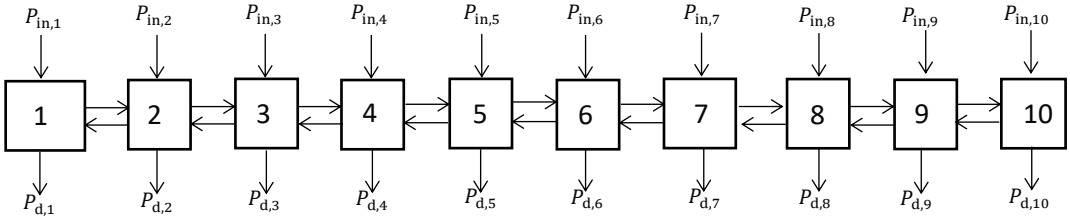

Figure 31: Energy flow in the SEA subsystems.

The power input to the SEA system is assumed to be due to the first sound reflection from the train floor. The input power to the SEA system was calculated in each segment by integrating the normal sound intensity over the area of the floor.

$$P_{in,i} = \int_{S_i} \mathrm{I}_z \mathrm{d}S \tag{4.7}$$

where I_z is the normal sound intensity on the train floor. p is the sound pressure amplitude on the train floor calculated using the model in the previous section and θ is the angle to the normal. If the coupling loss factor $\eta_{i,j}$ and dissipation loss factor η_i are known, the energy in each subsystem can then be calculated from the SEA equations. The coupling loss factor $\eta_{i,j}$ between two segments and the dissipation loss factor η_i of a segment are given by [15]

$$\eta_i = \frac{c_0 S_i \alpha_i}{4\omega V_i} \tag{4.8}$$

$$\eta_{i,j} = \frac{c_0 S_{i,j} \tau}{4\omega V_i} \tag{4.9}$$

where c_0 is the sound speed, S_i is the total surface area of the segment i, α_i is the average absorption coefficient for subsystem i, V_i is the volume for subsystem i, $S_{i,j}$ is the area of the adjoining partition between cavities i and j. τ is transmission coefficient of this partition. As the partition between subsystems is completely open, Forssén et al. assumed a very strong coupling between two subsystems [15], setting τ equal to 1. To calculate the dissipation loss factor, the absorption coefficient is required. This is based on the following assumptions:

(a) The absorption coefficient of the sides of the area is expected to be 1 as the sides are opening to free field.
(b) The absorption coefficient on the train floor is set to be 0.3 to model the scattering and absorption on the train floor. This value is chosen as it gives the best agreement with the measurements in the next section.
(c) The absorption coefficient of the ballast has been measured in a reverberation chamber based on the Sabine formula [16]. In the present case the ballast forms 4/5 of ground, the remainder being the surface of the sleepers.
(d) The sleepers are made of concrete, so the absorption coefficient of sleepers is set to be 0.

The solution to the SEA model gives the energy E in each subsystem. From this, the rms reverberant sound pressure can be calculated by

$$p_{rev} = \sqrt{\frac{\rho_0 c_0^2 E}{V}} \tag{4.10}$$

The results are given in the next Section.

4.3.3 Prediction of total sound pressure at the measured locations

After the direct sound and the reverberant sound have been calculated, the total sound at the measurement locations is determined as the incoherent sum of these two components. Examples of the direct sound, the reverberant sound and the total sound in 1/3 octave bands are plotted in Figure 32.

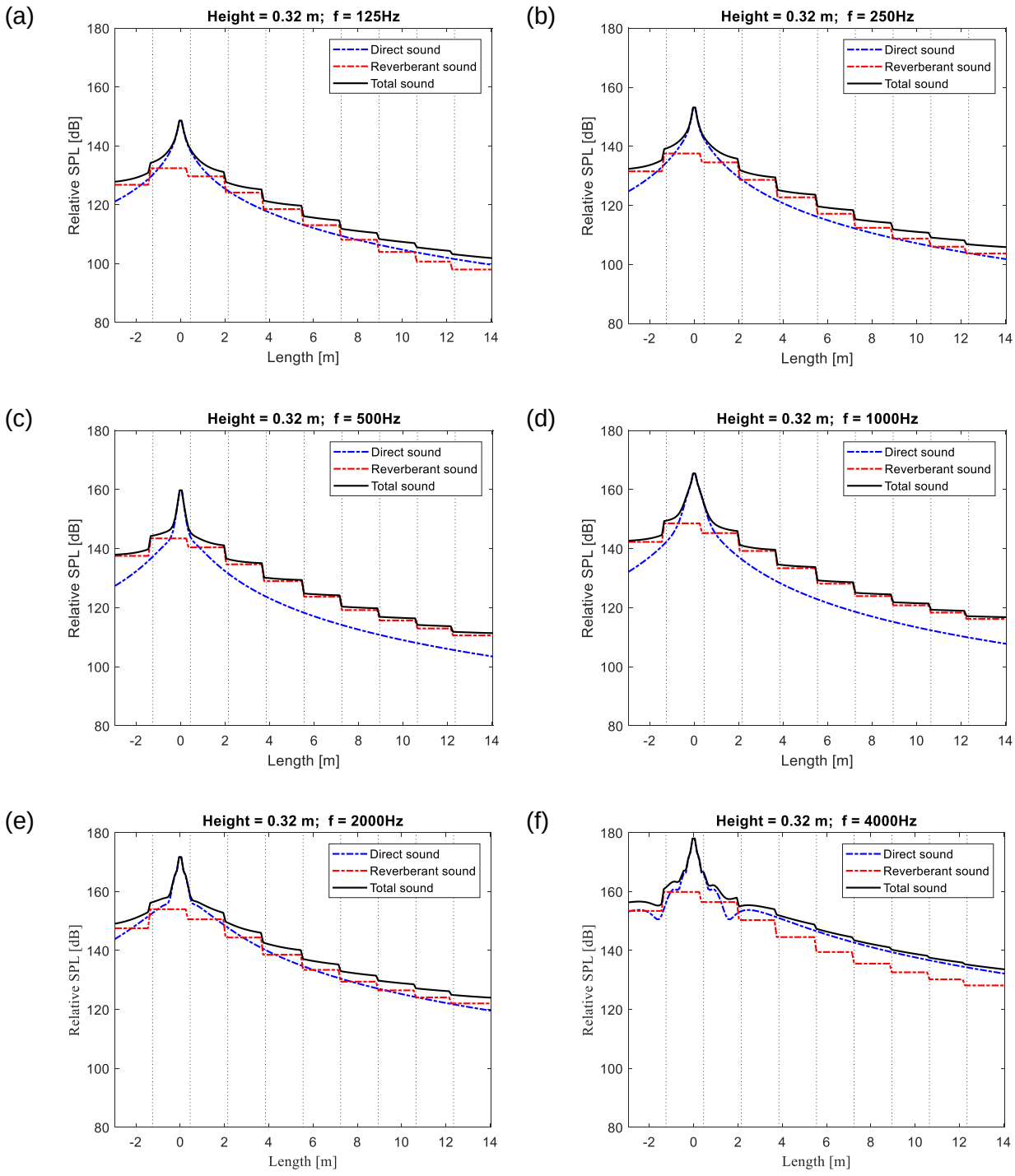

Figure 32: Sound pressure at *h* = 0.32 m obtained by using the SEA model for a unit power source.

4.3.4 Comparison with measured sound below the train

Field measurements were conducted to validate the SEA model, as described in Appendix A.6. The measured sound pressure levels at height h = 0.32 m above the ground were used to validate the predictions. Examples of the che comparisons are shown in Figure 33. As the source strength in the measurements is unknown, the predicted values were adjusted in level to correspond with the measured ones.

From this comparison between the SEA predictions and the field measurements, and other frequency bands not shown here, it can be concluded that below roughly 3 kHz, the decay with distance from the SEA predictions agrees reasonably well with the measurements. The assumptions used, such as using an absorption coefficient of 0.3 for the train floor are acceptable. Above 3 kHz, the measured sound pressure below the train floor decays slightly faster than the SEA predictions. This could be compensated by using a higher absorption coefficient for the train floor.

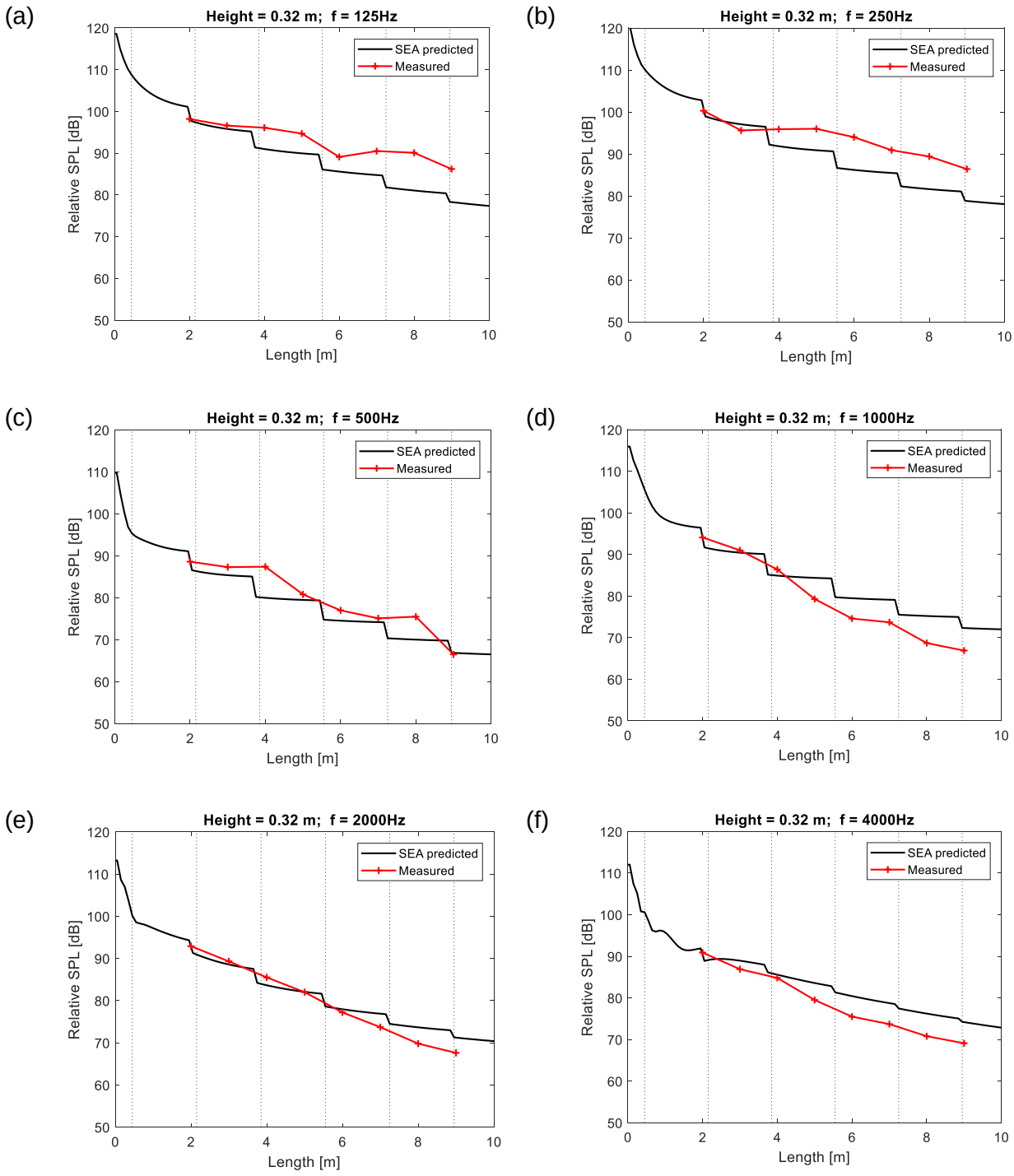

Figure 33: Comparisons between the predicted and measured sound beneath train floor for an omnidirectional source under the bogie.

4.3.5 Application to noise from a running train

To apply this approach to the running train, the sound sources consisting of the wheels, rails and sleepers (and the bogie frame) should be taken into account. The same procedure is used to determine the sound incident on the train floor. First the direct sound is calculated using equivalent sources for each component. The strength of these sources is set according to the sound power predicted using TWINS (Figure 23). Then the reverberant sound is calculated using the SEA model with the input power in each subsystem determined from the first sound reflection from the train floor.

The sound power from the wheel estimated using TWINS is divided into two components. In TWINS the power from the radial modes is assigned a monopole directivity whereas the power from the axial modes is assigned a dipole directivity. The direct sound from the wheel is therefore determined according to these two types of equivalent source which are located at the centre of the wheel.

The rail noise is calculated using an equivalent source model [17]. As shown in Figure 34, an array of correlated point sources is defined along the rail. These sources are assigned source strengths according to the vibration at the corresponding position; this vibration is determined using the same vibration model as used in TWINS. Examples of the direct sound incident on the train floor are shown in Figure 35.

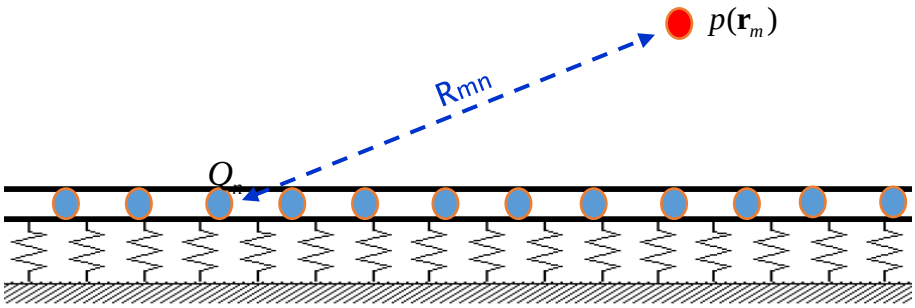

Figure 34: Equivalent noise source model used for the rail.

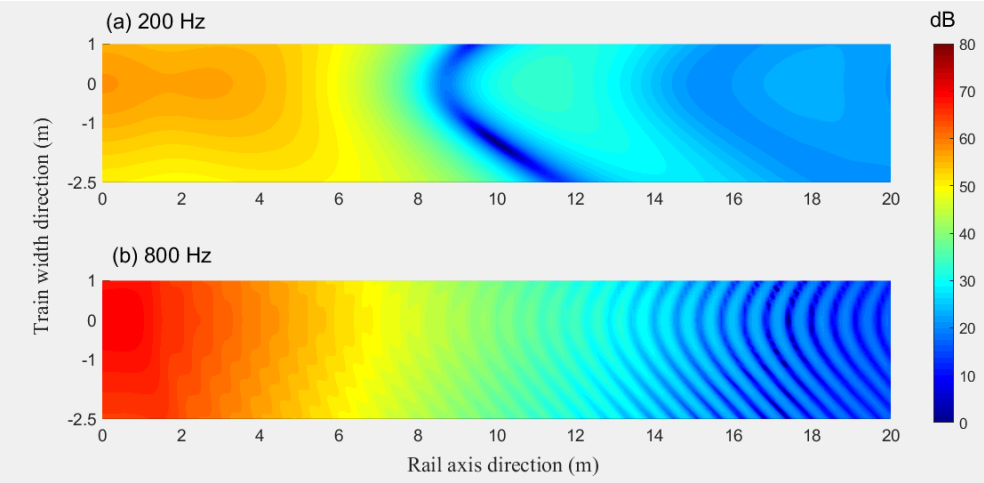

Figure 35: Examples of the direct sound pressure incident on the train floor due to radiation from the rail.

4.4 SOUND FIELD AROUND THE SIDE OF THE VEHICLE

To determine the sound field around the side of the train, the use of traditional approaches such as the three dimensional boundary element method will be computationally expensive. In this study, a wavenumber-domain boundary element approach (2.5D BE approach) was developed to predict the transmission of noise from the rail or the wheel to the train outside surfaces. The procedure has been validated by using field measurements described in Appendix A.6.

4.4.1 The 2.5D BE model

The 2.5D method relies on the fact that the geometry is invariant in the axial direction, denoted x. Thus the BE model of the train cross-section can be formed in two dimensions and the third dimension is solved in the wavenumber domain.

The conventional three dimensional boundary element method is based on the boundary integral equation for circular frequency ω [18]

$$p(x,y,z) = -\int_S (i\rho\omega v(x,y,z)\psi(x,y,z) + p(x,y,z)\frac{\partial\psi(x,y,z)}{\partial n})dS \qquad (4.11)$$

where *S* is the surface of the vibrating object, $p(x,y,z)$ is the sound pressure at receiver P, $v(x,y,z)$ is the normal velocity on the vibrating surface and $\psi(x,y,z)$ is the Green's function (fundamental

solution to the wave equation). The Fourier transform pair of the sound pressure $p(x, y, z)$ in the x direction is expressed as

$$p(\kappa, y, z) = \int_{-\infty}^{\infty} p(x, y, z) e^{i\kappa x} dx \tag{4.12}$$

$$p(x, y, z) = \frac{1}{2\pi} \int_{-\infty}^{\infty} p(\kappa, y, z) e^{-i\kappa x} d\kappa \tag{4.13}$$

where κ is the wavenumber in the x direction [19]. In practice to determine the far-field pressure, the limits of the integral in Eq. (4.12) can be restricted to the range $-k_0$ to k_0 where k_0 is the acoustic wavenumber at frequency ω. However, to determine the near-field pressure also larger values of wavenumber should be included,

In equation (4.12), $p(\kappa, y, z)$ is a function of y and z, but is independent of x, so it can be calculated in the wavenumber domain by using a two dimensional model. The wavenumber domain boundary integral equation is expressed as

$$p(\kappa, y, z) = -\int_{\Gamma} (i\rho\omega v(\kappa, y, z)\psi(\kappa, y, z) + p(\kappa, y, z) \frac{\partial \psi(\kappa, y, z)}{\partial n}) d\Gamma \tag{4.14}$$

where Γ is the two dimensional boundary. $v(\kappa, y, z)$ in Equation (7) is the particle velocity in the wavenumber domain, being calculated by applying the Fourier transform to the normal velocity in the spatial domain in a similar way to Eq. (4.12). The Green's function in Eq. (4.14), $\psi(\kappa, y, z)$, has the same form as $\psi(y, z)$ in a 2D case. It is expressed as

$$\psi(\kappa, y, z) = -i \frac{1}{4} H_0^{(2)}(\sqrt{k_0^2 - \kappa^2} r) \tag{4.15}$$

where $H_0^{(2)}$ is the Hankel function of the second kind of zero order. Note that the wavenumber k_0 is replaced by $\sqrt{k_0^2 - \kappa^2}$. To save computation time it is possible to reuse the 2D calculations for different combinations of k_0 and κ.

Ground reflections can be included either by using a modified (halfspace) Green's function for a rigid ground or, if ground absorption is to be included, by including the ground surface explicitly as boundary elements. Here the Delany-Bazley model [14] is used for the ground impedance.

4.4.2 Modelling a point source in 2.5D

As the 2.5D approach is based on a 2D geometry it is not strictly possible to introduce a point source. This can be overcome approximately by using a circular mesh (representing a cylinder) of radius *a* and setting the velocity to be non-zero only over a short length:

$$v(\omega, x) = \begin{cases} 1 & x \in [-a, a] \\ 0 & x \notin [-a, a] \end{cases} \tag{4.15}$$

The corresponding velocity in the wavenumber domain is obtained by applying a Fourier transform. This approach has been verified by comparison with the analytical solution for a point source:

$$p(r) = i\omega\rho_0 q\left(\frac{e^{-ikr}}{4\pi r}\right) \tag{4.16}$$

where $p(r)$ is the pressure amplitude at radial distance r, k is the wavenumber and q is the source strength. For a pulsating sphere of radius a and velocity amplitude v_0, this is given by

$$q = 4\pi a^2 v_0 \tag{4.17}$$

Results are calculated for a unit velocity amplitude and source radius 0.005 m.

A waveguide boundary element model was created to represent the monopole source radiation, consisting of a BEM mesh of a circle with radius 0.005 m. Five field points were located in each of the *x, y* and *z* directions relative to the source to predict the sound decay, as shown in Figure 36. Each line is offset from the origin by 0.5 m (the line in the *x* direction cannot be located at (0,0) as this is inside the cylindrical BEM mesh). The field points in the *x* direction are all at the same values of (*y*, *z*). In each case, the radial distances from the field points to the source are 0.5 m, 1.16 m, 2.08 m, 4.03 m, 8.02 m, respectively. The results are plotted in Figure 37 for a frequency of 200 Hz, from which it can be seen that the 2.5D BEM results agree very well with the analytical results.

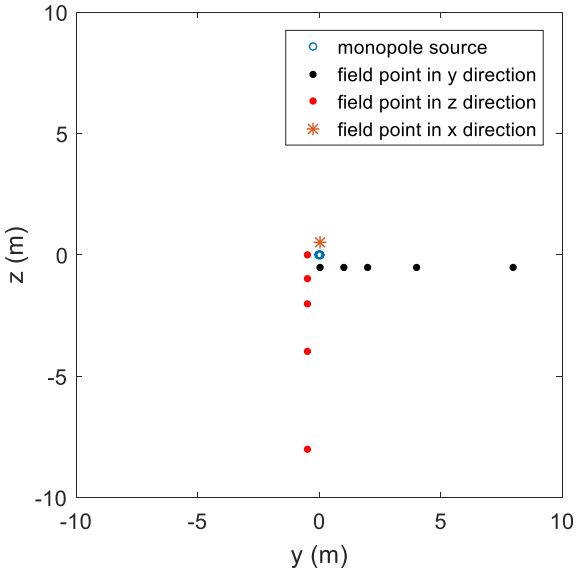

Figure 36: Field points at different distances from a monopole source.

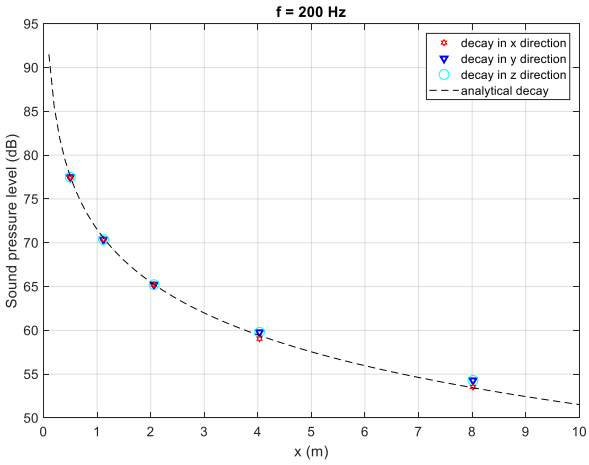

Figure 37: Sound decay obtained by using the waveguide model and by analytical method.

4.4.3 Comparison with field measurements

A 2.5D BEM mesh has been generated of the train cross-section, see Figure 38. In this model the skirts are omitted as the source is placed in the bogie region where there are no skirts. Details of the bogie frame are omitted. In the numerical model, about 800 elements were used. This can be used up to approximately 2 kHz based on the criterion that the element size should be less than a quarter of the acoustic wavelength. Five receivers on located close to the side surface of the train to represent the microphones in the measurements. The source in the numerical model has the same size as the omnidirectional loudspeaker (diameter 0.45 m). The asterisks denote CHIEF

points in the model which are used to overcome the non-uniqueness problem of the exterior BEM [18].

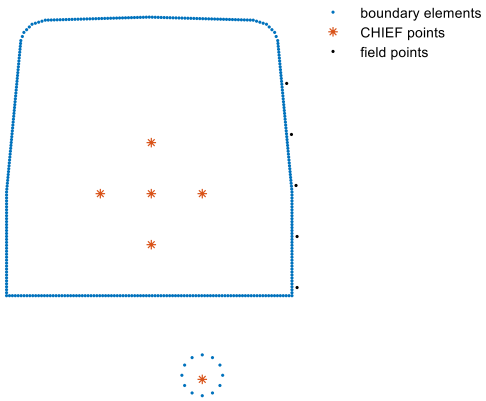

Figure 38: Numerical model of the vehicle. Blue dots donate the boundary element nodes for the source and the train, asterisks donate the CHIEF points and black dots donate the field points.

The predicted sound levels were compared with the measurements from 50 Hz to 2000 Hz. As the source strength in the measurements is unknown, the predicted sound pressure levels were calculated initially based on a unit velocity on the source and then shifted in level to correspond with the measured data. Some examples are shown below in Figure 39. Good agreement can be seen in terms of the sound pressure level distribution. To extend these results to higher frequencies would require a finer BEM grid and thus more computational time; this has not been explored in the current work.

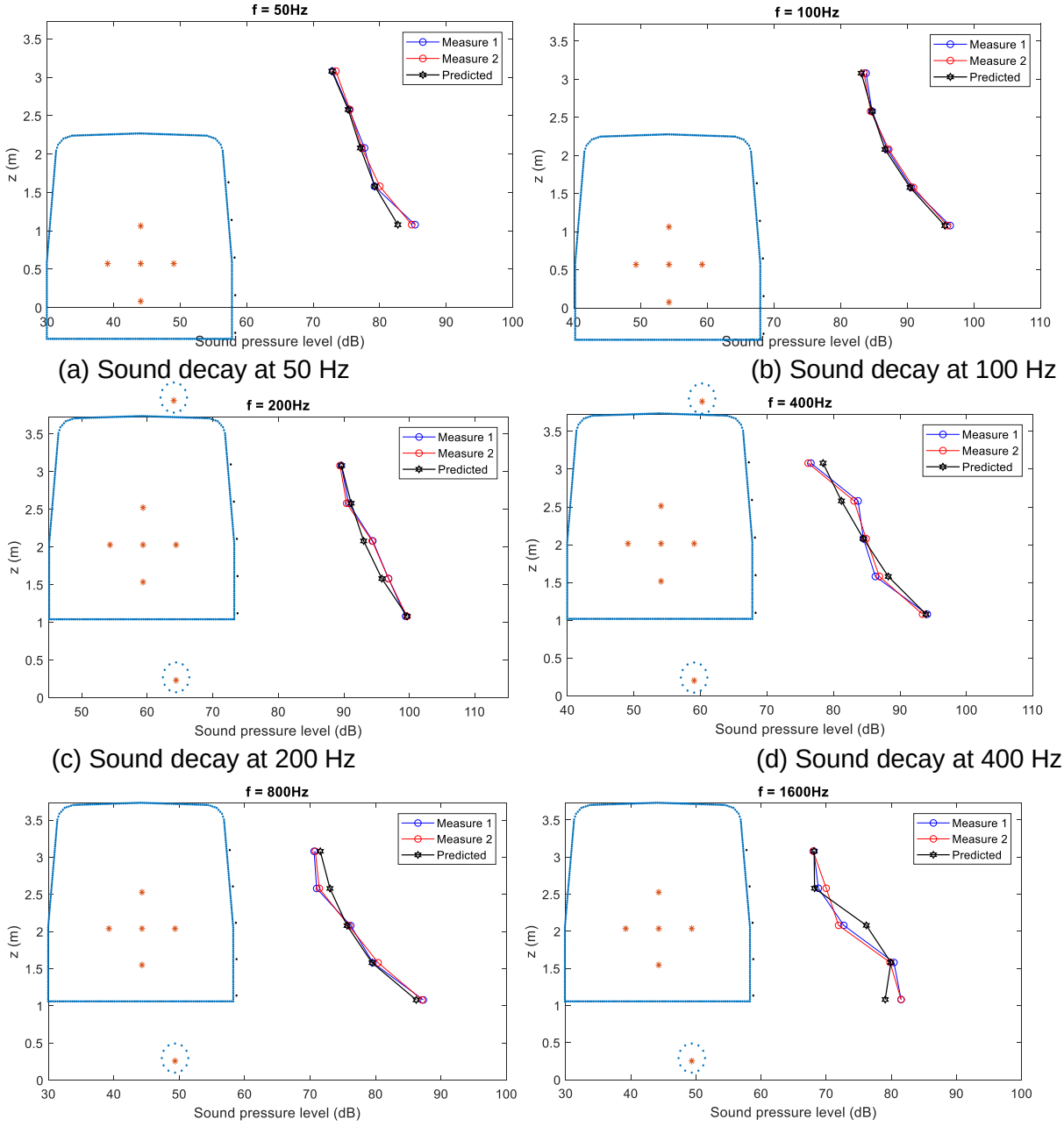

(a) Sound decay at 50 Hz

(b) Sound decay at 100 Hz

(c) Sound decay at 200 Hz

(d) Sound decay at 400 Hz

(e) Sound decay at 800 Hz

(f) Sound decay at 1600 Hz

Figure 39: Sound pressure levels on train side wall due to monopole source under the train.

4.4.4 Application to noise from a running train

To apply the approach to the noise from a running train, separate BEM calculations are performed for each source: wheel axial modes (dipole sources), wheel radial modes (monopole sources), rail vertical motion, rail lateral motion and sleepers. In each case the sound pressure on the train surface is calculated for a unit amplitude sound source and the results are adjusted according to the sound powers obtained from TWINS (Figure 23). Allowance is made for the fact that there are multiple wheels: four in the test bogie plus four in the adjacent bogie and four in the bogie at the other end of the vehicle. The sound pressures from each of these wheels (and the associated track vibration) are combined incoherently in a post-processing step, making use of the fact that the geometry in the model is independent of *x*.

The sound pressure is determined at the four surface-mounted microphones 1006, 1009, 1010 and 1011 shown in Figure 2. Microphones 1006, 1009 and 1011 are 0.7 m above the bottom edge of the sidewall and microphone 1010 is 1.5 m above it.

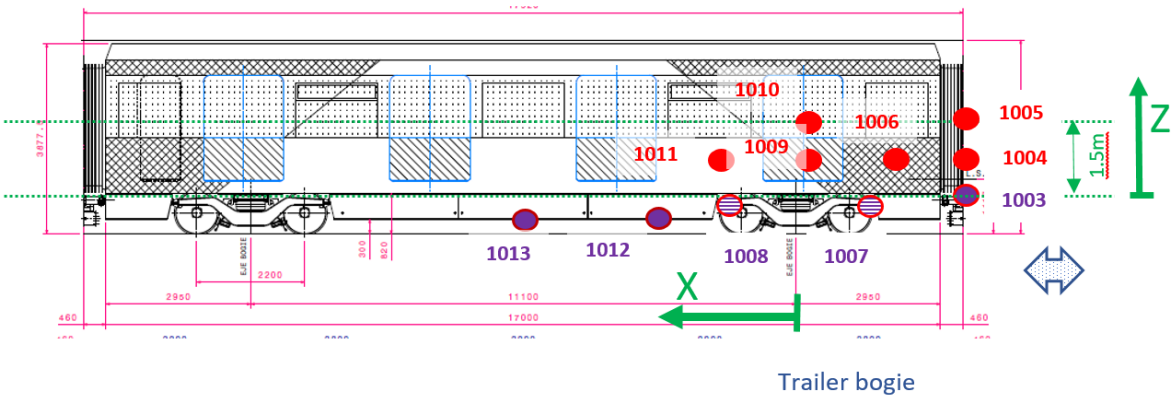

Figure 40: Locations of microphones on the side of the train.

Three source locations were chosen to represent the wheel as shown in Figure 41. At each position, either a monopole or a dipole are used to represent the radial and axial components of the wheel radiation respectively. The absorption of the ballast was modelled by including an acoustic impedance boundary condition on its top surface. The train body is modelled without the fairing as this is not present in front of the bogie region.

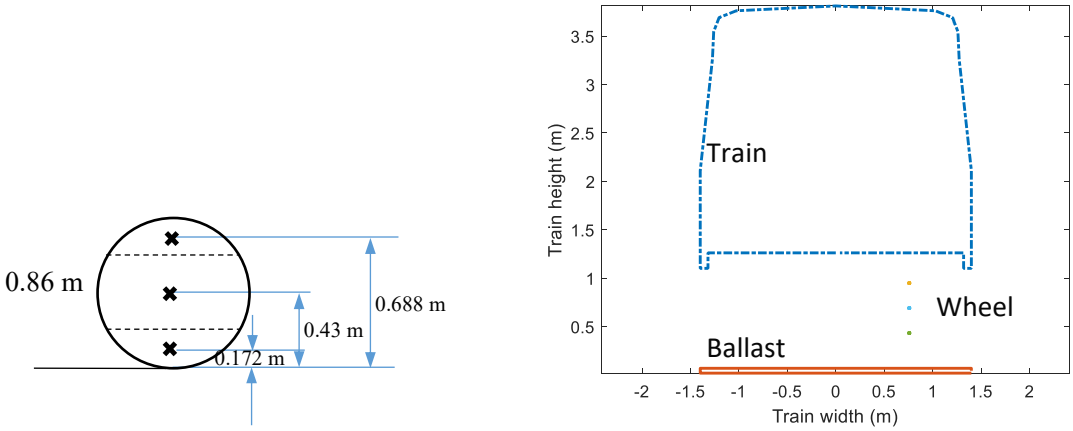

Figure 41: Left: locations of sources representing the wheel. Right: BEM mesh used for the wheel sources.

The overall sound pressure at the receivers on the side wall was calculated by averaging the mean-square sound pressure over the three source positions. As shown in figure 5 there are only small differences between the results for the three source positions.

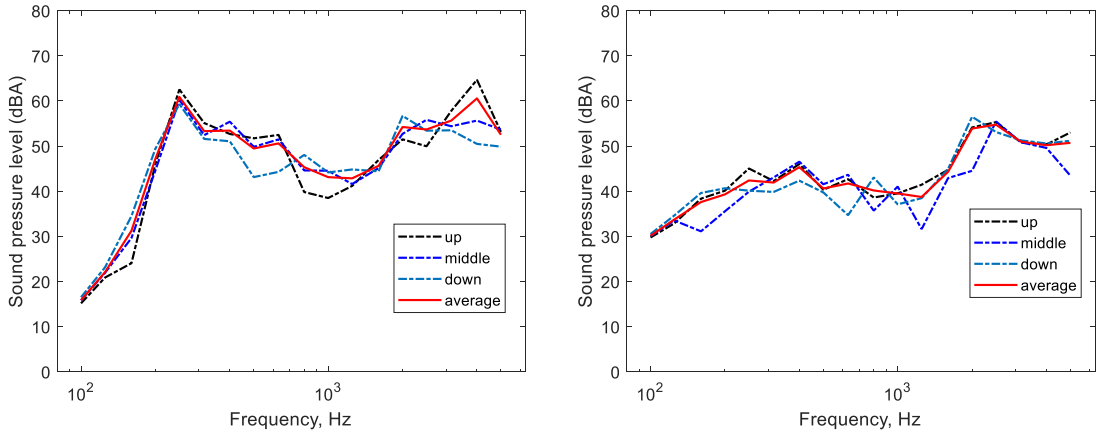

(a) Wheel axial component (b) Wheel radial component

Figure 42: Sound pressure level at example receiver location showing separate results from the three source positions and the average.

The sound radiation of the rail is calculated by using a BEM mesh for the rail which is assigned normal velocities corresponding to either vertical or lateral rigid motion. Two models were created,

one without the fairing on the train body and the other with the fairing, see Figure 43. In both cases the rail foot is 0.02 m above the surface of the ballast. The distribution of rail vibration the *x* direction was obtained from the TWINS model and converted to the wavenumber domain.

Similar BEM models are used for the sleeper radiation, except in this case the rail is omitted and, instead of the ballast absorption, the upper surface of the sleepers is assigned a velocity. This is derived from the vertical rail vibration and the ratio of sleeper vibration to rail vibration obtained from TWINS.

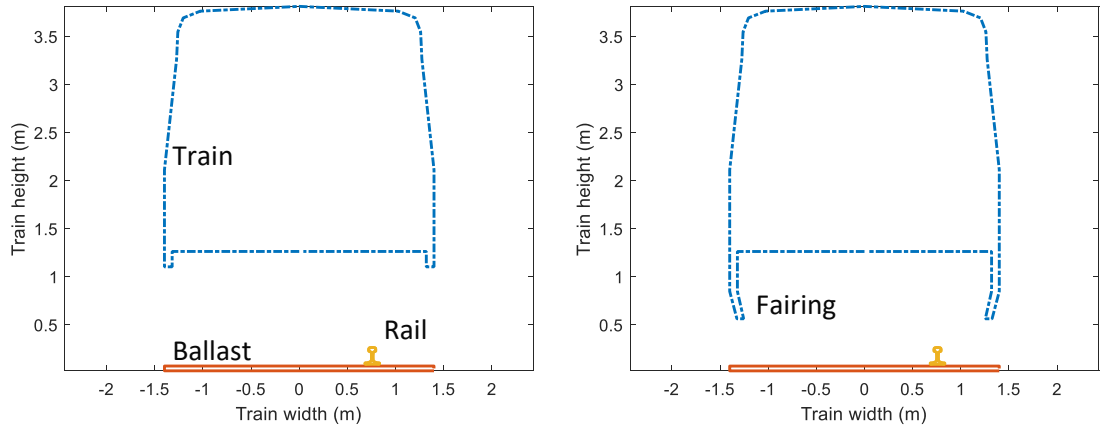

(a) Case without fairing (b) Case with fairing

Figure 43: BEM models for the rail radiation.

Example results for microphone position 1009 are shown in Figure 44, indicating that generally the fairing reduces the sound pressure level at the side wall positions.

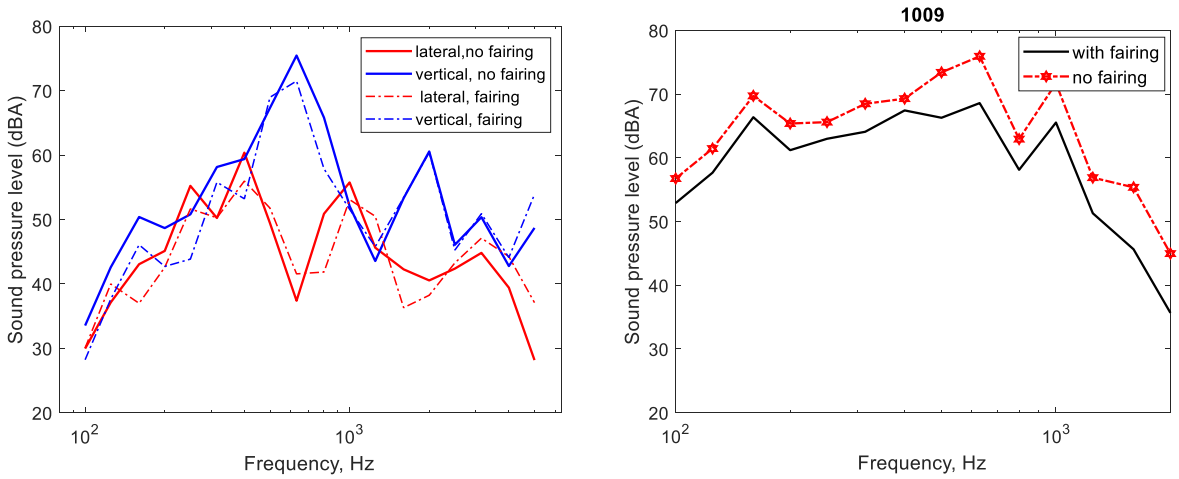

(a) Rail noise (b) Sleeper noise

Figure 44: Sound pressure levels at position 1009 due to rail and sleeper sources.

Finally the contributions of the sound at the receivers from each component are summed: the wheel axial, wheel radial, rail vertical, rail lateral and the sleeper. Account is taken of the various wheels in the train and the associated track vibration. Results are presented in Figure 45.

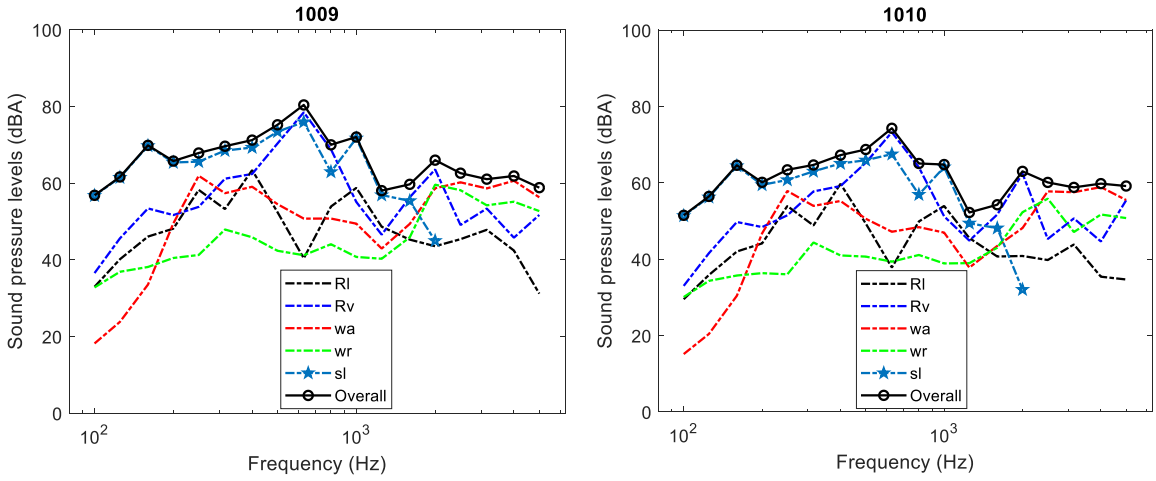

Figure 45: Overall sound pressure levels at receivers 1009 and 1010 and their components (Rl: rail lateral, Rv: rail vertical, wa: wheel axial, wr: wheel radial, sl: sleeper).

4.5 PREDICTION OF AIRBORNE SOUND WITHIN THE VEHICLE

The external sound pressure under the floor of the vehicle was determined in Section 4.3 and that on the side walls was determined in Section 4.4. To predict the airborne sound inside the vehicle, these external sound pressures should be combined with the transmission loss of the vehicle panels. In the present project these have been measured, see Appendix A.4. The power transmitted to the vehicle interior through each panel $W_{\text{trans},i}$ in each frequency band can be estimated by:

$$W_{\text{trans},i} = \left(\left(L_{p,\text{ext},i} - 6\ dB\right) - R_d\right) S_i \tag{4.18}$$

where $L_{p,\text{ext},i}$ is the external sound pressure at panel i, $R_{d,i}$ is the sound reduction index (transmission loss) of panel i and S_i is its surface area. The sound reduction index is derived on the basis that the incident sound field is diffuse. In practice the external sound field is not diffuse and the corresponding sound reduction index may therefore be affected by the form of the incident sound field.

To calculate the interior sound pressure use can be made of a number of methods:

- The Sabine formula assumes the whole interior volume is a diffuse field.
- The SEA approach sub-divides the interior volume into different coupled subsystems.
- The ray tracing approach may also be used at high frequency.
- At low frequency a finite element or boundary element model could be employed.

For example, using the Sabine formula the spatially averaged sound pressure level is given by

$$L_p = L_W + 10\log_{10}\left(\frac{T_{\text{rev}}}{V}\right) + 14 \tag{4.19}$$

where T_{rev} is the reverberation time (see Appendix A.5), V is the volume inside the carriage, and L_W is the sound power level of the total transmitted power, given by the sum of $W_{\text{trans},i}$ over all panels.

5. CONCLUDING REMARKS

A modelling approach has been presented for the noise and vibration transmission from the running gear to the vehicle interior. To the authors' knowledge this is the most comprehensive such modelling approach that has been applied in the railway industry although the techniques are relatively common in the automotive field. As well as the various component models, it relies on an extensive set of static measurements to determine input parameters and obtain complementary

transfer functions; in this case there is no model available for the car body so measurements are used to quantify the transmission to the vehicle interior.

The steps taken to model the structure-borne noise transmission are as follows:

1. Laboratory measurements of the dynamic stiffness of suspension elements, in this case the primary suspension spring, traction bar and lateral secondary damper.
2. A finite element model of the bogie frame including these frequency-dependent dynamic stiffnesses.
3. Wheel/rail interaction forces determined using a TWINS-based approach. For this the track receptances are required which are obtained from an analytical model tuned to static measurements.
4. The effect of wheel rotation is also considered using a dedicated finite element approach.
5. The finite element model of the bogie (and wheelset) and the wheel/rail interaction forces are used to determine the blocked forces at the connection points to the car body.
6. These blocked forces are combined with vibroacoustic transfer functions measured in the static tests to determine the contribution to the interior noise.

Similarly for the airborne noise transmission the following steps are followed:

1. A TWINS model of the rolling noise, including a finite element model of the wheel. The parameters for the wheel and track are selected according to static measurements (e.g. track decay rates, wheel modal damping). Measured wheel and rail roughness is used in these predictions.
2. The sound power from the bogie is determined from a boundary element model based on the FE model used for the structure-borne calculation.
3. The sound transmission in the space beneath the vehicle is determined using a statistical energy analysis approach.
4. The sound transmission to exterior panels is calculated using a 2.5D boundary element model.
5. The exterior sound pressures are combined with the transmission loss of individual panels, doors and windows to determine the airborne sound transmission to the interior.

The various models have been assembled and demonstrated here. The following specific conclusions have been reached:

- It has been verified by comparison between the modal summation approach and the direct calculation that the modal summation approach can be used with the frequency-dependent stiffness elements.
- The two models for acoustic propagation beneath and around the vehicle have been successfully verified using static measurements with a loudspeaker source.

Running measurements have also been obtained on the same vehicle as the static measurements and these will be used subsequently for validation of the modelling approach.

REFERENCES

[1] I. Lopez Arteaga et al. Description of methods for characterizing suspension elements. RUN2Rail Deliverable D4.1, December 2018.

[2] D.J. Thompson, B. Hemsworth and N. Vincent. Experimental validation of the TWINS prediction program, part 1: description of the model and method. Journal of Sound and Vibration 193, 123-135, 1996.

[3] A. R. Tufano, O. Chiello, M.-A. Pallas, B. Faure, C. Chaufour, E. Reynaud and N. Vincent. On-board indirect measurements of the acoustic quality of railway track: state-of-the art and simulations, Internoise 2019.

[4] A. R. Tufano, O. Chiello, M.-A. Pallas, B. Faure, C. Chaufour, E. Reynaud and N. Vincent. Numerical and experimental analysis of transfer functions for on-board indirect measurements of rail acoustic roughness, submitted to IWRN13, Ghent, Belgium, 2019.

[5] L. Baeza, J. Giner, D.J. Thompson, J. Monterde, Eulerian models of the rotating flexible wheelset for high frequency railway dynamics, Submitted for publication in an international journal in 2018.

[6] C. Glandier, S. Grollius, Improved full vehicle finite element model Tire Road Noise Prediction. SAE Technical paper 2017-01-1901, June 2017.

[7] L. Gagliardini, Vehicle NVH design, 2017. https://www.fp7-eliquid.eu/members/wp-documents/2013-leuven-marie-curie-graduate-school-on-vehicle-dynamics-and-mechatronics/Lecture%207%20Gagliardini.pdf

[8] D. Thompson, Railway noise and vibration: Mechanisms, modelling and means of control. Elsevier, 2009.

[9] A.T.Moorhouse, A.S.Elliott, T.A.Evans, In situ measurement of the blocked force of structure-borne sound sources, Journal of Sound and Vibration, Vol. 325, Issues 4–5, 11 September 2009, Pages 679-685

[10] P. Remington and J. Webb. Estimation of wheel/rail interaction forces in the contact area due to roughness. Journal of Sound and Vibration 193, 83-102, 1996.

[11] ISO 3095, “Railway applications – Acoustics – Measurements of noise emitted by railbound vehicles”, International Standards Organization, Geneva, 2013.

[12] ISO 3745, “Acoustics – determination of sound power levels and sound energy levels of noise sources using sound pressure – precision methods for anechoic rooms and hemi-anechoic rooms”. International Standards Organization, Geneva, 2012.

[13] M. Chargin, G. Xie, L. Dunne, and N. Hariu, Application of Shape Optimization in Structural Design for Minimizing Radiated Noise, SAE Technical Paper 2018-01-1482, 2018, doi:10.4271/2018-01-1482.

[14] M.E. Delany and E.N. Bazley. Acoustical properties of fibrous absorbent materials. Applied Acoustics, 3(2):105-116, 1970.

[15] J. Forssén, S. Tober, A.C. Corakci, A. Frid and W. Kropp. Modelling the interior sound field of a railway vehicle using statistical energy analysis. Applied Acoustics, 73(4), 307-311, 2012.

[16] R.A. Broadbent, D. J. Thompson and C.J.C. Jones. The acoustic properties of railway ballast. 8th European Conference on Noise Control, Edinburgh, UK. 2009.

[17] T. Kitagawa and D.J. Thompson. The horizontal directivity of noise radiated by a rail and implications for the use of microphone arrays. Journal of Sound and Vibration 329, 202-220, 2010.

[18] T.W. Wu, ed. Boundary element acoustics: Fundamentals and computer codes. WIT Press, 2000.

[19] C.M. Nilsson, C.J.C. Jones, D.J. Thompson, J. Ryue. A waveguide finite element and boundary element approach to calculating the sound radiated by railway and tram rails. Journal of Sound and Vibration 321, 813-836, 2009.

[20] EN 15461: 2008+A1. Railway applications – noise emissions, characterization of the dynamic properties of track sections for pass by noise measurements. European Committee for Standardization, Brussels, 2011.

[21] EN 15610:2009. Railway applications – noise emission – rail roughness measurement related to rolling noise generation. European Committee for Standardization, Brussels.

[22] ISO 3382-2:2008 “Acoustics. Measurement of room acoustic parameters. Part 2. Reverberation time in ordinary rooms”. International Standards Organization, Geneva, 2008.

APPENDIX A: STATIC MEASUREMENTS

Figure 46 gives major definitions concerning the static measurements.

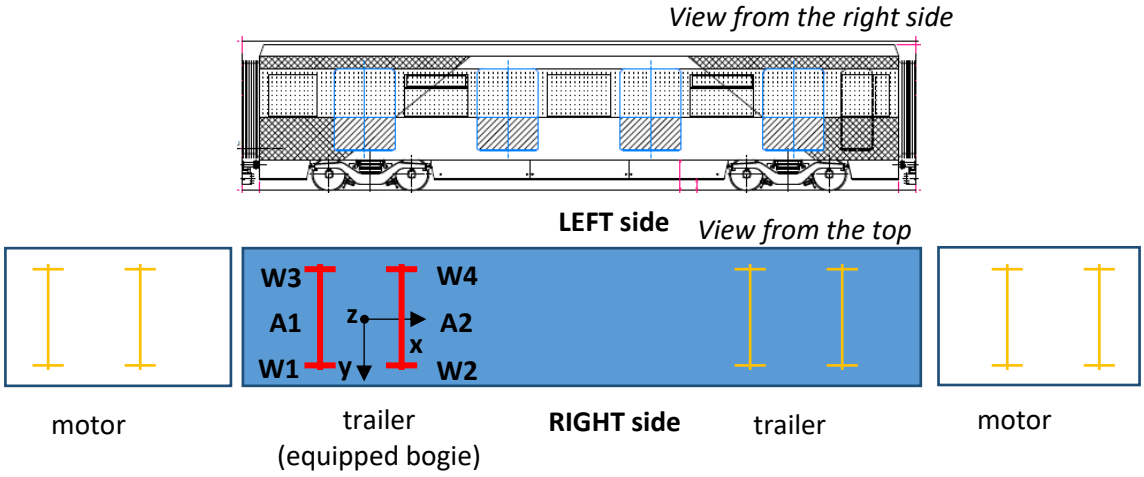

Figure 46: Definitions on the investigated trailer car: coordinate system fixed at the equipped bogie center, W1-W4: wheels, A1-A2: axles.

A.1 WHEEL CHARACTERIZATION

A railway wheel is a lightly damped structure, which can be characterised by its natural modes of vibration. For an axisymmetric wheel, these modes can be described by two identifiers (see Figure 47):

- The number of nodal diameters n,
- The form of the cross-section deformation:
  - axial modes with m nodal circles, denoted (mLn). 1Ln modes are also called rocking modes because they involve a rotation of the wheel tyre.
  - radial modes, denoted (Rn)

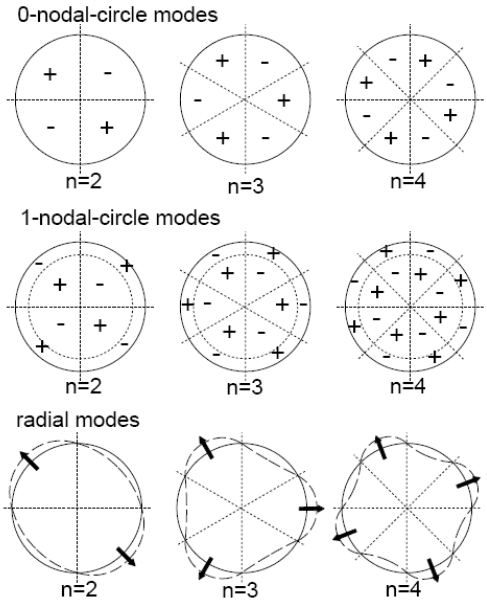

Figure 47: Examples of mode shapes of a wheel. +/- indicates the relative phase of the out-of-plane motion in each area

The considered wheel is an axisymmetric monobloc wheel (see Figure 48, Ø 860 mm, 305 to 313 kg). Consequently, a simplified experimental modal analysis (EMA) was applied. Furthermore, the wheel features two small holes in the web, three sandwich dampers providing modal damping (see Figure 49). Modes not being identified from the experimental data could be identified from a FE model.

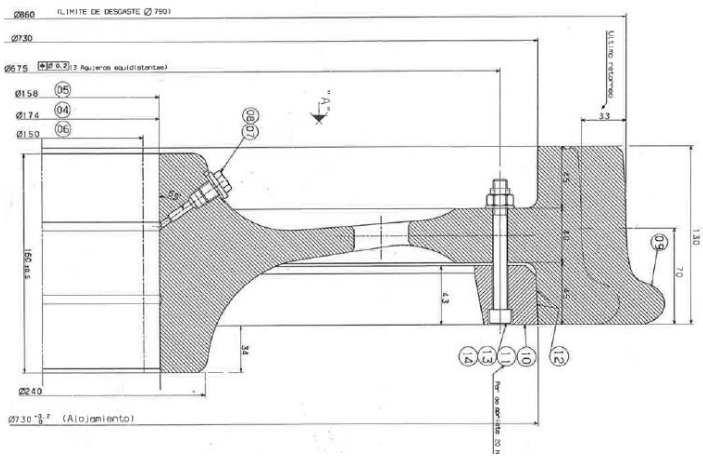

Figure 48: Wheel section

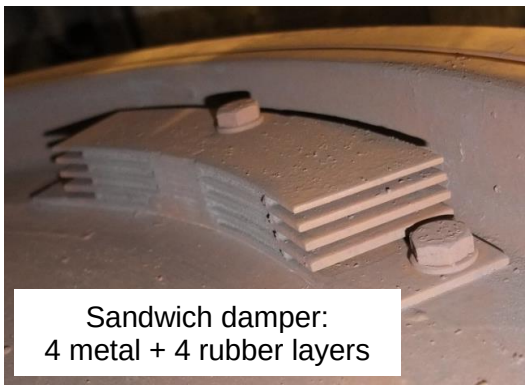

Figure 49: Details of the wheel

In order to identify the modal parameters (natural frequencies and modal damping), the wheel (lifted wheelset) is excited by an impact hammer and a single accelerometer is used to measure the response (at room temperature). The obtained transfer functions (FRF) were analysed to derive the modal parameters. The measurement positions are presented in Figure 50, whereas Table 5 summarises the information contained in the different FRFs.

FRFs cover frequencies from 0 to 8000 Hz with a step of 1.25 Hz. The chosen step is considered to be sufficient for the determination of the modal damping ξ introduced by the sandwich dampers. It is defined as follows:

$$\xi = \frac{c}{c_{crit}} = \frac{f_2 - f_1}{2f_{max}}, f_{1,2} = f\left(\left({}^{\gamma}/_{F}\right)_{max} - 3\ dB\right)$$

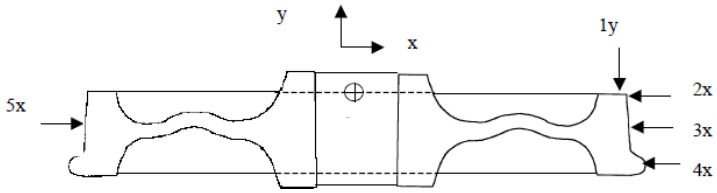

Figure 50: Scheme of the simplified wheel modal analysis

$^{\gamma}/_{F}$	**Information**
1Y-1Y	Purely axial modes denoted *0Ln*
2X-2X 2X-4X	Radial modes denoted *Rn* and axial rocking modes *1Ln*
3X-3X	Radial modes denoted *Rn*
5X-3X	Distinction between odd and even nodal diameters *n*

Table 5: EMA of the wheel – summary of measured FRFs

Table 6 summarises the identified wheel modes and their associated damping. Additionally, non-identified modes are listed in Table 7. The first rolling noise relevant mode R2 is located at 1885 Hz and the modal damping provided by the sandwich dampers is low.

	0Ln		1Ln		Rn	
n	**f [Hz]**	**ξ [%]**	**f [Hz]**	**ξ [%]**	**f [Hz]**	**ξ [%]**
0	351	1.70	-	-	-	-
1	270	0.21	-	-	-	-
2	405	0.19	2380	0.19	1885	0.21
3	1084	0.07	2875	0.17	2581	0.17
4	1961	0.13	-	-	3166	0.55
5	2939	0.03	4378	0.28	4548	0.27
6	3975	0.04	4984	0.17	5401	0.10
7	5042	0.13	-	-	6324	0.20
8	6125	0.05	-	-	-	-

Table 6: Identified modes and modal damping determined from the wheel EMA

f [Hz]	1721	1780	3373	3780	4232	4811
ξ [%]	0.43	0.66	0.26	0.44	0.52	0.16

Table 7: Additional modes and modal damping determined from the wheel EMA

Figure 51 shows the point accelerance at the nominal contact point for a radial excitation (3X-3X) and Figure 52 shows the point accelerance at the rim point for an axial excitation (1Y-1Y). These accelerances could be used to fit the numerical wheel modal base. Note, that some axle modes notable appear in the 1Y-1Y point accelerance below 2000 Hz.

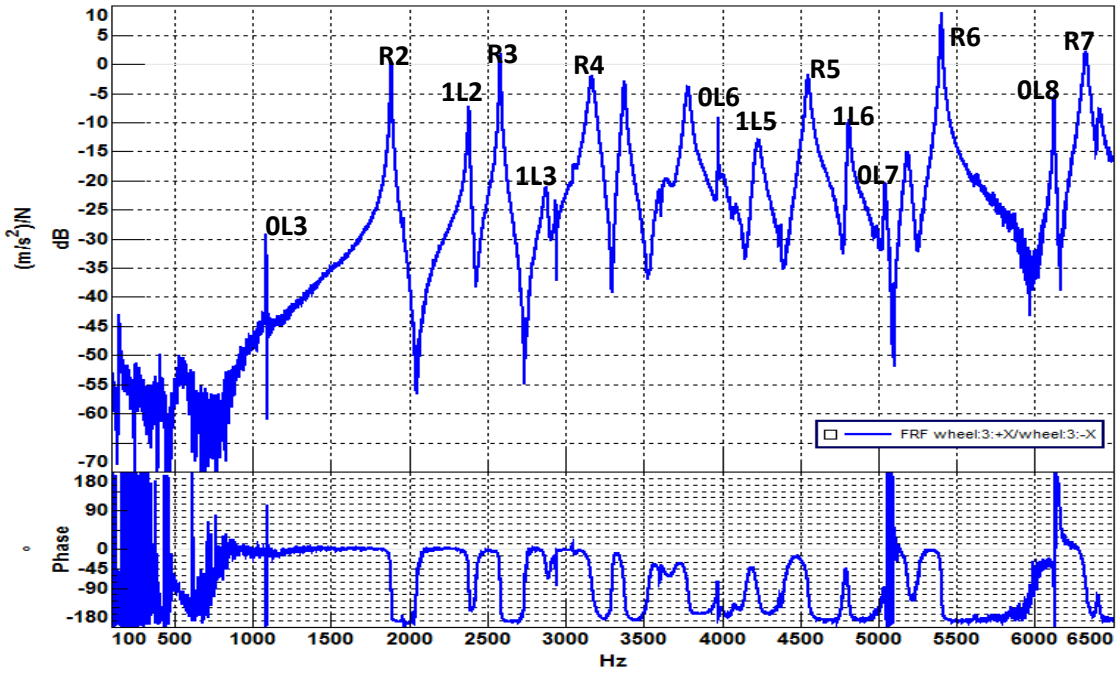

Figure 51: Point accelerance $^{Y}/_{F}$ at the radial contact point 3X

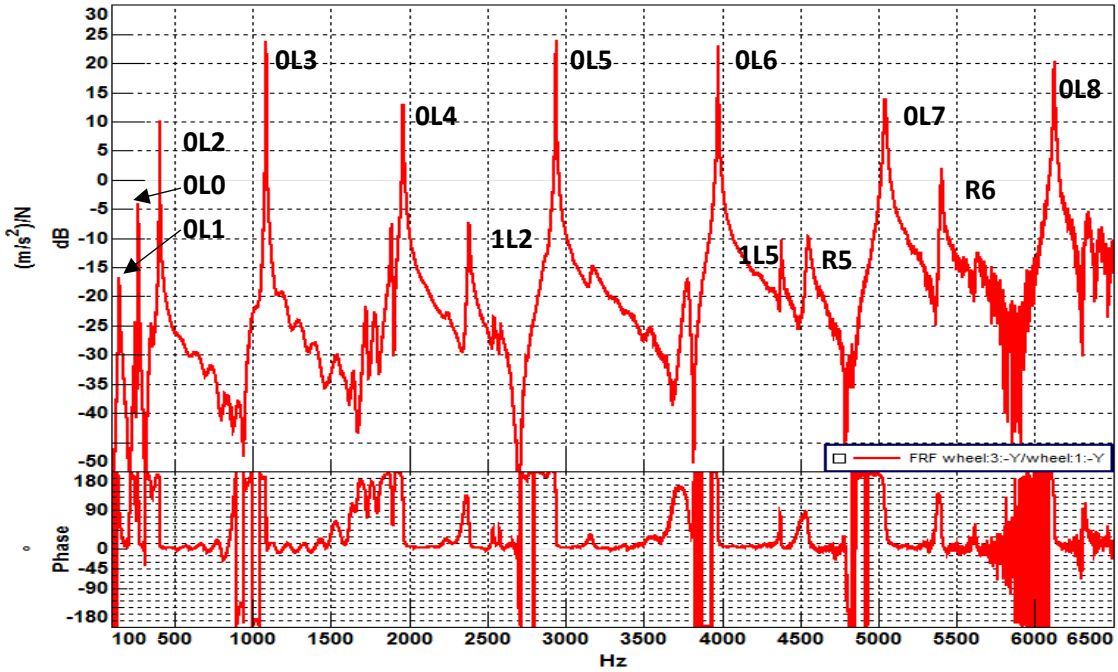

Figure 52: Point accelerance $^{Y}/_{F}$ at the rim point 1Y

A.2.1 Measurement procedure

The measurement of the TDR (Track Decay Rate) was performed according to the EN 15461 +A1 [20]. The location of the impact points on the test site is shown in Figure 53.

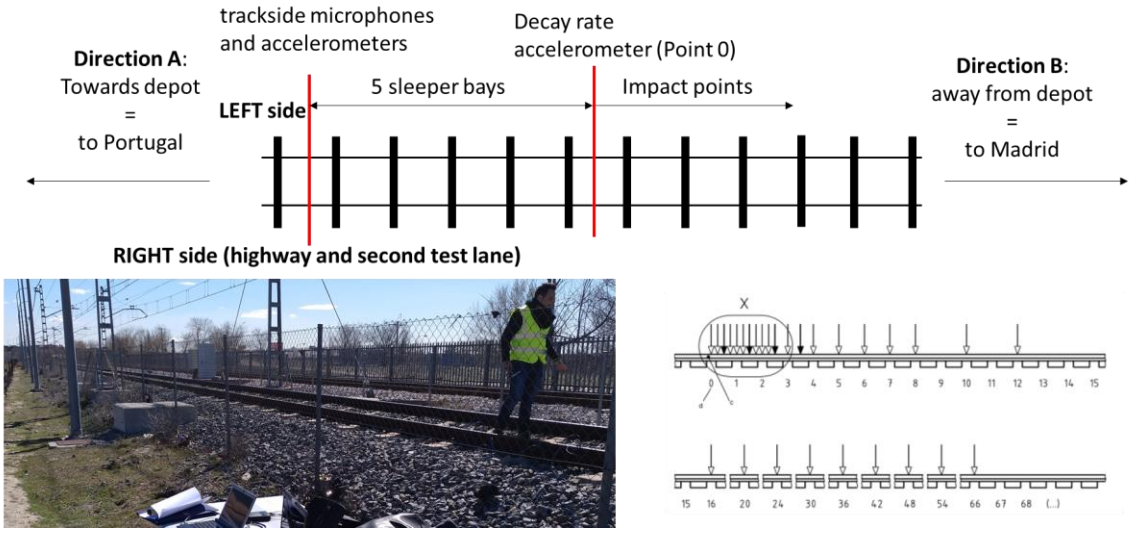

Figure 53: Impact points for decay rate measurement.

The test track consists of UIC54 rails with inclination 1/20, ballast and concrete sleepers. It should be noticed that the sleeper span was 1 m in length. The fastening accessories and the elastic pad are shown in Figure 54.

Figure 54: Rail fastening system in the test track.

Some of the final recommendations of the STARDAMP project were followed. The number of impacts at the starting point of the grid was 10 so that the FRF obtained at this point included the least error possible. Also, the analysis of the TDR values was limited to a signal reduction of -20 dB relative to the starting FRF in order to reduce the influence of the noise floor on the calculation of the spectra.

A titanium tip was used, the sampling rate was 20.4 kHz and the calculation window for the FRF was 0.2 s. The temperature of the track components measured during both the lateral and vertical tests was around 11-12 ºC.

Complementary receptance measurements were performed to illustrate the dynamic behaviour of the track over the frequency range 0-2000 Hz, according to the following procedure. FRF measurements were made using different locations for the input (force) and the output (accelerometer) and with different impact hammer and tips in order to cover different bandwidths, as indicated in Table 8.

Input / Force	Output / Accelerometer	Bandwidth / Hammer and tip	Direction
1a	1a	0-2 kHz / Small hard tip	Vertical
1b	1b	0-2 kHz / Small hard tip	Vertical
1c	1c	0-2 kHz / Small hard tip	Vertical
(a,b,c) refer to three consecutive sleepers. If the 3 FRFs look similar, then start with the other measurements (that means no voided sleeper, representative, etc.)			
Input / Force	**Output / Accelerometer**	**Bandwidth / Hammer and tip**	**Direction**
1	1	0-2 kHz / Small hard tip	Lateral
2	2	0-2 kHz / Small hard tip	Vertical
2	2	0-2 kHz / Small hard tip	Lateral
1	3	0-2 kHz / Small hard tip	Vertical
3	3	0-500 Hz / Medium plastic tip	Vertical
1	1	0-500 Hz / Medium plastic tip	Vertical
1	3	0-500 Hz / Medium plastic tip	Vertical

Table 8: Impact and measurement points for track receptances

The numbers used to define locations read as follows:

- 1 Location on top of the rail over sleeper.
- 2 Location on top of the rail in the middle of the sleeper bay.
- 3 Location on top of the sleeper, close to the fastener

A.2.2 Results

Figure 55 and Figure 56 show the lateral and vertical track decay rate, respectively.

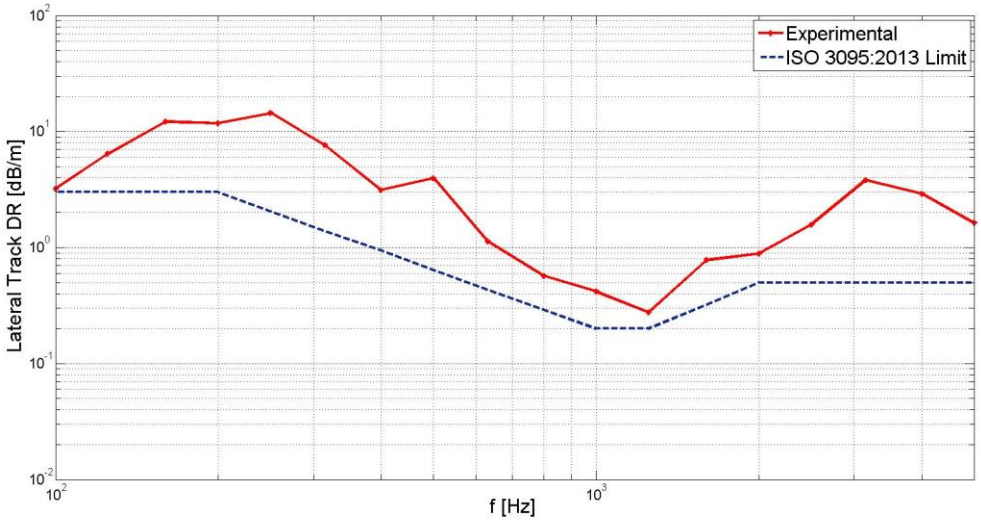

Figure 55: Lateral TDR.

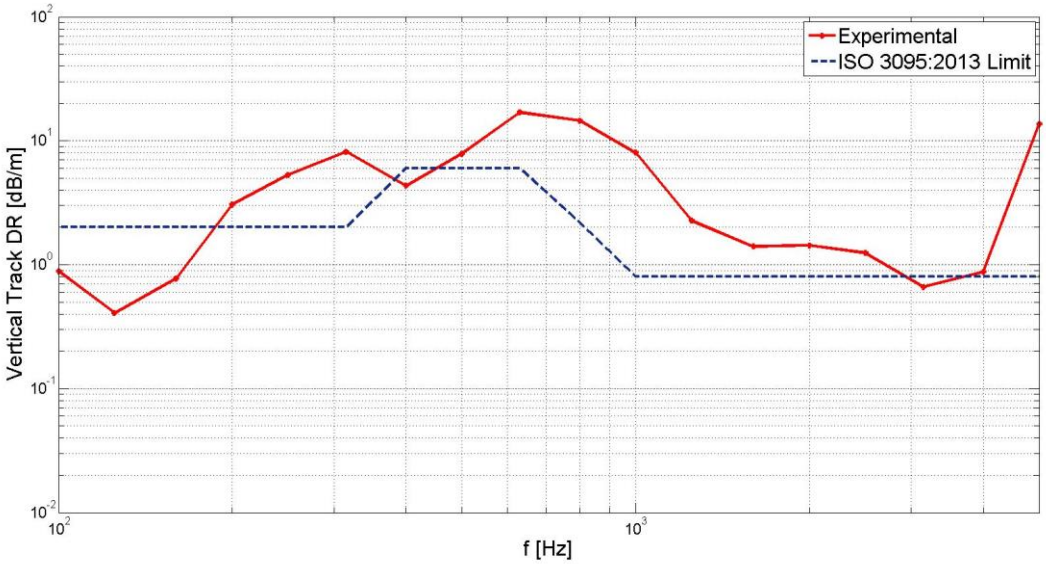

Figure 56: Vertical TDR.

Lateral decay rate is above the limit from the standard [11] over the full frequency range. For the vertical decay rate the values at 400 Hz and 3150 Hz are lower than the limit from the standard. Also, the measured decay rate values for the lower frequencies of the range (100 to 160 Hz) are lower than the limit curve (although in [11] this only extends down to 315 Hz).

Measurements in this low frequency range should be considered carefully because the hard tip used was unable to excite it properly. It was usually difficult to keep the coherence measured below 200 Hz above 0.85-0.9 when 4 hits were made.

The following figures show the different track mobilities measured.

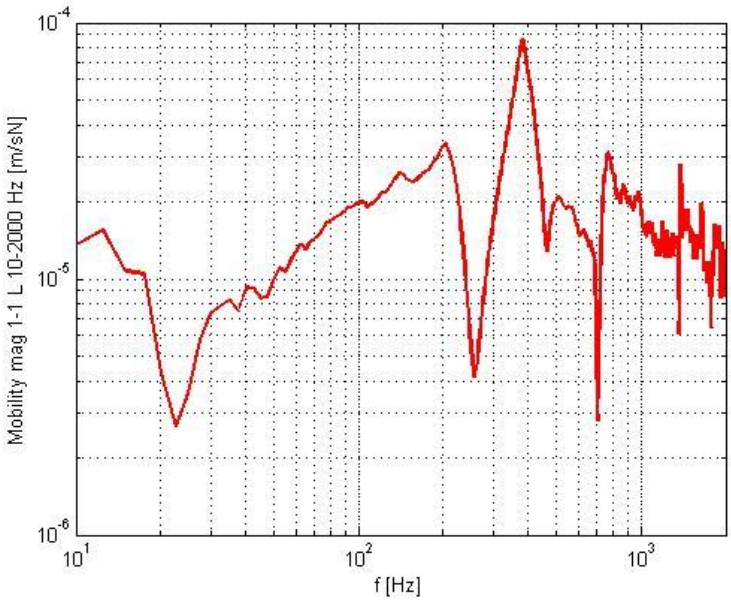

Figure 57: Lateral mobility magnitude over sleepers (1-1) from 10 Hz to 2 kHz

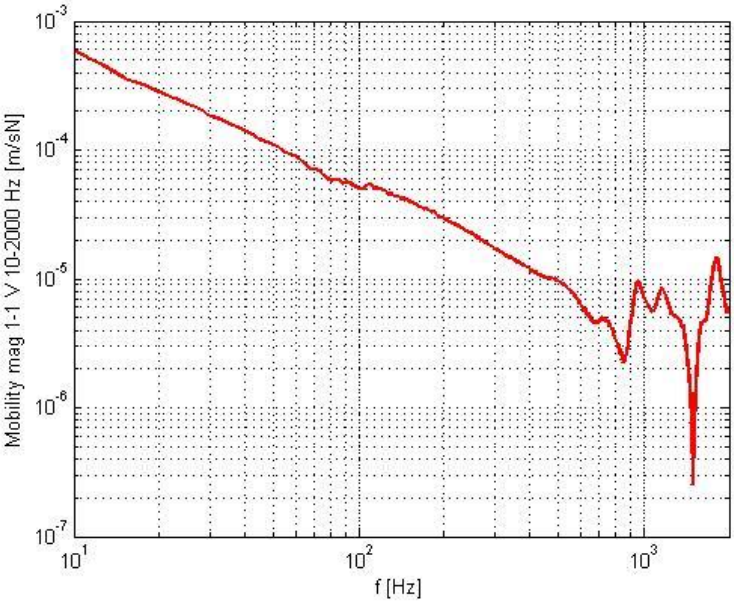

Figure 58: Vertical mobility magnitude over sleeper (1-1) from 10 Hz to 2 kHz

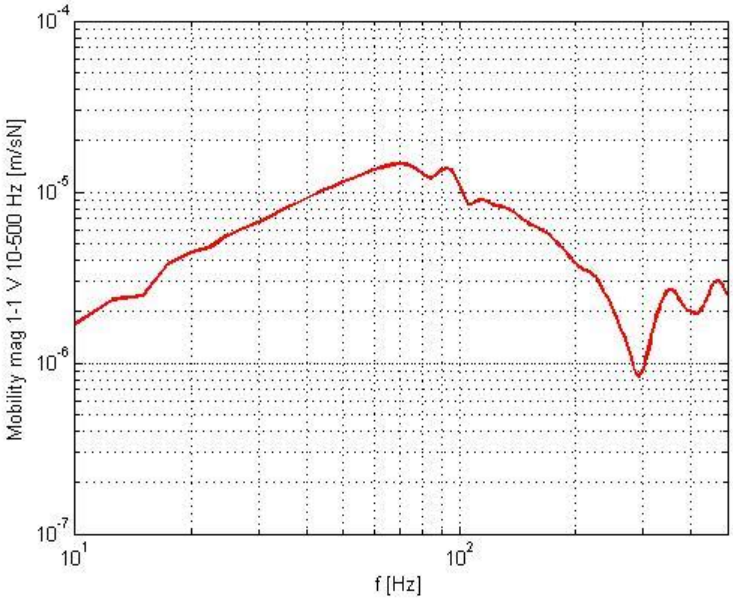

Figure 59: Vertical mobility magnitude over sleepers (1-1) from 10 Hz to 500 Hz

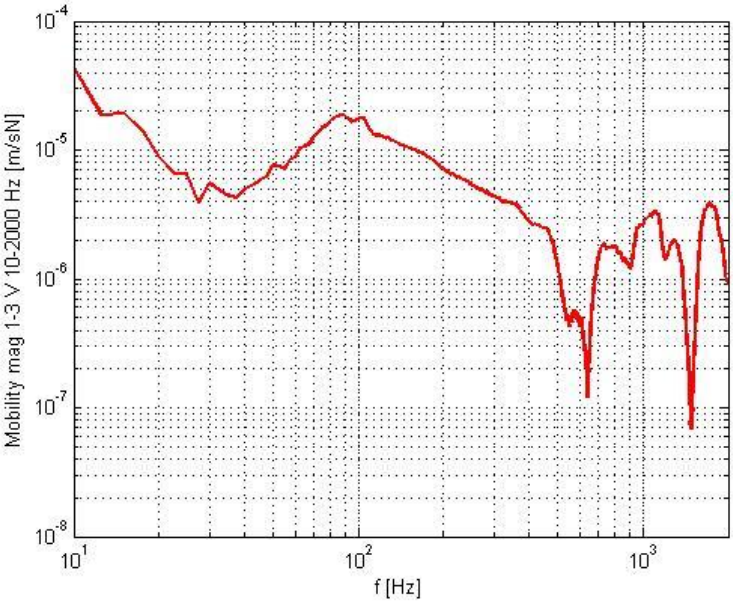

Figure 60: Vertical mobility magnitude, excitation on rail, measured on sleeper (1-3) from 10 Hz to 2 kHz

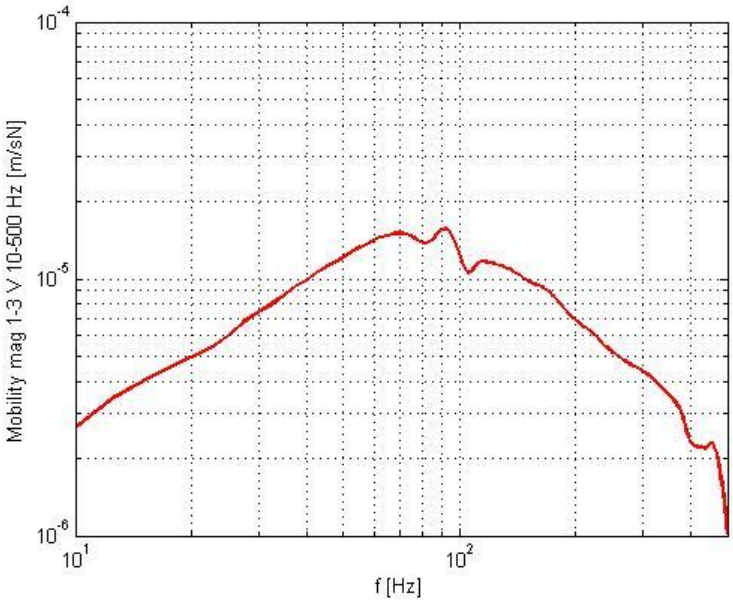

Figure 61: Vertical mobility magnitude, excitation on rail, measured on sleeper (1-3) from 10 Hz to 500 Hz

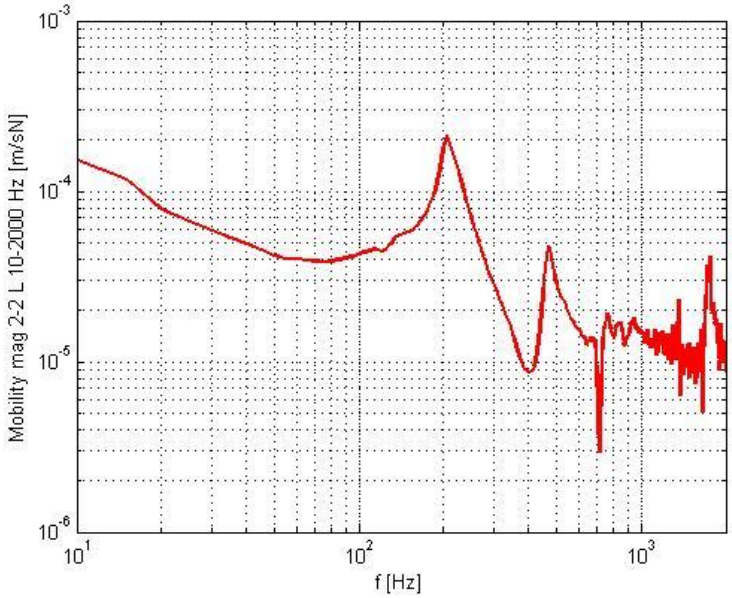

Figure 62: Lateral mobility magnitude middle sleeper bay (2-2) from 10 Hz to 2 kHz

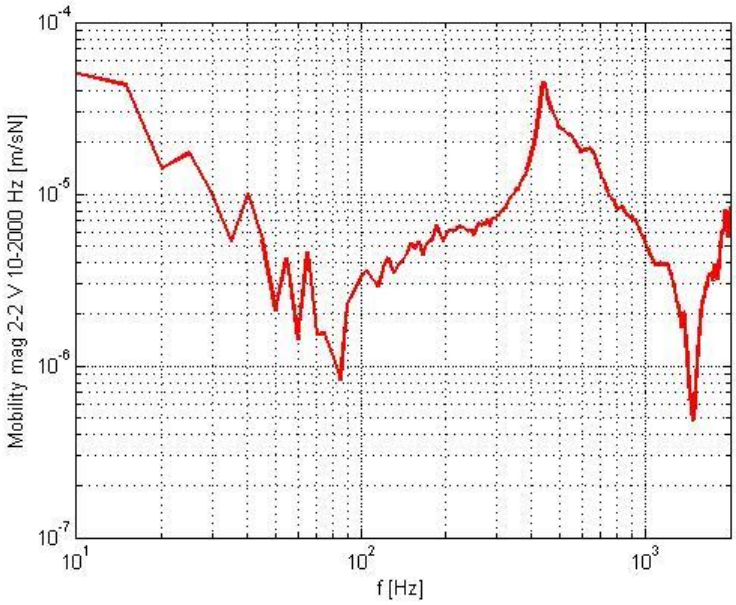

Figure 63: Vertical mobility magnitude middle sleeper bay (2-2) from 10 Hz to 2 kHz

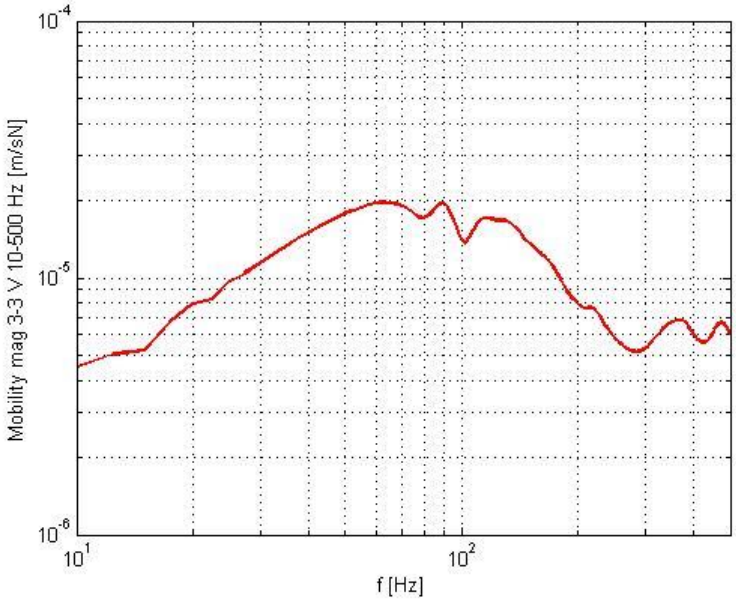

Figure 64: Vertical mobility magnitude on the sleeper (3-3) from 10 Hz to 500 Hz

A.3.1 Rail roughness

A.3.1.1 Measurement procedure

The rail roughness was measured with the Corrugation Analysis Trolley (CAT), according to the standard EN 15610:2009 [21]. In order to measure the acoustic roughness a sampling distance of 1 mm was fixed. The data obtained from CAT were post-processed to remove the spikes and apply the curvature processing.

As shown in Figure 65, the roughness was measured on both rails over a length of 80.25 m, which is equivalent to 80 sleeper bays. Five lines were measured within the running band at distances of 18, 33, 35, 37 and 43 mm from the inner face of each rail (Figure 65).

Additionally, the rail profiles corresponding to UIC54 rails with inclination 1/20 were sized using the MiniProf Rail.

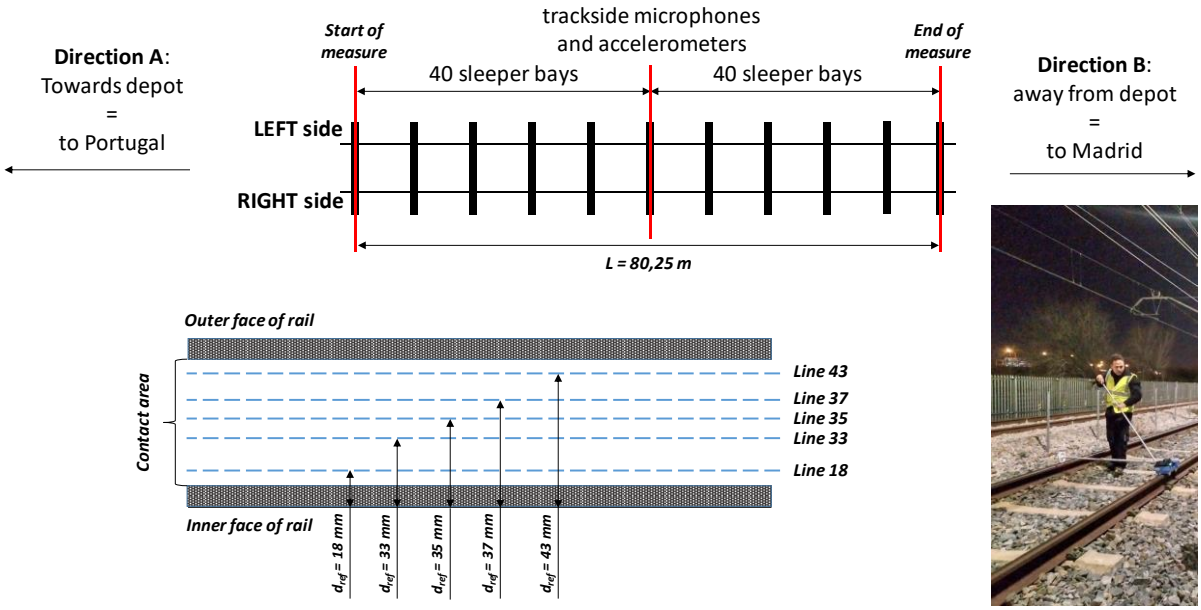

Figure 65: Distances and lines for rail roughness measurement.

A.3.1.2 Results

The profiles measured on both rails are shown in Figure 66.

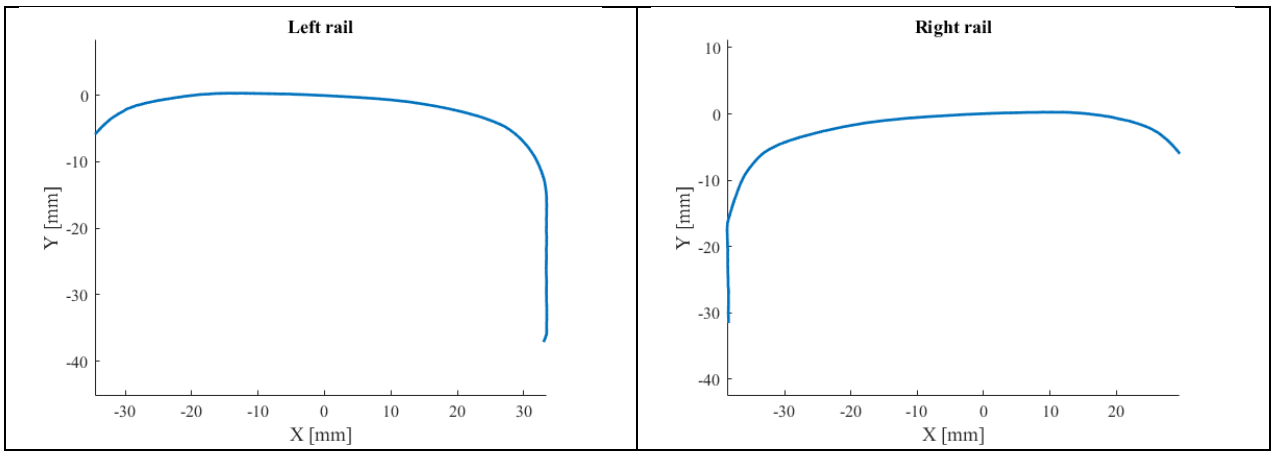

Figure 66: Measured rail profiles.

Roughness raw data for all measured lines and both rails are displayed from Figure 67 to Figure 71.

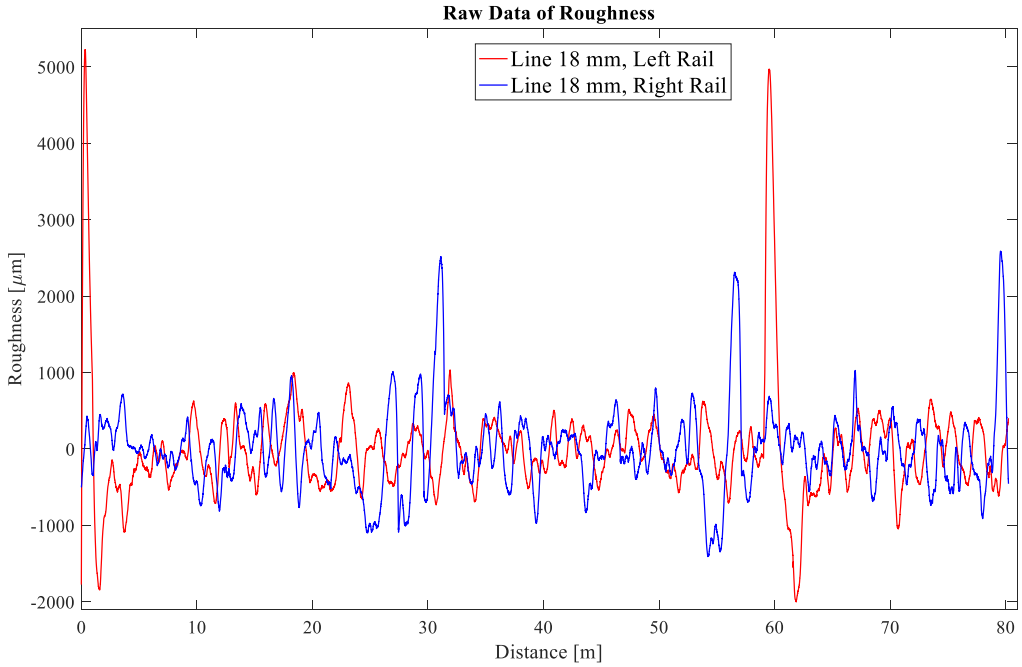

Figure 67: Raw data of roughness (μm) in both rails measured on line 18 mm.

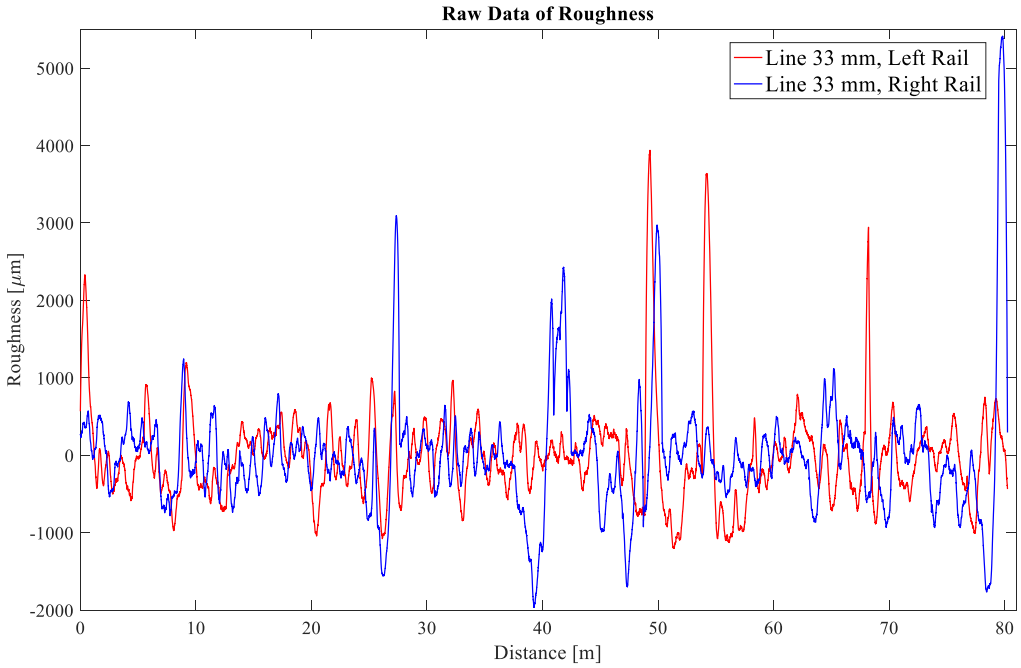

Figure 68: Raw data of roughness (μm) in both rails measured on line 33 mm.

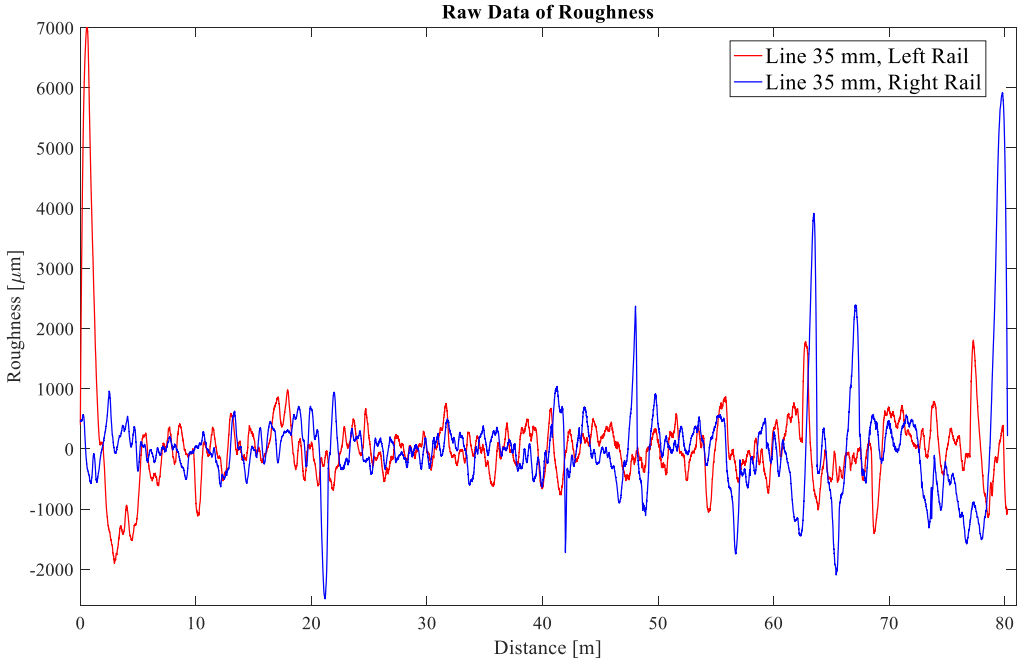

Figure 69: Raw data of roughness (μm) in both rails measured on line 35 mm.

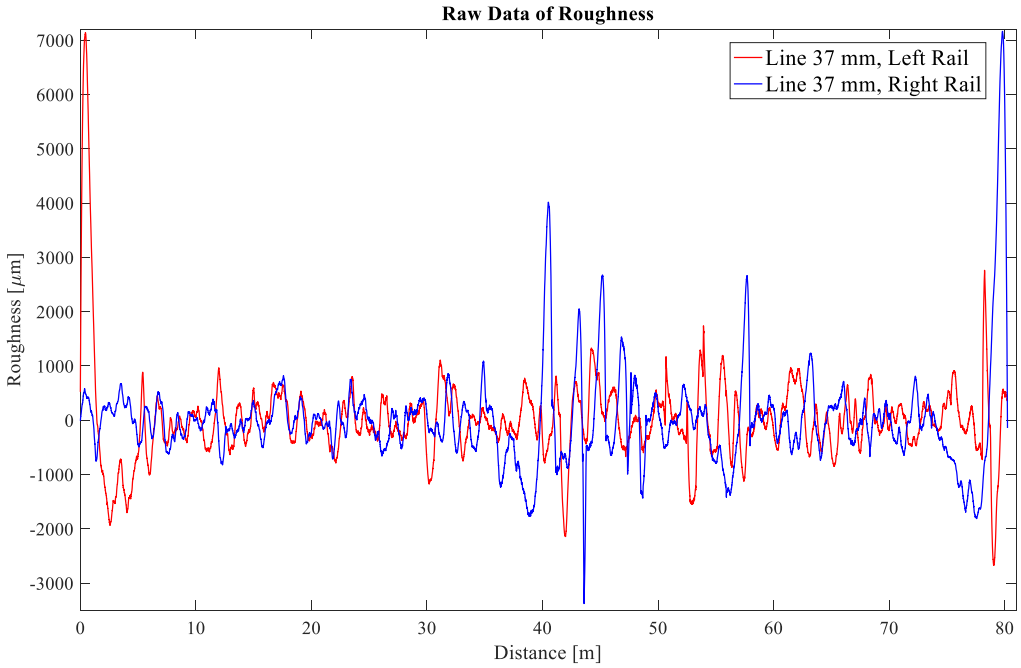

Figure 70: Raw data of roughness (μm) in both rails measured on line 37 mm.

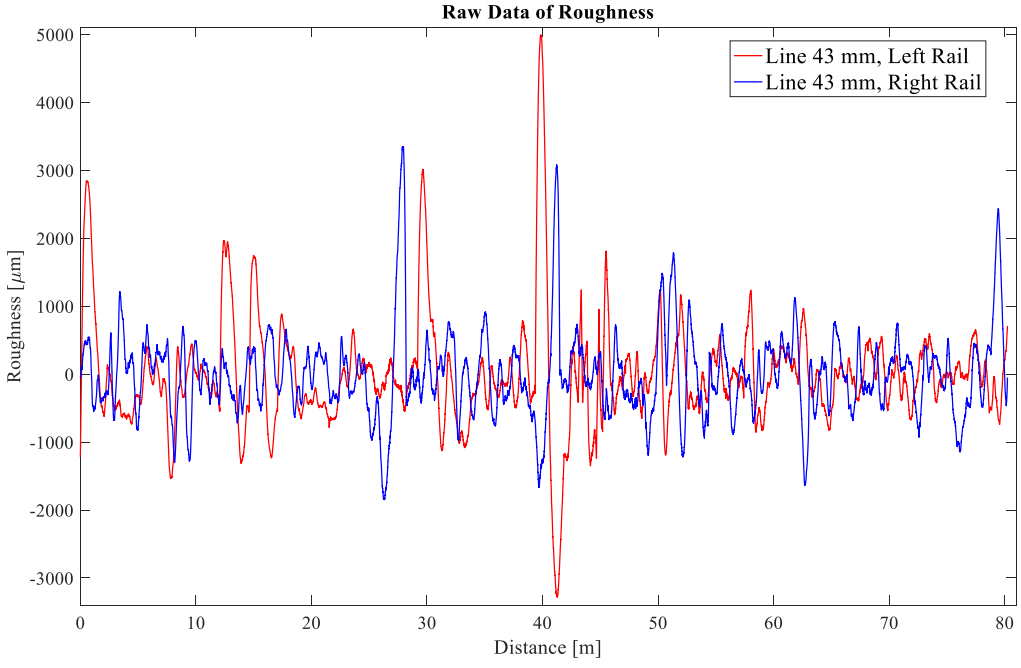

Figure 71: Raw data of roughness (μm) in both rails measured on line 43 mm.

One-third octave band spectra of the rail roughness are presented for the five lines and both rails in Figure 72 and Figure 73, and are compared with the rail roughness spectrum limit of the standard ISO 3095 [11] (TSI limit spectrum). The roughness level has a reference value of 1 µm.

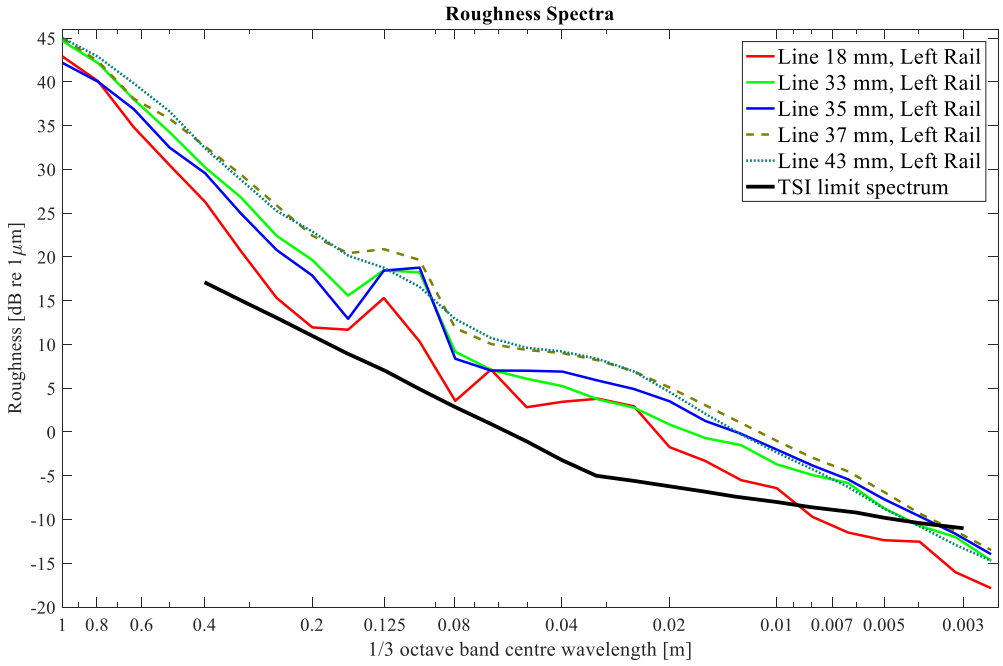

Figure 72: One-third octave band spectra of left rail roughness for all lines.

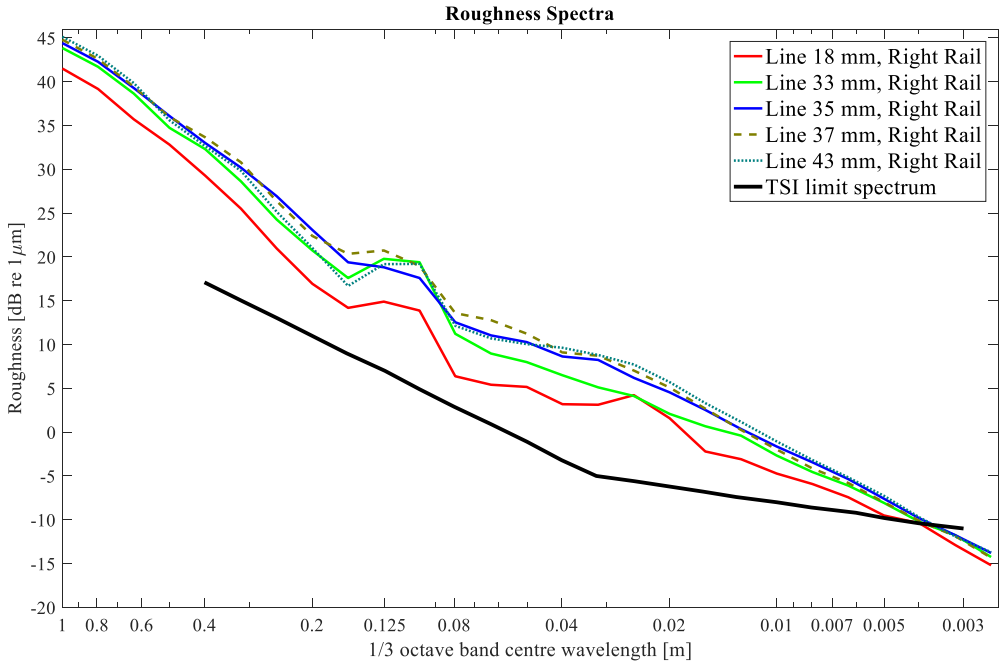

Figure 73: One-third octave band spectra of right rail roughness for all lines.

A.3.1.3 Comments

The results in Figure 67 to Figure 71 show some roughness peaks up to 7 mm in all measured lines of both rails, which is due to the low quality of the track rolling area. The location of the test track (inside a depot) does not lead to stringent track geometry quality requirements. In almost the entire wavelength range, the one-third octave band roughness spectra of both rails are above the TSI limit (by up to 15 dB), only being below the TSI limit when the wavelength is lower than 4 mm.

A.3.2 Wheel roughness

Wheel roughness measurements are performed on all 4 wheels of the trailer bogie (Figure 74). 3 LVDT displacements sensors, spaced 10 mm from each other (see Figure 75) are used. The displacement and an angular wheel speed are recorded simultaneously during 3 successive rotations of the wheel (~40 s per turn). The sample frequency is 5 kHz.

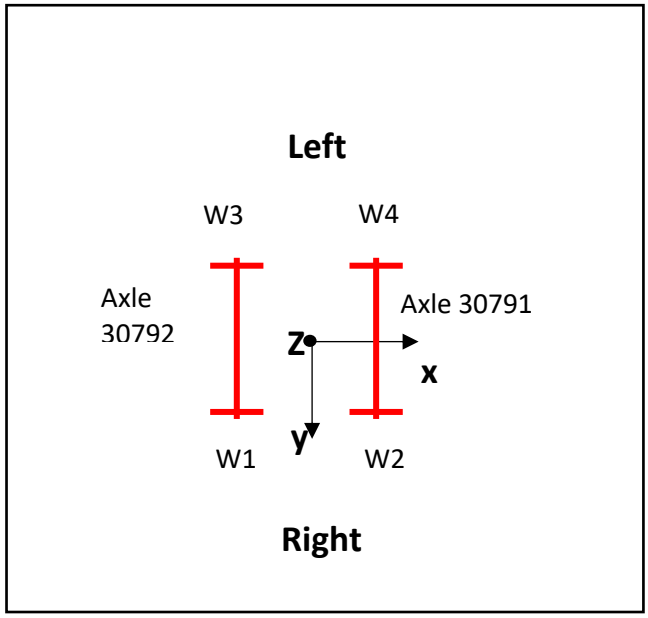

Figure 74: Wheel designation

Figure 75: Contact area of Wheel 4 with displacement sensors

Wheel description:

- Nominal geometry: Ø 860 mm – after reprofiling: 860.44 – 859.24 mm,
- Tyre width: 130 mm,
- Nominal contact point: 70 mm,
- The visible width of the contact area is around 30 mm (see Figure 75).
- The wheel tread is cleaned before the measurement.

Distances are given from **inner wheel side.** The measured spectra are given in Table 9.

Wavelength in mm	Trailer bogie wheels					
	W1	W2	W3	W4	Quadratic average	Rail (ISO3095-2013)
400	-8	1	-8	-2	-3	17.1
315	-12	1	-14	-1	-3	15
250	-15	-2	-17	-3	-6	13
200	-11	-3	-14	-4	-6	11
160	-17	-4	-12	-2	-5	9
125	-19	-10	-16	-4	-9	7
100	-20	-11	-15	-5	-10	4.9
80	-19	-11	-14	-6	-10	2.9
63	-20	-15	-17	-7	-12	0.9
50	-18	-16	-18	-9	-13	-1.1
40	-18	-16	-16	-12	-15	-3.2
31.5	-18	-17	-16	-14	-16	-5
25	-18	-16	-16	-14	-16	-5.6
20	-18	-9	-16	-15	-13	-6.2
15.7	-18	-13	-16	-15	-15	-6.8
12.5	-17	-18	-17	-15	-17	-7.4
9.9	-18	-18	-18	-17	-18	-8
7.9	-18	-19	-19	-18	-18	-8.6
6.3	-18	-19	-19	-19	-19	-9.2
5	-19	-19	-20	-19	-19	-9.8
4	-20	-20	-20	-20	-20	-10.4
3	-21	-21	-21	-21	-21	-11

Table 9: Measured wheel roughness in dB ref. 1µm

A.4 TRANSMISSION LOSS OF VEHICLE PANELS

A.4.1 Measurement procedure

The sound reduction index R_d of a panel characterizes its acoustic transmission loss. It is defined by the ratio between the transmitted intensity $I_{\text{transmitted}}$ and the incident intensity I_{incident}, in a diffuse sound field:

$$R_d = -10 \log_{10}\left(\frac{I_{\text{transmitted}}}{I_{\text{incident}}}\right) = L_{I,\text{incident}} - L_{I,\text{transmitted}}, L_I \text{ intensity levels in dB} \qquad \text{(A4.1)}$$

The incident (one-sided) intensity on the panels is deduced from the mean acoustic pressure level inside the coach using a diffuse field assumption. The average sound pressure level $L_{p,\text{diffuse}}$ is estimated using 3 microphones. Expressed in decibels (with the references: 10^{-12} W/m² for the intensity and 2.10^{-5} Pa for the pressure), the relation is:

$$L_{I,\text{incident}} = L_{p,\text{diffuse}} - 6\ dB \quad \text{(A4.2)}$$

Thus inserting formula (A4.2) into formula (A4.1) gives:

$$R_d = \left(L_{p,\text{diffuse}} - 6\ dB\right) - L_{I,\text{transmitted}} \quad \text{(A4.3)}$$

Two artificial sources (B&K Omnipower sources 4292-L connected to B&K power amplifier Type 2734 or equivalent) were placed inside the coach in order to create a diffuse field. The transmitted intensity is measured by scanning the outer skin of the coach with an intensity probe (type B&K 3599). Two different intensity probe spacer are used: d = 12 mm (limit: 5 kHz) and d = 50 mm (limit: 1.25 kHz). Measurements were carried out during night time, since the background noise in the workshop was low during this period. Measurements were repeated twice for each panel to insure repeatability.

Finally, the sound reduction index R_d per panel is directly available in ⅓ octave bands up to 5000 Hz. Note, that values above 50 dB are inaccurate. A global sound reduction index R_w is calculated based on ISO 717-1 standard for each panel.

A.4.2 Results

Figure 76 shows the location of the investigated panels. These are listed in Table 10. An example of the ⅓ octave band spectra is shown in Figure 77. For some panels the sound reduction index R_d had to be estimated for certain frequencies due to measurement difficulties (low transmitted intensity).

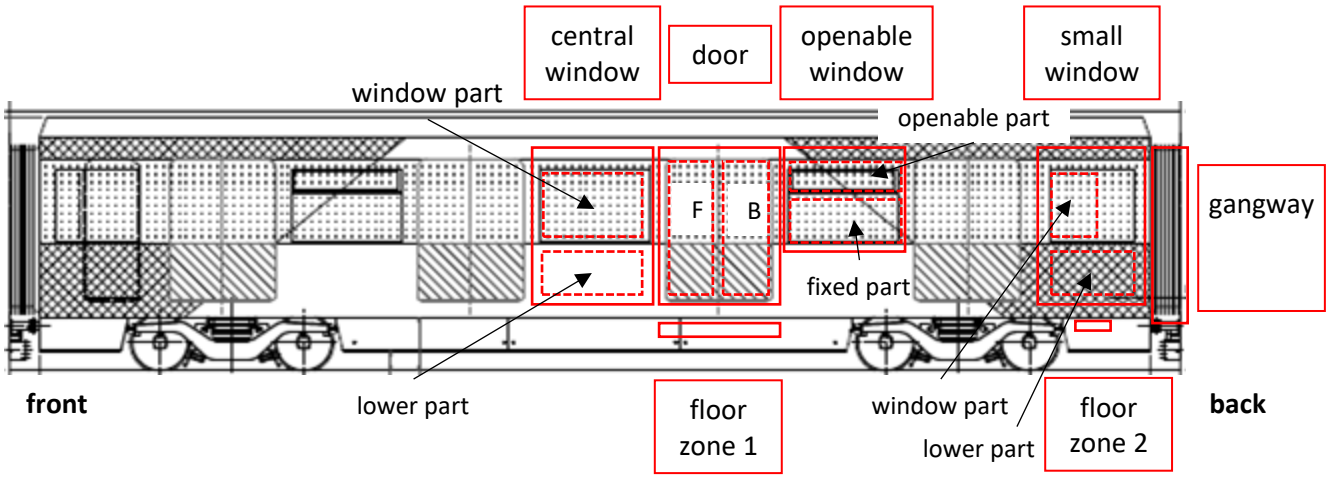

Figure 76: Definition of the panels (view from the left side, equipped bogie on the right)

Panels
Windows
Central window - window part (glass)
Central window - lower part (aluminium)
Openable window - fixed part
Openable window - openable part
Openable window - total
Small window - window part (glass)
Small window - lower part (aluminium)
Doors
F panel (left door part) - with joints
B panel (right door part) - no joints
B panel (right door part) - with joints
F + B - total
Gangway
Gangway - lateral
Gangway - floor
Floor
Floor - zone 1
Floor - zone 2

Table 10: Panels for measurement of global sound reduction index

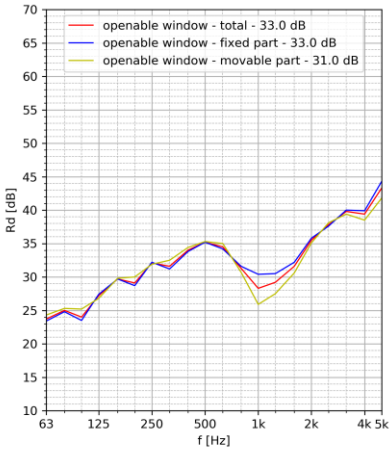

Figure 77: Example of sound reduction index for openable window panels

A.5 INTERNAL ABSORPTION

The internal absorption of the coach was assessed through reverberation time. This was measured according to standard ISO 3382-2:2008 [22]. 28 measurements were carried out, considering 7 combinations of microphone and source positions, with 4 measurements associated with each combination. In this particular case, the notation used for microphones was “Position 1” and “Position 2”, while for source location the corresponding nomenclature was “Source 1”, “Source 2” and “Source 3”. Finally, combinations P1S1, P1S2, P2S1, P2S2, P3S1, P3S2 and P3S3 were taken into account. Additional details can be found in Figure 78.

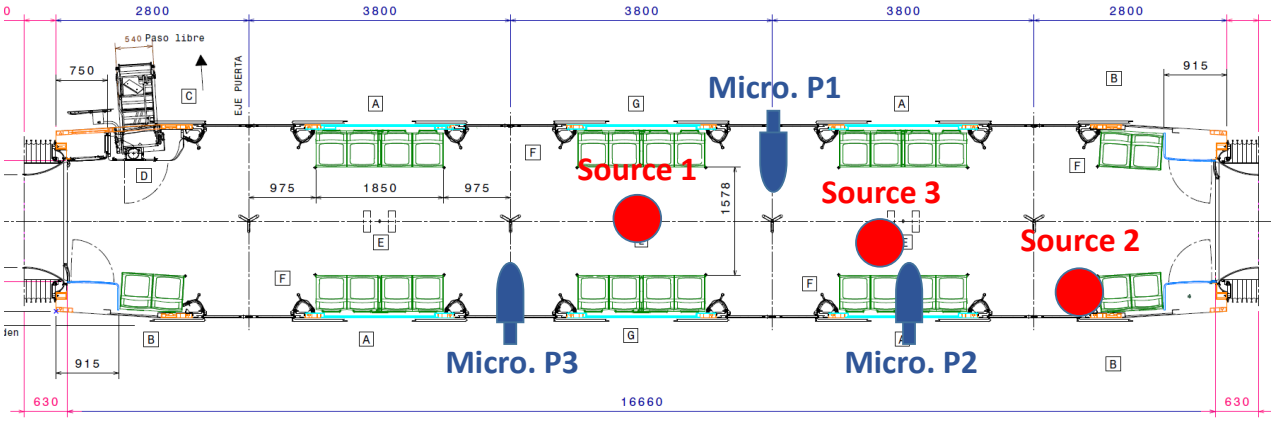

Figure 78: Coach scheme with source and microphone positions.

Several conditions had to be fulfilled during the measurements. In all cases, a minimum distance of 2 m between microphone positions was kept. Also, the minimum distance between microphones and reflective surfaces was 1 m (see Figure 79 for illustration purposes). To compute the minimum separation between microphones and sources, equation (1) of ISO 3382-2:2008 was considered,

$$d_{min} = 2\sqrt{\frac{Vol}{c\,T_{rev}}}\,. \qquad \text{(A5.1)}$$

To calculate the volume, the following dimensions of the coach are used: length = 18 m, width = 2.48 m and height = 2.1 m, which yields Vol = 93.74 m^3. For a temperature of 19ºC, the speed of sound is given by c = 342.6 m/s. Finally, a low value T_{rev} = 0.3 s is assumed to compute an overestimated d_{min} = 1.91 m.

Figure 79: Reverberation time measurement. Different source and microphone locations.

Figure 80 shows the average results in one-third octave bands. Note that, as mentioned previously, for a given curve associated with a microphone and source position, four measurements have been averaged. The final mean value is also depicted (which implies the average of 28 reverberation time measurements).

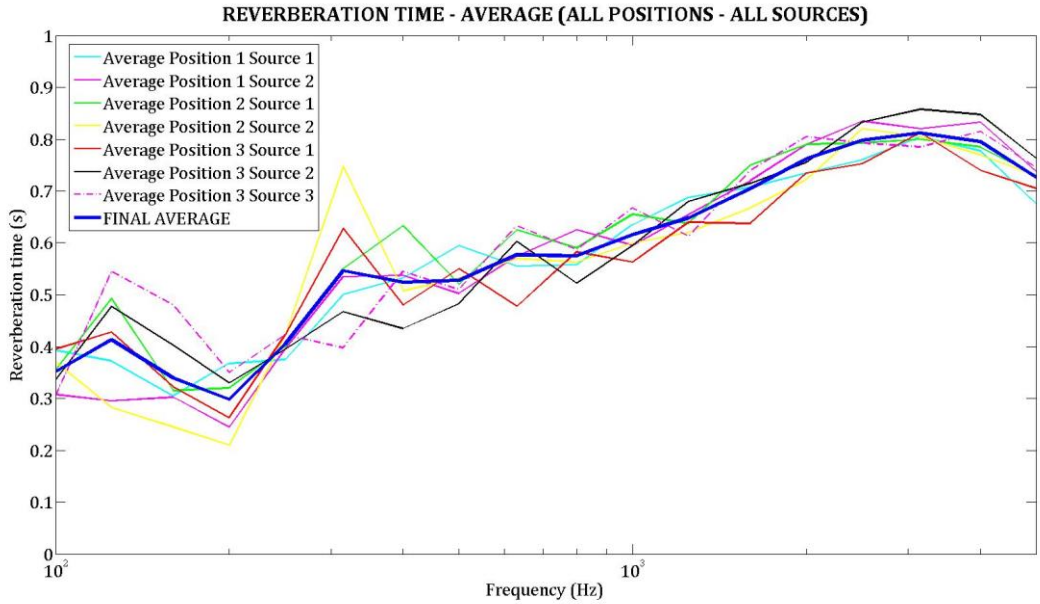

Figure 80: Reverberation time in one-third octave bands.

An estimation of the absorption coefficient α can be computed through Sabine's equation,

$$T_{rev} = 0.1611 \frac{Vol}{S\,\alpha}. \qquad \text{(A5.2)}$$

where the surface area S = 164.88 m^2 is computed neglecting front and rear coach ends. The corresponding values of the absorption coefficient are shown in Figure 81.

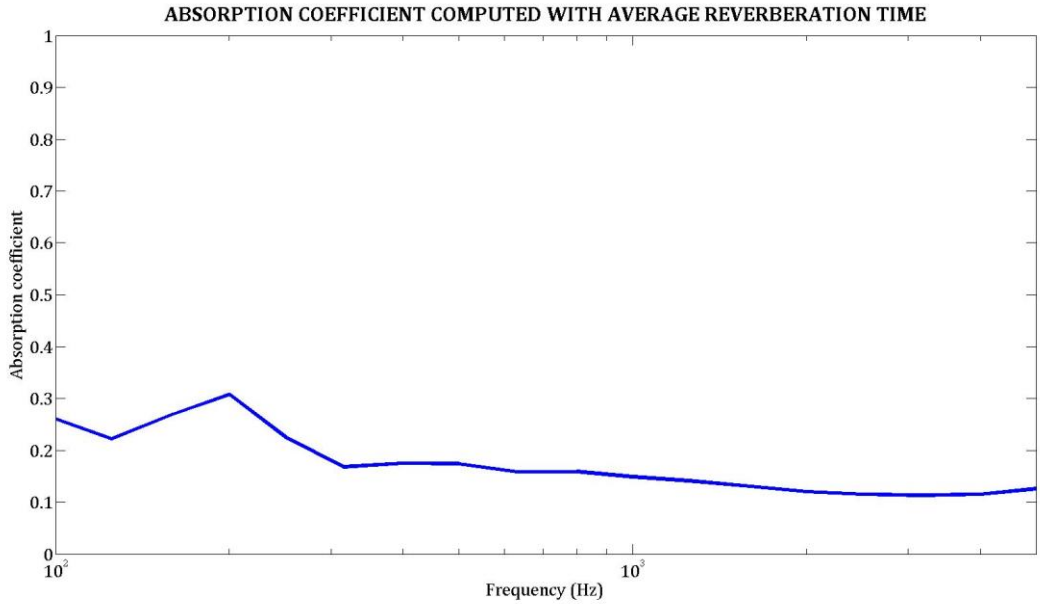

Figure 81: Coach absorption coefficient in one-third octave bands.

A.6 ACOUSTIC MEASUREMENTS BENEATH THE VEHICLE AND ON EXTERIOR WALLS

The results of the experimental measurements carried out beneath the vehicle and on exterior walls are shown in this section. For the first case, two microphone heights h = 0.17 m and h = 0.32 m were considered over the surface of the sleepers (see scheme in Figure 82). Microphone position 1 was at distance of 2 m from the source. The rest of microphone positions (2, 3, 4, …, 8) had a relative separation of 1 m. For each position, two measurements were carried out.

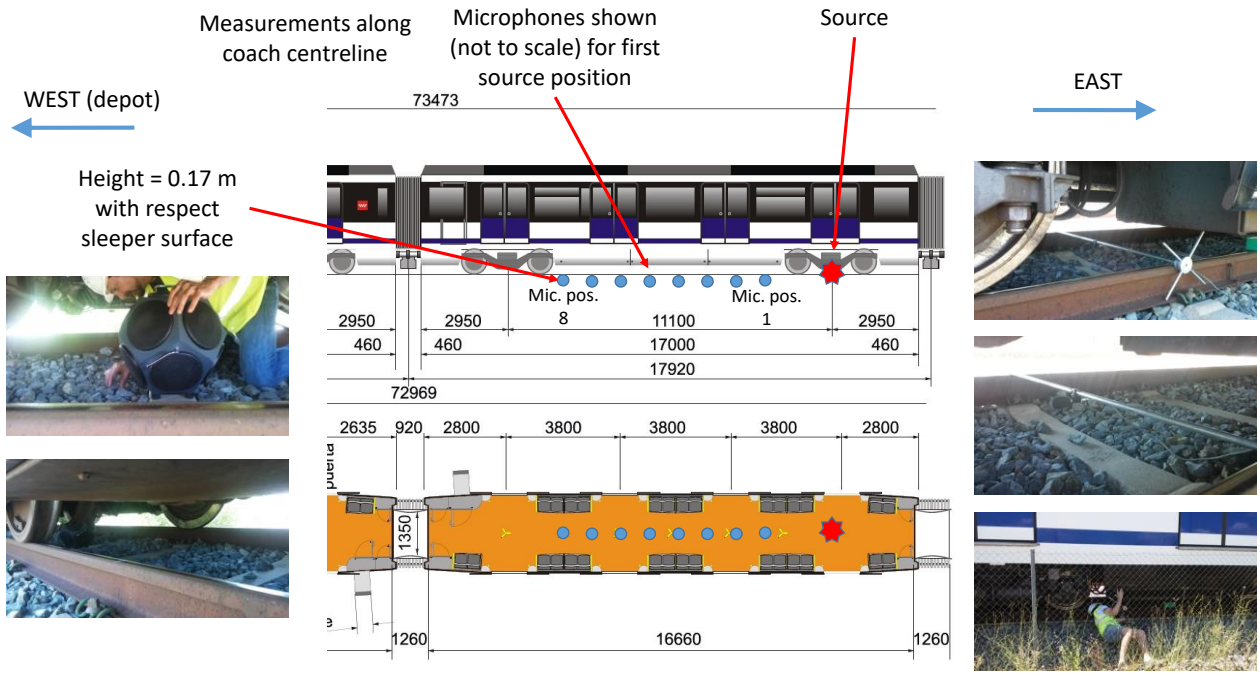

Figure 82: Acoustic measurements beneath the vehicle.

The results for *h* = 0.17 m and *h* = 0.32 m are given in Table 11 and Table 12. These are expressed in SPL (dB) in one third octave bands; dB(A) are provided in the last row.

Central frequency (Hz)	Position 1, measur. 1	Position 1, measur. 2	Position 2, measur. 1	Position 2, measur. 2	Position 3, measur. 1	Position 3, measur. 2	Position 4, measur. 1	Position 4, measur. 2	Position 5, measur. 1	Position 5, measur. 2	Position 6, measur. 1	Position 6, measur. 2	Position 7, measur. 1	Position 7, measur. 2	Position 8, measur. 1	Position 8, measur. 2
10	68.3	54.4	52	51.9	51.8	54.7	57	61	68.6	63.2	62.6	58.4	59.7	61.8	54	56
12.5	63.3	56.6	54.5	53.2	55.7	56.7	57.1	62.3	66.1	61.7	61.5	63.3	59.6	61	57	57.6
16	61.4	59.6	58.2	58.8	58.9	59.2	59	62.1	68.3	62.6	65.3	61.6	62.5	62.5	60.4	60.7
20	61.8	61.9	63	60.7	63.4	63.1	61.3	65.4	67.2	63.1	63.8	65.7	62.2	61.9	59.4	61.8
25	71.9	70.8	68.9	68.2	68	67.5	66.4	66.8	69.4	65.4	71.3	65.5	66.4	67.6	65.4	67.4
31.5	81.5	81.7	79.7	78.4	78.4	77.9	74.3	76.3	75.3	73.8	74.6	73.7	72.1	73.3	72.1	72.8
40	88.3	89.2	87.6	87.5	86.5	86.9	84	83.2	81.1	81.3	79.8	79.4	78.2	77.9	78.5	77.7
50	92.2	92.7	91.2	90.6	89.7	89.6	87	87	86.5	85.8	84.5	84.2	82.2	81.8	81.3	81.4
63	96.7	96.1	95.7	95.7	94.9	94.4	87.9	88.2	90.6	90	90.3	89.7	86.1	86.3	85	84.2
80	100.1	99.8	95.2	95.9	98.2	99.3	93.9	93.1	90.6	90.4	93.2	93	90.7	90.9	87.5	87.2
100	101.1	100.7	97.4	97.3	99	98.7	96.7	96.2	91.5	91	93.6	93.6	93.9	94.1	88.2	88.1
125	97.2	97	96.4	96	95.8	95.7	94.9	94.6	89.8	89.4	89.4	90.1	89.6	89.8	87.6	88.1
160	97.4	97.2	99.2	99.1	94.9	94.6	89.7	89.1	86.3	86.3	83.4	83.3	83	83.4	81	81.5
200	99.2	98.8	99.7	100	95.6	95.3	87.8	87.9	92.1	92.5	91.2	91.5	87.3	87.1	83.7	83.9
250	103.9	104.3	91.2	91.1	93.2	93.2	96.6	96.6	94.2	93.7	91.9	91.7	89.7	89.1	86.6	86.2
315	103.5	103.6	93.8	93.5	91.5	91.4	95.4	95.4	89.4	88.9	90	89.9	87.7	87.3	83.7	83.3
400	93.2	92.8	98.4	98.2	90.9	90.6	89.6	89.4	89.5	89.2	84.3	84.1	80.9	80.3	79.3	78.9
500	90.3	90.1	89.7	89.5	86.9	86.4	82.2	82.2	80.9	81	78.2	77.9	75.5	74.6	71.3	71.5
630	93.4	93.6	90.1	89.9	88.2	88.1	87.3	87.4	84.2	84.3	76.8	76.5	75.9	75.6	76.7	76.7
800	94.3	94	84.6	84.8	82.7	82.8	81.2	80.9	78.2	77.8	73.1	72.7	68.7	68.4	64.9	64.6
1000	93.1	92.9	88.4	88.1	87.1	87	76.7	76.7	73	72.8	70.5	70.5	68.8	68.8	65.3	65.2
1250	93.2	93.2	88.5	88.4	85.6	85.5	79	78.9	75.2	75.2	72.5	72.3	68.8	68.8	65.9	66
1600	94.1	94	89.7	89.4	84.5	84.2	82.8	82.5	78.7	78.4	73.2	73.3	67.9	68.2	67.3	67.4
2000	92	91.8	89	89.1	84.6	84.3	80.4	80.4	78	77.8	74	74.1	71	71	66.7	66.8
2500	93.4	93.5	87.9	87.9	83.6	83.5	79.3	79.2	78.2	77.8	75.6	75.5	73.9	74.4	69.2	69.5
3150	93	93.6	88.5	88.8	86.4	86.6	80.8	81	78.6	78.6	75.9	76	73.9	74.3	71	71.4
4000	90.1	90.2	84.6	84.9	82.7	83.2	79.4	79.9	76.8	77.1	73.3	73.5	69.6	70.5	70.2	70.5
5000	91.9	92.4	87.4	87.3	84.7	84.7	81.2	81.3	78.4	78.1	76.6	76.6	74.1	73.8	71.9	72.1
6300	85.7	85.5	81.9	81.6	80.8	80.2	76.4	75.9	72	72	69.2	68.6	67.7	66.8	65.2	65.4
8000	79	78.8	74.8	74.6	70.6	70.3	68.3	68.2	66	65.3	63.1	63.1	59.2	59.3	57.9	58.7
10000	66.6	65.9	63.9	63.4	59.8	59.1	57	56.5	53.4	52.7	49.8	49.4	49.1	48.2	46.6	46.2
12500	55	54.7	49.9	49.5	46.9	46.5	44.4	44.1	42.3	41	40.3	39.6	38.4	38.1	35.8	35.9
16000	48.3	47.8	43.9	43.9	41.8	41.8	38.3	38	35.4	35.4	33.1	32.9	30.1	30.3	28.7	29.1
20000	46.9	46.2	41.6	41.7	39.6	39.6	35.8	35.6	32.3	32.2	30.4	30.3	27.7	28.1	26	26.2
dB(A)	105.1	105.2	100.8	100.7	97.5	97.4	95.4	95.4	92.7	92.5	90.1	90.1	87.7	87.4	84.9	84.8

Table 11: SPL (dB) beneath the vehicle, *h* = 0.17 m

Central frequency (Hz)	Position 1, measur. 1	Position 1, measur. 2	Position 2, measur. 1	Position 2, measur. 2	Position 3, measur. 1	Position 3, measur. 2	Position 4, measur. 1	Position 4, measur. 2	Position 5, measur. 1	Position 5, measur. 2	Position 6, measur. 1	Position 6, measur. 2	Position 7, measur. 1	Position 7, measur. 2	Position 8, measur. 1	Position 8, measur. 2
10	55.3	68.1	52.3	55.1	55.4	56.1	65.3	72.4	59.2	67.4	61.2	63.9	56.9	60	54.6	56.3
12.5	58.8	72.1	55.4	56.4	54.5	56.6	65.2	72.4	58.6	63.1	63.1	62.8	61.8	60.6	57.7	57.1
16	66.3	63.8	59.6	58.9	58.9	59.5	65.3	71.3	61.2	63.1	63.6	63.3	63.8	64.8	62.6	59.7
20	65.9	66.1	62.8	62.3	62.2	61.5	64.4	68.8	65	64.8	64	62.5	66.4	61.2	63.3	62.1
25	70.7	71.9	68.9	69.3	68.9	67.2	67.8	69.3	67.1	66.6	65.3	64.9	66.5	67.6	63	64.3
31.5	82.8	82.4	80.9	80.1	78.2	79.3	75.4	75.2	74.6	74.8	73.4	73.2	73.1	72	71.1	71.3
40	89.7	89.3	88.3	86.9	87.6	86.8	83.3	83.2	81.5	81.7	79.3	79.1	78.7	77.9	77.7	77.5
50	93.1	92.7	90.8	90.7	91.2	90.1	87.5	86.5	86.6	86.6	84.7	84.5	82.1	81.3	82	81.6
63	96.5	96	95.3	94.9	95.4	94.5	88.8	88.1	91	90.5	90.7	90.3	86.3	86.5	84.3	84.6
80	100	100.1	95.3	95	99.2	99.3	93.5	93.7	90.9	90.8	92.8	92.6	90.3	89.9	87.2	86.7
100	101.3	101.1	97.9	97.9	98.4	99.3	96.6	96.1	91.9	91.7	93.7	94.1	93.5	93.3	87.5	87.5
125	98.2	98.2	96.5	96.6	96.2	96.1	95.4	94.7	88.7	89.1	90	90.5	89	90.1	85.8	86.2
160	98.1	98.2	100.2	99.8	97	96.6	89.6	89.9	86.4	86.1	84.8	84.3	84.3	84.4	81.6	81.4
200	99.3	98.6	97.6	97.7	95.5	95.5	88.7	88.4	92	91.9	92.1	92.1	88.8	89.1	85.1	85.1
250	100.6	100.3	95.5	95.6	96.2	95.9	95.5	96	94.2	94	90.7	90.9	89.3	89.4	86.1	86.4
315	101	101.1	95.6	95.7	94.7	94.4	95.4	95.3	89.4	89.1	87.1	87.5	88	87.6	82.5	82.4
400	92.8	92.8	95.5	95	91.4	90.9	86.4	86.1	83.8	83.3	82.4	82.8	78	77.9	75.8	75.3
500	88.7	88.6	87.3	87.3	87.5	87.4	80.8	80.8	77.3	77	75	75.1	75.4	75.5	67	66.5
630	94.5	94.7	91.8	91.9	90.8	91	91.1	90.8	81	80.6	78	78.9	79.7	79.6	77	77
800	94.7	94.5	89.3	89.1	83.7	83.9	83.9	83.7	75.6	75.3	75	74.8	72	71.7	68.6	68.5
1000	94.1	94.1	90.9	91	86.7	86.4	79.1	79.3	74.6	74.6	74.2	73.7	69.4	68.7	66.8	66.9
1250	92.1	91.9	89.3	89.5	86.5	85.8	79.6	80	75.4	75.4	74	74.2	71.2	71	66.6	66.6
1600	90.7	90.4	90	89.9	85.9	85.7	82.8	82.8	77.4	77.3	72.6	72.9	72	71.9	66.9	66.9
2000	93.2	92.9	89.2	89.3	86.2	85.5	81.6	82	77.2	77.2	73.5	73.7	69.7	69.8	67.7	67.6
2500	91.2	91.4	88.4	88.7	87.1	86.9	81.5	81.1	77	77	75.7	76.6	72.4	72.2	70.4	70.8
3150	93.9	94	89.5	89.8	86.8	86.5	83.7	83.6	77.3	77.2	74.3	75.4	72.2	72.1	71.5	71.6
4000	90	90.9	86.1	86.9	83.5	84.8	79	79.5	75.6	75.5	73.8	73.7	70.2	70.8	68.8	69.1
5000	91.3	91.3	87.6	88.1	83.9	85.6	82.1	82	76.6	76.9	76	75.9	72.9	72.8	70.7	70.9
6300	85.5	85.3	81.9	81.2	80.2	78.4	74.5	73.9	70.9	70.6	68.7	68.5	67.3	66.5	64.6	64.4
8000	78.7	78.6	76	76.6	73.4	73.2	68.5	68.2	64	63.9	61.6	61.4	59.5	58.8	58	57.9
10000	65.1	64.3	62.1	60.6	60.2	59.4	55.8	54.6	51.1	50.7	50.3	49.1	48.4	46.7	47.6	46.3
12500	54.2	54.1	50.6	50.5	47.9	47.7	44.3	44.1	39.9	39.7	38.2	38.9	36.3	35.9	34.5	34.1
16000	49.6	49.4	45.6	45.4	42.6	42.8	38.2	37.8	35.3	35	32.8	33.9	31	31.2	28.6	28.3
20000	47.7	47.5	43.1	42.9	40.6	40.4	42.4	35	32.2	31.8	29.9	30.5	28.3	28.4	25.4	25.2
dB(A)	104.3	104.3	101.2	101.3	98.7	98.6	96.1	96	91.4	91.2	89.4	89.7	87.8	87.8	84.4	84.5

Table 12: SPL (dB) beneath the vehicle, *h* = 0.32 m

Regarding the measurements on the exterior walls, two sections were considered, denoted as section 1 and section 2 (see schemes in Figure 83 and Figure 84, respectively). On the one hand, for section 1 the source was located in the central part of the bogie, close to the rail. The five microphone positions were located at a lateral distance of 0.3 m from the centre of the coach doors. The relative vertical separation between microphone positions was 0.5 m. On the other hand, for section 2 the source was located close to a wheel. The lateral distance between this section and section 1 was 1.5 m. The height of the five microphone positions was the same as in the previous case.

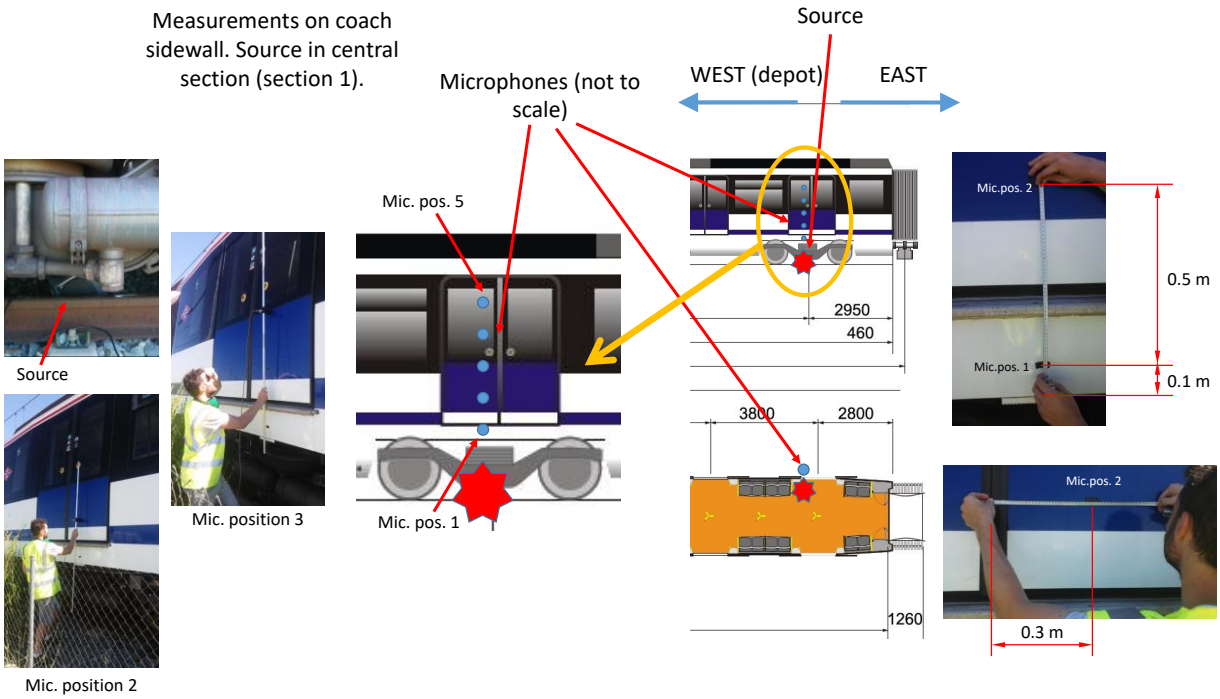

Figure 83: Acoustic measurements on exterior walls, section 1.

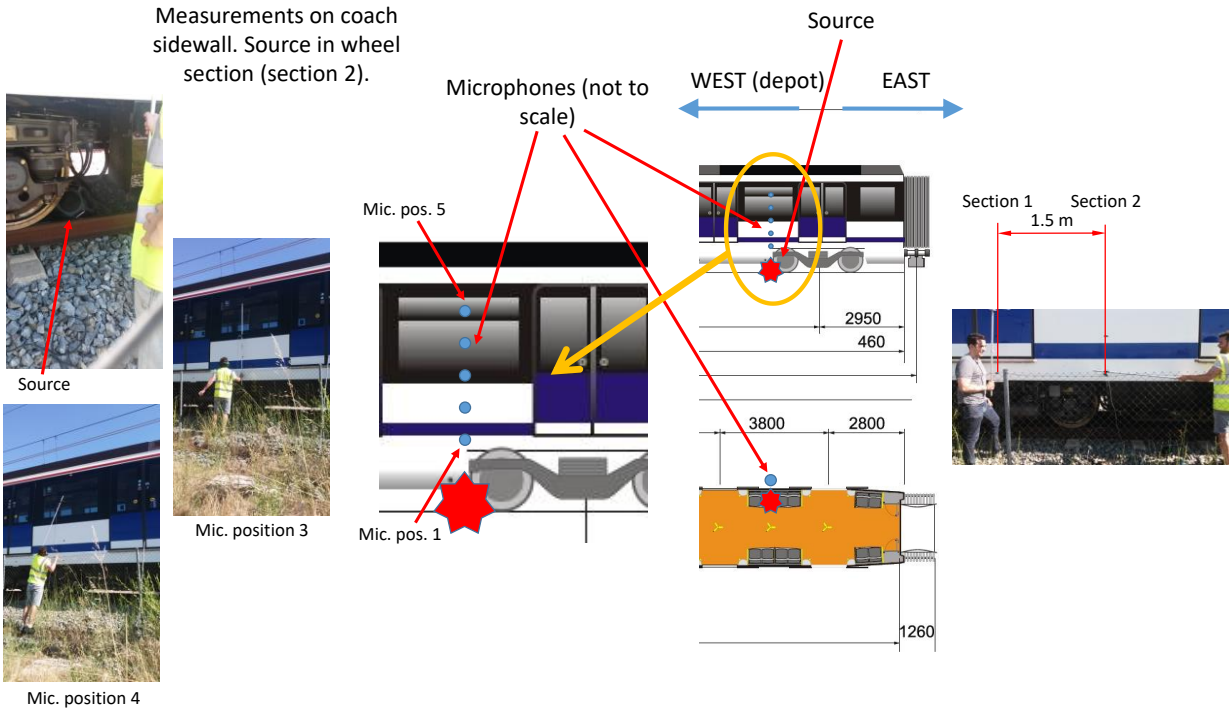

Figure 84: Acoustic measurements on exterior walls, section 2.

Similar to the previous results beneath the vehicle, two measurements were carried out for each exterior position. The results for section 1 and section 2 are given in Table 13 and Table 14. These are expressed in SPL (dB) in one third octave bands; dB(A) are provided in the last row.

Central frequency (Hz)	Position 1, measur. 1	Position 1, measur. 2	Position 2, measur. 1	Position 2, measur. 2	Position 3, measur. 1	Position 3, measur. 2	Position 4, measur. 1	Position 4, measur. 2	Position 5, measur. 1	Position 5, measur. 2
10	53.1	58.2	50.7	53.1	59.4	57.3	64.6	54.2	58	52.5
12.5	56.2	59	53.3	56.1	57.6	56.4	62.9	56.7	57.7	53.4
16	61.7	56.8	60.1	56.1	57.1	56.9	61.1	56.9	57.2	55.3
20	56.9	57.8	56	57	59.3	60.2	60.4	57.4	58.5	58
25	66.3	65.9	61.6	63.8	61.3	60.9	60.2	59.5	58.9	59
31.5	76.7	76.9	73.3	73.3	71	70.6	67.8	68.6	65.3	65.5
40	82.9	82.7	79.3	78.7	76.6	75.7	74.7	74.5	71.5	71.5
50	84.7	85.3	79.8	80.8	78	78.7	77.8	77.3	74.9	74.8
63	86.1	86.7	80.6	81	78.3	79	77.3	77	75.9	75.5
80	88	88.2	82	82.2	78.6	78.9	77.2	77.2	75.7	75.3
100	95	95.2	89.7	89.5	85.5	85.9	84.2	83.7	82.9	83.2
125	100.1	100	94.3	94.3	90.3	90	87	87.7	85.5	86
160	106.1	106.7	101.7	101.3	98	98.2	95.2	94.9	93.1	92.8
200	100.8	100.9	97	97.1	94.5	94.7	92.3	91.9	91.9	91.8
250	96.1	96.2	93.9	93.9	90.2	89.9	87.1	87	83.5	83.5
315	91.3	91.5	92.3	92.3	89.4	89.6	85.8	85.8	80.5	80.3
400	89.4	89	86.5	86.7	86.2	86.4	82.5	81.9	76.8	76.7
500	90.1	90	80.4	80.5	81	81.7	80.1	79.9	76.8	76.6
630	84	84.5	82.1	82.2	77.5	76.9	74.5	74.7	71.9	71.3
800	86.3	86.8	81.5	82.1	78.9	80	76.9	75.8	76.3	75.3
1000	87.3	87.7	77.5	77.5	74.5	75.5	72	71.6	68.4	67
1250	86.2	86.4	77.8	77.5	71.6	73.3	72.9	72	67.2	67.2
1600	83.9	84.2	77.9	78.5	79.4	76.5	71.7	71.2	69.4	69.3
2000	85.5	85.7	75.8	75.2	74.6	74.8	72.5	72.3	69.2	69.4
2500	81.8	82.2	74.4	74.9	73.3	70.8	70.5	70.9	69.8	69.3
3150	80.6	80.5	74.2	74.7	73.6	73.3	70.6	70.6	67.8	68
4000	80.3	80.4	73.4	73.1	71.5	72.5	68.7	70.2	66.3	67.1
5000	79	77.9	72.5	72.7	70.2	71.1	69.1	69.6	66.5	66.3
6300	73.7	73.4	66.2	65.8	63.9	64.4	62.6	62.2	60.2	60.3
8000	65.9	65.8	57	56.3	55.8	55.2	54.4	54.4	52.5	51.7
10000	53.4	52.9	43.3	43.3	42.7	42.9	41.1	40.9	38.6	37.7
12500	38.5	38.2	29.5	29.4	28.5	28.7	26.8	26.4	26.1	25.4
16000	31.3	32.3	24.1	24.2	22.8	23.2	21.4	21.2	21.8	21
20000	28.6	30.4	22.3	22.7	21.3	21.7	20.6	20.3	21.8	20.6
dB(A)	98.7	98.9	94.1	94.1	91.4	91.5	88.6	88.3	86.2	86

Table 13: SPL (dB) on exterior wall, section 1

Central frequency (Hz)	Position 1, measur. 1	Position 1, measur. 2	Position 2, measur. 1	Position 2, measur. 2	Position 3, measur. 1	Position 3, measur. 2	Position 4, measur. 1	Position 4, measur. 2	Position 5, measur. 1	Position 5, measur. 2
10	57.5	57	53	52.4	55.2	56.1	55.1	59.1	54.3	52.6
12.5	58	56.6	60	54.8	56.7	56.3	57.7	60.9	56.4	53.7
16	55.6	57.5	57.7	57.1	55.7	57.3	60.3	59.4	57.7	54.4
20	58.1	58.4	57.8	56.6	56.7	56.9	57.6	59.8	58.4	56.7
25	67.1	66.9	64.3	64	61.6	62.3	61.1	60.6	59.7	59
31.5	76.8	77.2	73.8	74	70.9	70.5	68.8	67.7	65.1	65.8
40	82.3	81.9	78.2	79.2	76.5	75.7	73.2	74.2	70.7	70.4
50	85.3	84.8	79.2	80	77.7	77.3	75.4	75.5	72.9	73.4
63	88.4	88.7	83.1	83.1	80	79.9	77.5	76.9	76.3	76
80	93.7	93.4	88.6	89.1	85.2	85.6	83.4	82.9	81.6	80.9
100	96.4	96	90.6	90.9	87	87.2	84.7	84.5	83.8	83.5
125	100.2	100.5	94.3	94.5	90.3	89.9	86.7	86.6	86.3	85.6
160	102	102.1	96.5	97.3	93	92.7	87.4	87.7	85.8	85.6
200	99.4	99.6	96.8	96.8	94.4	94.3	90.7	90.4	89.6	89.4
250	92.7	92.5	91.7	91.9	88.6	88.4	87.2	87	86.6	86.6
315	94.2	94	88.8	88.8	85.3	85.3	83.6	83.3	78.8	78.5
400	94.1	93.4	86.3	86.9	84.5	84.9	83.7	83.1	76.6	76.2
500	87	86.7	82.7	82.6	75.1	75.3	78.4	78.4	75	74.8
630	87.5	86.9	87	86.2	80.3	79.6	76.4	77.3	73.4	73.1
800	87.3	87.1	79.6	80.4	76.2	75.9	71	71.4	70.6	70.8
1000	90.9	91.1	83.4	82.9	76	76.3	68.8	70.2	69.6	70.3
1250	86.2	86.3	82.1	81.6	73.4	72.6	71.1	70.6	68.4	68.8
1600	81.5	81.5	80.4	79.8	72.7	71.9	68.8	70	68.1	68
2000	84.3	84.3	78.7	78.4	74.3	74.7	73.3	73.5	69.1	68.8
2500	83.9	85.2	79	78.6	76.4	76.2	72.8	73.3	68	68.3
3150	82.2	83.6	76.7	77.8	74.2	74.2	73.3	73.8	69.9	70
4000	80.9	82.4	74.9	75.3	74.2	74.3	71.8	72.4	68.2	68.9
5000	80.6	80.1	76.3	76.4	73.2	72.9	70.6	70.5	69.8	69.9
6300	72.7	71.4	70.5	70.2	65.5	65.6	63.6	63.8	61.5	61.2
8000	65.6	64	60.6	60.5	58	57.3	55.2	55.5	52.6	51.6
10000	54.1	53.5	49	49.4	42.9	42.2	41.9	42.2	39.4	38.7
12500	38.1	38.7	33.2	34.1	28.6	28.1	26.7	27	23.4	26.1
16000	30.6	29.7	26	26.5	22.5	22.3	21.2	22	19.6	25.8
20000	28	27.6	23.2	23.8	21.3	21	20.5	21.2	19.6	26.7
dB(A)	98.6	98.7	93.9	93.9	89.9	89.7	87.2	87.3	84.8	84.7

Table 14: SPL (dB) on exterior wall, section 2

A.7 STATIC MEASUREMENTS ON BOGIE FRAME

A.7.1 Measurement procedure

The bogie's modal behaviour was determined experimentally with the wheels on the rails, with operative secondary suspension and without load inside the coach. The track is specific (pit inside the workshop). Frequency response functions (FRF) were acquired by hammer impact (mean of 5 impacts). Its tip was adjusted according to the frequency range:

- 5-200 Hz : 086D20 HAMMER - soft tip,
- 12-400 Hz : 086D20 HAMMER - medium tip,
- 25-1000 Hz: 086D05 HAMMER – hard NYLON tip.

The driving points are located near the bogie side attachment point of the primary suspension connection (Figure 85).

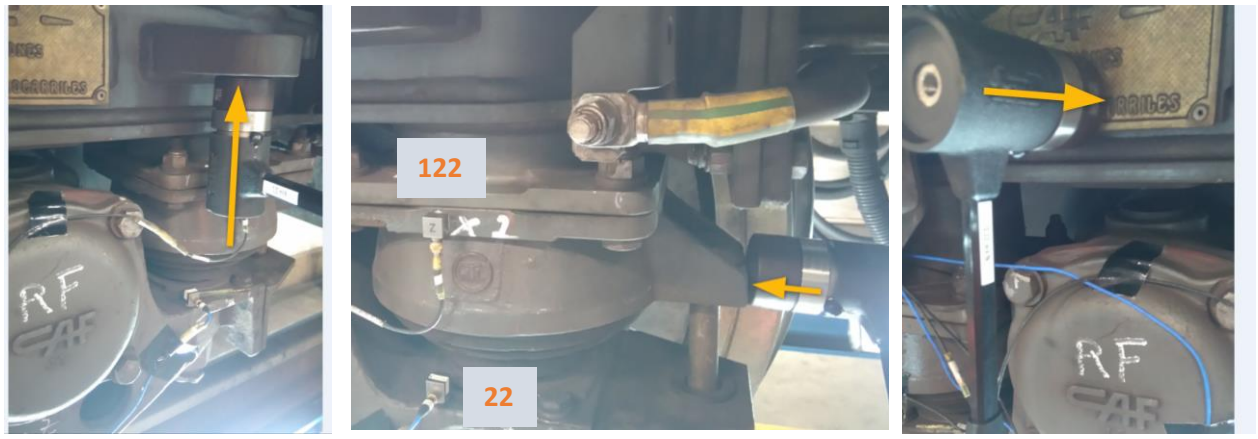

Direction Z Direction X Direction Y

Figure 85: Driving point location bogie (122) – response location 22 is on the wheel set side (upstream)

A.7.2 Results

FRF at the driving point (122) and the transfer to the upstream point (22) of the primary suspension are presented in Figure 86 to Figure 88. Particular modes are listed in Table 15.

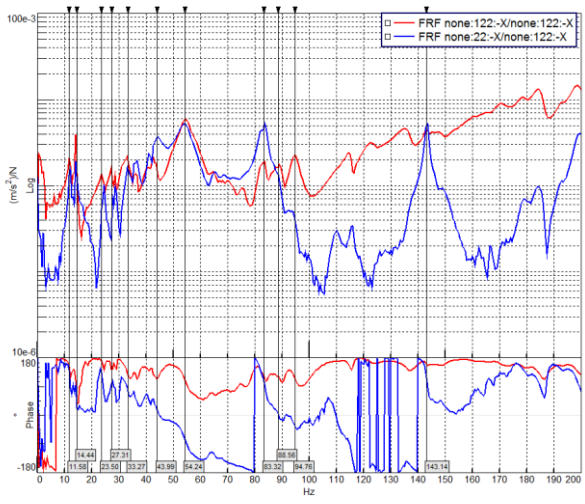

Figure 86: FRF Driving point 122 - Direction X

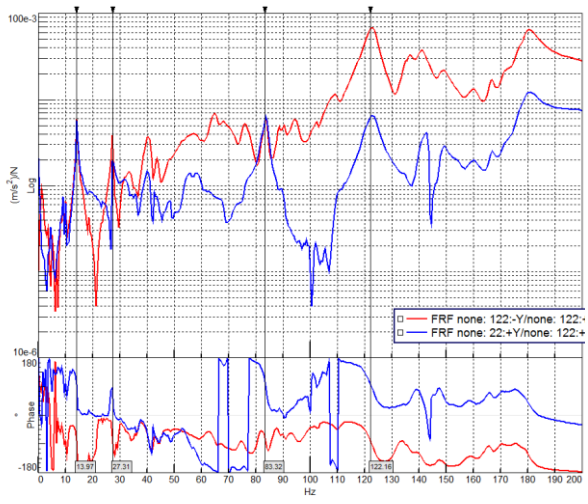

Figure 87: FRF Driving point 122 - Direction Y

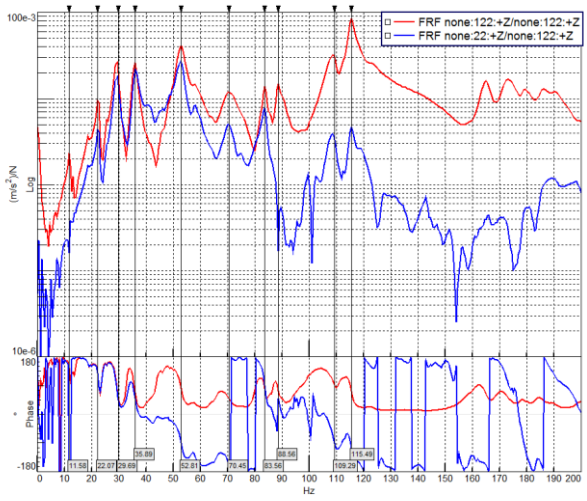

FRF 122 / 122 (Driving point)
FRF 22/ 122 (Transfer)
Units: ms²/N

Frequency range : 0 -200 Hz

Figure 88: FRF Driving point 122 - Direction Z

Frequency [Hz]	Modes shapes
11.7	Rigid body mode – bogie translation TX
14.2	Rigid body mode – bogie rotation θZ
22.4	Rigid body mode – bogie rotation θY
24.4	Rigid body mode – bogie translation TZ
27	Rigid body mode – bogie translation TY?
29.3	Rigid body mode – bogie rotation θY
36	Bogie torsion
52.8	Wheelset (21) & bogie (121) in opposition rigid body mode – Primary suspension in Z
54.3	Wheelset (21) & bogie (121) in opposition rigid body mode – Primary suspension in X

Table 15: Identified modes of the bogie

A.8 CAR BODY TRANSFER FUNCTIONS

A.8.1 Measurement procedure

Transfer functions γ/F have been recorded for many different excitation locations and a dense accelerometer mesh (mono- and tri-axial) is used to capture the transfer at each stage (see Figure 89 and Figure 90). The car body remains connected with the bogie. Hammer excitation is used and the frequency range covers 20 to 1 kHz.

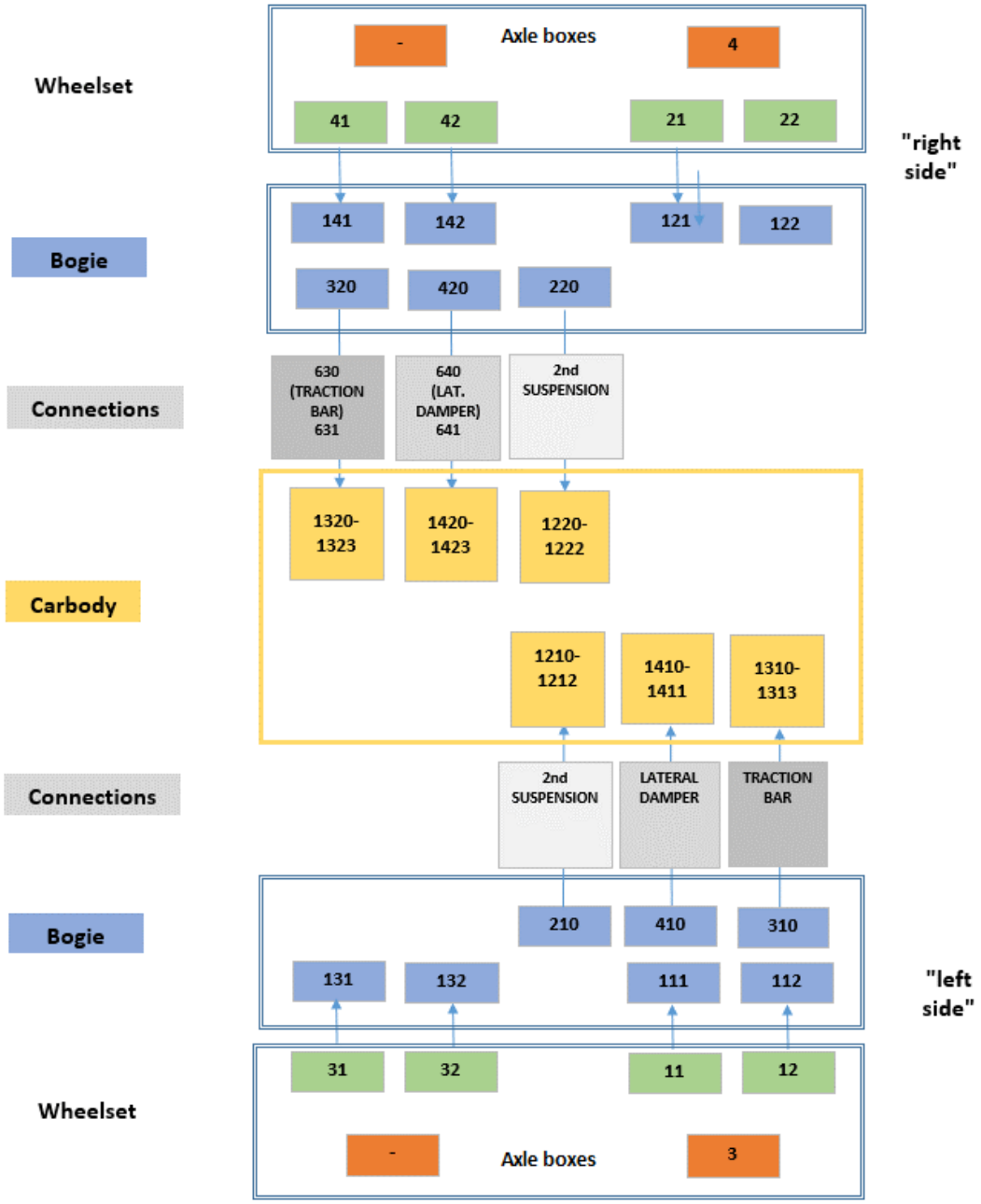

Figure 89: accelerometer instrumentation plan

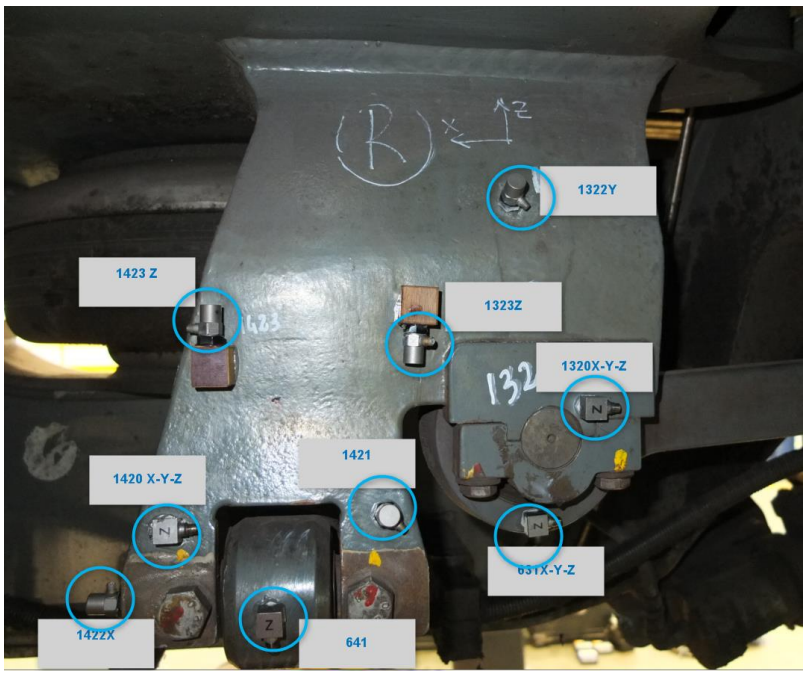

Figure 90: bolster connection (right vehicle side)

A.8.2 Results

Figure 91 and Figure 92 show examples of the available measurement data. The frequency response functions (FRF) shown correspond to an excitation on the bogie next to the upstream connection of the traction bar (Figure 93). Responses are given for the traction bar connecting points and the car body (Figure 90). Further data are not shown here, since it has not been decided yet which data will be used for the comparison with the numerical simulation.

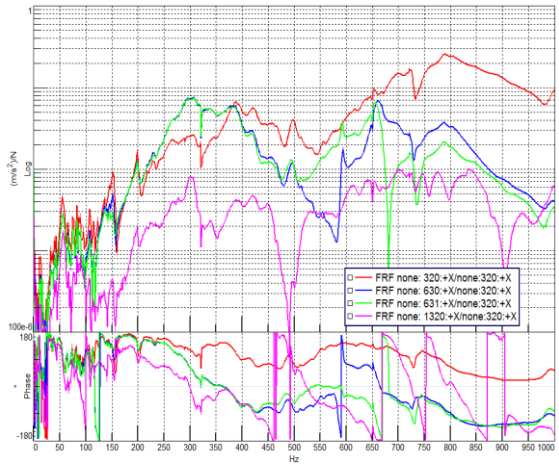

Figure 91: FRF Driving point 320 X

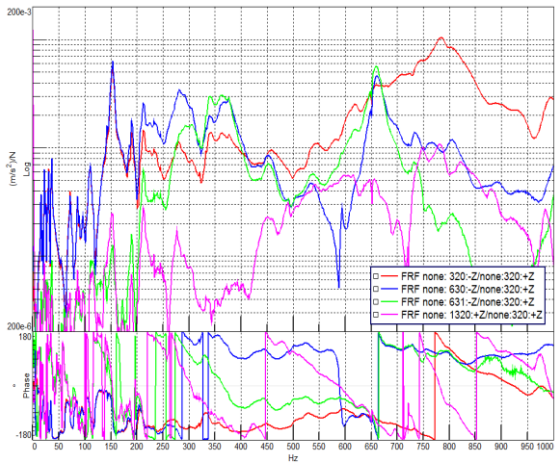

Figure 92: FRF Driving point 320 Z

Figure 93: Driving point on the bogie

FRF 320 / 320 (Bogie frame)
630/320 (Traction bar downstream)
631/320 (Traction bar upstream)
1320/320 (Car body)

(Unit: ms^{-2}/N - [0 – 1000 Hz])